ROLE OF THE P-CLUSTER AND FEMO-COFACTORS IN NITROGENASE CATALYSIS

by

Stephen Michael Keable

A dissertation submitted in partial fulfillment
of the requirements for the degree

of

Doctor of Philosophy

in

Biochemistry

MONTANA STATE UNIVERSITY
Bozeman, Montana

January 2017

©COPYRIGHT

by

Stephen Michael Keable

2017

All Rights Reserved

TABLE OF CONTENTS

1. INTRODUCTION 1

Nitrogenase 1
Nitrogenase P-clusters and FeMo-cofactors 4
Research Directions 8

2. FE PROTEIN-INDEPENDENT SUBSTRATE REDUCTION BY NITROGENASE MOFE PROTEIN VARIANTS 10

Contribution of Authors and Co-Authors 10
Manuscript Information Page 12
Abstract 13
Chapter Introduction 14
Materials and Methods 17
Results and Discussion 21
Activity Assays 21
Structural Analysis 26
Computational Analysis 28
Conclusion 31

3. THREE STRUCTURAL STATES OF THE NITROGENASE P-CLUSTER REVEALED IN MOFE PROTEIN STRUCTURES AT POISED POTENTIALS 33

Contribution of Authors and Co-Authors 33
Manuscript Information Page 34
Abstract 35
Chapter Introduction 35
Materials and Methods 39
Poising Crystals with Redox Mediators 39
Results and Discussion 42
Conclusion 46

4. ACETYLENE INTERACTIOIN WITH THE NITROGENASE FEMO-COFACTOR INVESTIGATED BY STRUCTURAL AND COMPUTATIONAL ANALYSIS 48

Contribution of Authors and Co-Authors 48
Manuscript Information Page 50
Abstract 51
Chapter Introduction 51
Materials and Methods 54

TABLE OF CONTENTS – CONTINUED

Computational Analysis of Acetylene Bound MoFe 57
Structural Analysis of Acetylene Bound MoFe 64
Conclusion 66

5. LIGHT-DRIVEN DINITROGEN REDUCTION CATALYZED BY A CDS:NITROGENASE MOFE PROTEIN BIOHYBRID 67

Contribution of Authors and Co-Authors 67
Manuscript Information Page 69
Abstract 70
Chapter Introduction 70
Materials and Methods 73
Results and Discussion 80
Photoexcitation of the CdS:MoFe protein biohybrids 80
Conclusion 84

2. CONCLUDING REMARKS 85

REFERENCES CITED 89

APPENDICES 98

APPENDIX A: Supplemental information from chapter 2 98
APPENDIX B: Supplemental information from chapter 3 104
APPENDIX C: Supplemental information from chapter 4 107
APPENDIX D: Supplemental information from chapter 5 113

LIST OF TABLES

Table Page

2.1 Product formation of MoFe protein variants using Eu(II)-L as reductant 25

4.1 Energetics of binding of acetylene to FeMo-co at various levels of modeling 57

S2.4 Data collection and refinement statistics for ß-98$^{Tyr\rightarrow His}$ structure 103

S3.1 Data collection and refinement statistics for P^{1+} structure 105

S3.2 Data collection statistics for P^{N} structure 106

S3.3 Data collection statistics for P^{2+} structure 106

S4.1 Data collection and refinement statistics for α-96$^{Arg\rightarrow Gln}$ structure 108

S4.2 Main interatomic distances for X-ray structure and two DFT optimized models 109

S4.3 Comparative summary of binding energy of acetylene to active site 110

S4.4 Summary of the energetics of binding at various levels of modeling 111

S4.5 Comparison of most relevant interatomic distances between α-96$^{Arg\rightarrow Gln}$ and two DFT models 112

S5.4 Turnover frequencies (TOF) of H_2 production for 30 min illumination of MoFe/nanocrystal complexes 118

S5.5 Turnover frequencies for H_2 production by CdS:MoFe protein biohybrids with various hole scavengers 119

S5.6 Table of control reactions that did not produce NH_3 120

LIST OF TABLES – CONTINUED

S5.7 Average raw fluorescence measurements for photochemical NH_3 121

S5.8 Results of NH_3 and H_2 production by CdS:MoFe protein biohybrids lacking reaction components..... 122

S5.9 Comparison of NH_3 and H_2 production rates between wild type and biohybrid nitrogenase 123

S5.10 Parameters used to estimate the quantum yield of product formation..... 124

S5.11 Electron requirement for NH_3 and H_2 product formation..... 125

S5.12 Uncorrected NH_3 production time course data 126

S5.13 Background corrected N_2 reduction/NH_3 production time course data 127

S5.14 Inhibition of Fe protein/ATP dependent H_2 production..... 128

S5.15 Data used to determine the effects of gaseous inhibitors on TOF of NH_3 production 129

S5.16 TOF of NH_3 production by CdS:MoFe protein 130

LIST OF FIGURES

1.1 Structural representation of nitrogenase MoFe-Fe protein complex 2

1.2 Ball and stick representations of the P-cluster and FeMo-cofactor 4

1.3 Proposed substrate channel accessing the active site of the MoFe protein 6

2.1 Nitrogenase and metal clusters 15

2.2 Fe protein independent hydrazine reduction catalyzed by MoFe protein variants 22

2.3 Concentration dependence of hydrazine on MoFe protein substrate reduction 24

2.4 Model of ß-98$^{Tyr\rightarrow His}$ superimposed with experimental electron density and wild type model 27

2.5 Mechanical coupling between core residues and the rest of the MoFe protein/Fe protein complex 29

2.6 Collective motion corresponding to the rocking of Fe protein on the MoFe protein surface 30

3.1 Structural representations of the P2+ and PN redox states of the P-cluster 37

3.2 Schematic drawing of crystal poising apparatus 38

3.3 Models of $P^{2+,}$ P^{N} and P^{1+} structural states of the P-cluster superimposed with electron density 41

3.4 Structural representation of the P1+ redox state of the P-cluster 42

LIST OF FIGURES – CONTINUED

3.5 Difference electron density analysis of electrochemically poised P-cluster structures 43

3.6 Ball and stick representations of the P-cluster and FeMo-co highlighting orientating to each other 45

4.1 Superposition of α-96$^{Arg\rightarrow Gln}$ and DFT optimized structures 53

4.2 Acetylene distance shift between α-96$^{Arg\rightarrow Gln}$ and DFT optimized structure 58

4.3 Neutrally charged model with four K+ ions 60

4.4 Superposition of α-96$^{Arg\rightarrow Gln}$ structure and DFT optimized structures with dispersion correction 61

4.5 Electrostatic features of protein region surrounding acetylene in α-96$^{Arg\rightarrow Gln}$ and wild type structures 63

4.6 The α-96$^{Arg\rightarrow Gln}$ structure with acetylene modeled into experimental electron density 65

5.1 Reaction scheme for N_2 reduction to NH_3 by nitrogenase and the CdS:MoFe protein biohybrids 72

5.2 Photochemical N_2 reduction to NH_3 by CdS:MoFe protein biohybrids 81

S2.1 Beta factors for the nitrogenase complex 98

S2.2 Concentration dependence of Eu(II)-DPTA on MoFe protein substrate reduction 100

S2.3 Covariance matrix for MoFe protein/Fe protein complex 102

S5.1 TEM images of CdS nanocrystals and UV-vis spectrum of the CdS nanocrystals 114

LIST OF FIGURES – CONTINUED

S5.2 Calibration curve for colorimetric NH_3 assay 115

S5.2 Photochemical H_2 production by CdS:MoFe protein biohybrids 117

ABSTRACT

Biological nitrogen fixation has been extensively researched for over four decades, yet due to the complex nature of this process, numerous questions still remain regarding the catalytic mechanism, and investigation of this system has relevance across a number of disciplines. Nitrogen is a fundamental element to all biological systems, primarily occurring in proteins and nucleic acids. However, most nitrogen on Earth is found in the form of nitrogen gas, a form that is biologically unavailable to most organisms owing to the strength of the triple bond between the two nitrogen atoms. The limited abundance of biologically accessible (or fixed) nitrogen has driven an anthropomorphic thrust to supplement the nitrogen cycle with nitrogenous fertilizers, thereby boosting agricultural output. The primary industrial method to produce these fertilizers, derived from the Haber-Bosch synthesis, is an energy intensive process that consumes approximately 1-2% of the world's energy portfolio. This process utilizes metal iron catalysis, high temperatures and high pressures, along with hydrogen usually obtained from reformed fossil fuels, to reduce atmospheric nitrogen gas to ammonia. Aside from the environmental consequences that arise from the production of nitrogenous fertilizers, long-term agricultural application may also have disastrous ecological ramifications, such as eutrophication. Additionally, biological nitrogen fixation supports more than half the human population, and having a more complete understanding of this complex process has the potential to displace some of the demand for fertilizer production. The aforementioned reasons are clearly enough to warrant serious investigation into biological nitrogen fixation, however, the fascinating intricacies and comparative relevance to other biochemical systems further motivates the study of this system. The enzyme committed to this task, nitrogenase, orchestrates an elegant unidirectional multiple electron reduction and activation of the nitrogen triple bond. Historically, mechanistic characterization of this enzyme has been difficult for a number of reasons; however, studies to date have revealed many aspects of the process as biochemical techniques have improved. Nitrogenase is an oxygen sensitive, complex two-component enzyme that is mechanistically pertinent to many other biochemical processes. . Presented here are studies revealing insight into substrate binding and the unique gated electron transfer mechanism of this fascinating enzyme.

CHAPTER 1

INTRODUCTION

Nitrogenase

The nitrogenase enzyme found in some bacteria and archaea is responsible for the multiple electron reduction of atmospheric nitrogen gas to ammonia (Figure 1.1). This energy demanding process, exemplified in the reaction below, requires the use of 16 MgATP and 8 reducing equivalents:[1, 2]

$$N_2 + 8H^+ + 16MgATP + 8e^- \rightarrow 2NH_3 + H_2 + 16MgADP + 16P_i$$

molybdenum-dependent nitrogenase represents the most thoroughly studied nitrogenase system. Substitutions of molybdenum for vanadium or iron also occur, but this discussion and research will focus on the molybdenum-dependant nitrogenase isolated from the diazotrophic bacteria, *Azotobacter vinelandii*. This system contains two complex metalloprotein components deemed the Fe protein and the MoFe protein, which must undergo multiple cycles of MgATP dependant association and dissociation events to deliver electrons from the Fe protein to the substrate binding and catalytic sites in the MoFe protein.[3] The Fe protein is the exclusive electron donor to the MoFe protein, both of which are thought undergo MgATP dependant conformational changes during catalysis.[3] Structurally, the 64kD Fe protein is a homodimer bridged by a single [4Fe-4S] cluster and has two sites for MgATP binding and hydrolysis, one in each subunit.[4] The

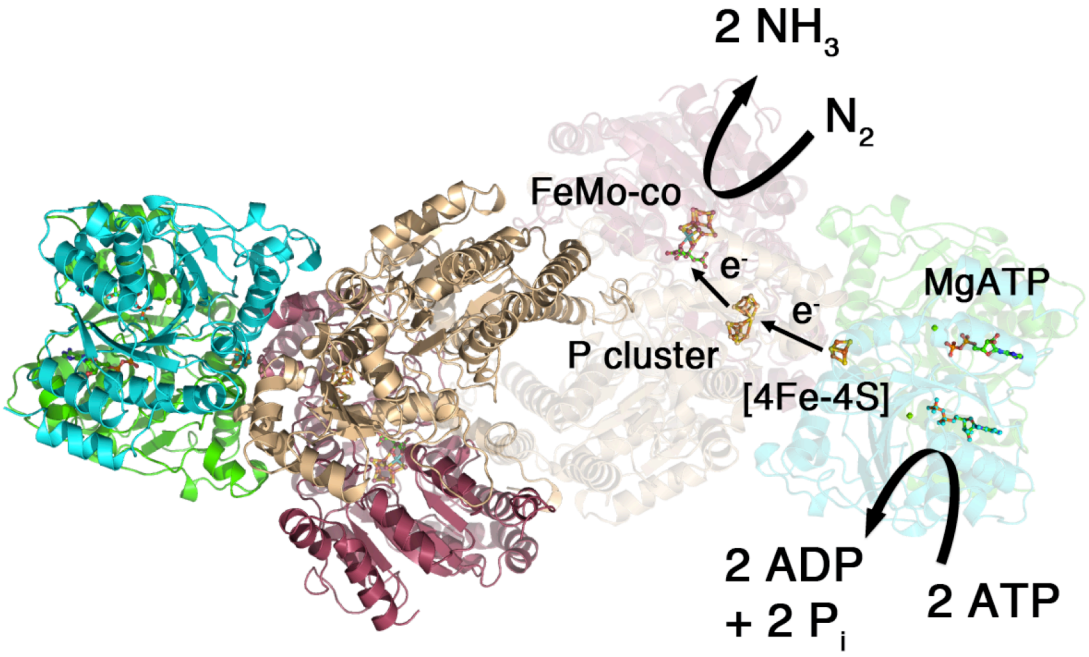


Figure 1.1. The structural representation of the nitrogenase MoFe protein - Fe protein complex stabilized by AlF_4. The transparent representation of one half of the complex shows the MgATP binding sites, and the electron transfer pathway from the [4Fe-4S] cluster of the Fe protein to the to the active site FeMo-cofactor via the P cluster intermediate. Figure generated from PDB file 1N2C

250kD MoFe nitrogenase is a $\alpha_2\beta_2$ heterotetramer that contains 2 [8Fe-7S] P clusters and 2 active site [7Fe-9S-C-Mo-homocitrate] FeMo-cofactors (Figure 1.1).[5] The FeMo-cofactor is unprecedented in nature and represents the only example of molybdenum incorporation into an iron-sulfur organometallo-cluster. The FeMo-cofactor is the site of substrate binding and reduction.[6] Catalysis is incumbent upon the interaction of the MoFe protein and the Fe protein to drive the sequential MgATP dependant intermolecular electron transfer from the Fe protein to the MoFe protein. During this process, the reduced Fe protein with its [4Fe-4S] cluster in the +1 oxidation state and two bound MgATP's, docks with the MoFe protein at a specific site near the P-cluster of

MoFe.[7] To prime the Fe protein for this process, an electron donor molecule such as ferredoxin or flavodoxin reduces the Fe protein [4Fe-4S] cluster,[8] and the binding of MgATP renders the Fe protein poised for complex formation with the MoFe protein. The interaction of the Fe protein and MoFe is thought to induce conformational changes in both proteins that facilitate the hydrolysis of MgATP, and concomitant inter and intra molecular electron transfer to deliver reducing equivalents to the active site.[7] Upon MgATP hydrolysis, the oxidized MgADP bound Fe protein disassociates to be regenerated for further rounds of electron transfer[9]. The MoFe protein P-clusters are thought to be intermediates in the electron transfer pathway between the [4Fe-4S] cluster of the Fe protein and the FeMo-cofactor active sites. This process only delivers one electron at a time, and the reduction of atmospheric nitrogen gas to ammonia requires at least six electrons, therefore multiple rounds of complex association and dissociation are necessary for nitrogen reduction. This intricate multiple electron reductase also has a promiscuous nature in that it can reduce a number of substrates other than nitrogen gas.[1] Other substrates include acetylene and cyanide, with cyanide also acting as an inhibitor, and the reduction of acetylene to ethylene being useful for assaying activity.[1] Investigations into the reduction of the alterative substrates may provide invaluable insight into the mechanism of catalysis.

Nitrogenase P-clusters and FeMo-cofactors

The three-dimensional molecular structure of the MoFe protein has been determined by X-ray crystallographic analysis.[10] Structural investigation has lead to major contributions to our current understanding of nitrogenase catalysis, and structural descriptions of the P-clusters and FeMo-cofactors (Figure 1.2) have been instrumental for developing models for substrate binding and reduction. The P-cluster can be described as two [4Fe-4S]

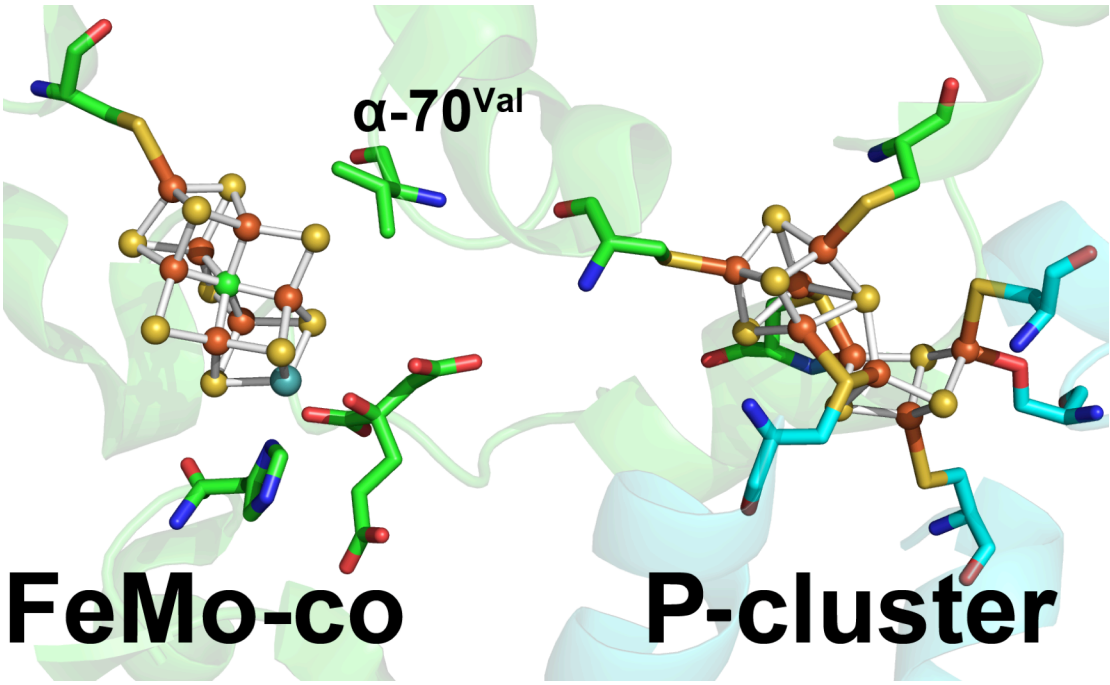


Figure 1.2. Ball and stick representations of the P-cluster and the FeMo-cofactor coordinated in the MoFe nitrogenase protein structure. The α-70^{Val} residue is labeled to show the proposed face of substrate binding. The residues shown in green are located in the alpha subunit while the residues shown in blue are in the beta subunit. The P-cluster spans the alpha-beta subunit interface. Image generated from PDB file 3U7Q.

clusters bridged by a sulfide in a shared corner, and is the only known naturally occurring [Fe-S] cluster that contains serinate-O (β-188^{Ser}) and amide-N (α-88^{Cys}) ligands.[11] In addition, this cluster is coordinated by six more typical cysteinate-S ligands across a pseudo two-fold axis that bridges the alpha and beta subunits of the MoFe protein (Figure 1.2). Each subunit contributes three cysteine residues, two from each coordinate as terminal ligands binding only one iron ion, and one from each coordinate as bridging sulfurs in the two [4Fe-4S] cubanes. Various studies have implicated the P-cluster as an intermediate in the electron transport pathway between the [4Fe-4S] cluster of the Fe protein and the FeMo-cofactor catalytic site.[3, 7, 12] Recent work has implied conformational changes induced by reduced Fe protein - MoFe protein complex formation, results in the all-ferrous resting state P cluster to become oxidized via intra molecular electron transfer to the FeMo-cofactor[7]. The oxidized P-cluster is then backfilled to its reduced all ferrous resting state via inter-molecular electron transfer from the Fe protein. Previous crystallographic studies have implicated redox associated structural changes to the P-cluster during rounds of catalysis.[11] These structural changes might be attributed to the required unidirectional gated electron flow, and proximity of key P-cluster ligands to FeMo-co ligands have been suggested to afford conformational sensing between the clusters.[13]

The FeMo-cofactor is an unprecedented natural [7Fe-9S-C-Mo-homocitrate] organometallo cluster. This cofactor can be best described as a [Mo-3Fe-3S] sub-cluster bridged to [4Fe-3S] partial cluster via three Fe bridging sulfides and a carbide moiety.[14] The molybdenum ion occupies a corner position of this cluster, and is additionally

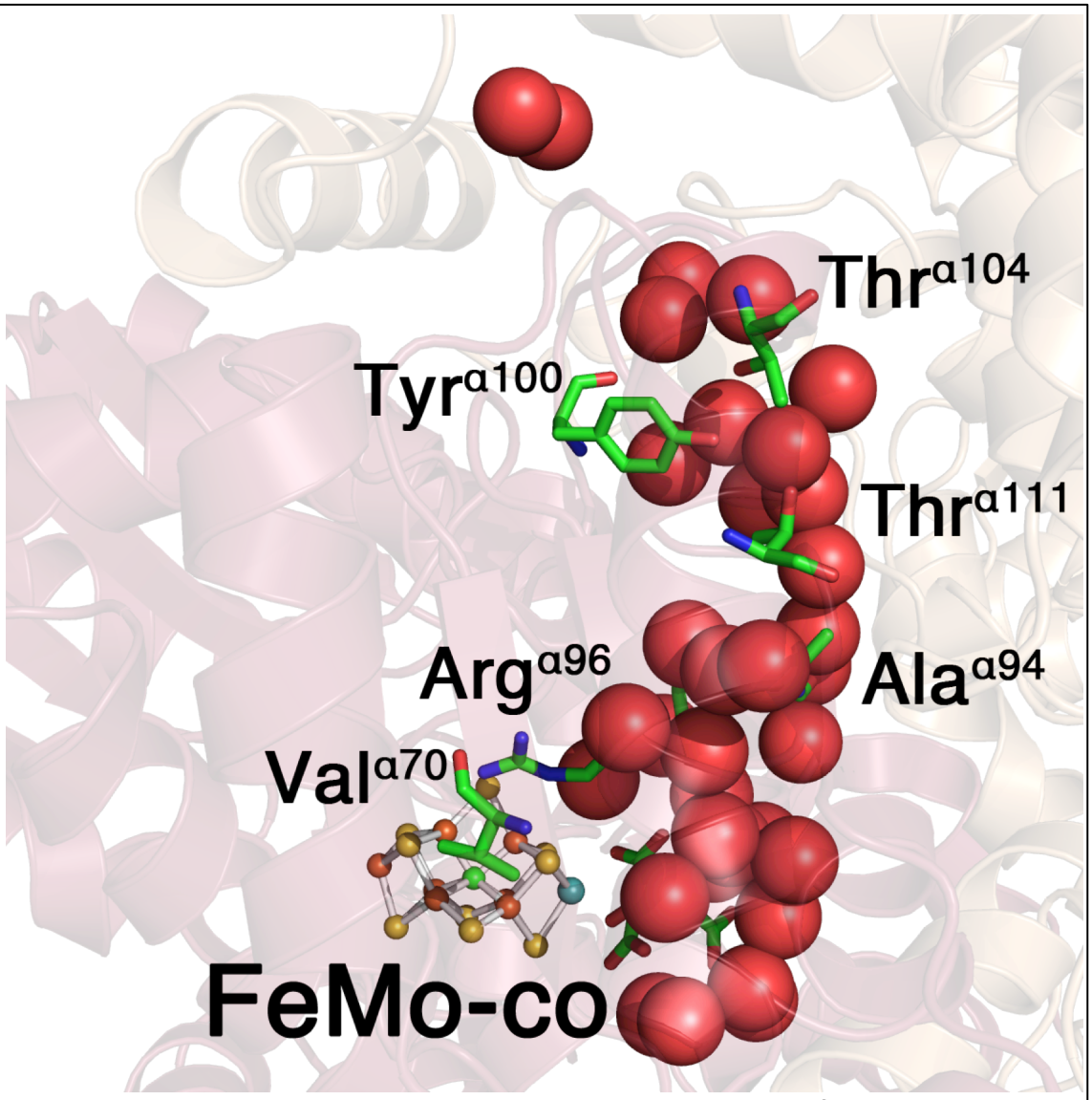


Figure 1.3. The proposed substrate channel accessing the active site of MoFe. Water molecules are represented as red spheres.

hexacoordinated with octahedral geometry by the hydroxyl and carboxyl groups from *R*-homocitrate, and by the delta nitrogen from α-442^{His} residue.[14] The only other coordinating amino acid is α-275^{Cys}, which is located on the opposite end of the cluster relative to the molybdenum.

The metal cluster possesses 4Fe faces that possess three-fold rotational symmetry. Various genetic, biochemical and spectroscopic studies have implicated one of these faces as the specific site for substrate binding and reduction.[1, 3, 15] This face is adjacent to α-70^{Val} and α-96^{Arg}, and these residues have been shown to spatially constrain the catalytic pocket of nitrogenase.[16] It has been reported that substitutions to α-70^{Val} (Figure 1.2) have been shown to control substrate access to the FeMo-co active site. Substitutions affording a larger pocket, result in a MoFe protein competent to reduce unconventional substrates such as propargyl alcohol, propyne, and 1-butyne.[1] Mutations that compress the pocket restrict reduction to only protons. These observations strongly imply this face as the site of substrate reduction.[1] Additionally, this FeS face has been reported to be directed toward a major solvent filled channel, which is thought to be a pathway for substrate access (Figure 1.3).[17] To further implicate this face as the site of substrate binding and reduction, several studies have applied a suite of advanced spectroscopic techniques to trap various substrates and intermediates binding during the catalytic cycle, and have implicated a specific iron (Fe6) as the site of substrate binding.[3] Molybdenum has not been implicated as a site for substrate binding, but the possibility remains that it may be involved the coordination of intermediates.

Research Directions

Industrial nitrogen fixation is costly, energy intensive, generates pollution and is sometimes a dangerous process. The over-application of artificial nitrogenous fertilizers can have disastrous consequences to ecosystems. Clearly there is a need to study biological nitrogen fixation to offset the negative consequences of anthropomorphic ammonia synthesis. Mechanistic characterization of nitrogenase enzymes based on structural and spectroscopic analysis has thus far been unsuccessful to fully describe the intricacies of the multiple electron reduction cycles. The FeMo-cofactor must accumulate at lest four reducing equivalents before nitrogen gas will bind, requiring the transient association of the electron donating Fe protein. This requirement creates a difficult situation to observe substrate binding via crystallographic techniques because the Fe protein cannot access the MoFe protein docking sites after crystallization has occurred. Consequently, a thrust to overcome this obstacle has been proposed through a concerted approach of innovative spectroscopic and structural analysis. Recent biochemical and spectroscopic studies have yielded intriguing results providing insight into how P cluster gated electron transfer occurs, and the binding of substrates and intermediates to the active site. These results suggest that it is possible to structurally characterize poised states and mechanistic intermediates that will drastically impact our understanding of how the nitrogenase apparatus orchestrates the complex electron transfer events that drive the catalytic reduction of atmospheric nitrogen. The work presented here builds on many years of research and may provide insight into some of these outstanding unknowns.

Chapter 2 describes research into a unique MoFe protein variant capable of substrate reduction in the absence of the Fe protein, with the electrons instead being supplied by a by a Eu^{II}-polyaminocarboxylate complex. A crystal structure of this unique variant was obtained and insight was gained into the mechanism of electron transfer in nitrogenase. Chapter 3 describes to overcoming obstacle through creativity, by developing a new crystallography technique to probe structural changes to the P-cluster at defined midpoint potentials. Chapter 3 reports insight into the mechanistically relevant substrate acetylene interacting with the FeMo-co active site through structural and computational analysis. Finally, chapter 5 revisits Fe protein independent electron transfer in the nitrogenase MoFe protein using photoreduction by cadmium sulfide (CdS) nanocrystals. Nitrogenase is an extremely recalcitrant system to study, however, the work described herein will provide some insight into this biological enigma.

CHAPTER TWO

FE PROTEIN-INDEPENDENT SUBSTRATE REDUCTION BY NITROGENASE MOFE PROTEIN VARIANTS

Contribution of Authors and Co-Authors

Manuscript in Chapter 2

Author: Karamatullah Danyal

Contributions: Growth, purification and kinetic studies

Co-Author: Andrew J. Rasmussen

Contributions: Growth, purification and kinetic studies

Co-Author: Stephen M. Keable

Contributions: Protein crystallization and structure determination

Co-Author: Boyd S. Inglet

Contributions: Growth, purification and kinetic studies

Co-Author: Sudipta Shaw

Contributions: Growth, purification and kinetic studies

Co-Author: Oleg A. Zadvornyy

Contributions: Structure determination

Co-Author: Simon Duval

Contributions: Growth, purification and kinetic studies

Co-Author: Dennis R. Dean

Contributions: PI of lab that provided mutant strains

Co-Author: Simone Raugei

Contributions: Computational analysis

Co-Author: John W. Peters

Contributions: Corresponding author

Co-Author: Lance C. Seefeldt

Contributions: Corresponding author

Manuscript Information Page

Karamatullah Danyal, Andrew J. Rasmussen, Stephen M. Keable, Boyd S. Inglet, Sudipta Shaw, Oleg A. Zadvornyy, Simon Duval, Dennis R. Dean, Simone Raugei, John W. Peters, Lance C. Seefeldt
Biochemistry
Status of Manuscript:
____ Prepared for submission to a peer-reviewed journal
___ Officially submitted to a peer-review journal
____ Accepted by a peer-reviewed journal
_X_ Published in a peer-reviewed journal

Published by the American Chemical Society

CHAPTER 2

FE PROTEIN-INDEPENDENT SUBSTRATE REDUCTION BY NITROGENASE MOFE PROTEIN VARIANTS

Abstract

The reduction of substrates catalyzed by nitrogenase normally requires nucleotide-dependent Fe protein delivery of electrons to the MoFe protein, which contains the active site FeMo-cofactor. Here, it is reported that independent substitution of three amino acids (ß-98$^{Tyr\rightarrow His}$, α-64$^{Tyr\rightarrow His}$, and ß-99$^{Phe\rightarrow His}$) located between the P cluster and FeMo-cofactor within the MoFe protein endows it with the ability to reduce protons to H_2, azide to ammonia, and hydrazine to ammonia without the need for Fe protein or ATP. Instead, electrons can be provided by the low potential reductant polyaminocarboxylate ligated Eu(II) (E_m -1.1 to -0.84 V vs NHE). The crystal structure of the ß-98$^{Tyr\rightarrow His}$ variant MoFe protein was determined, revealing only small changes near the amino acid substitution that affect the solvent structure and immediate vicinity between the P-cluster and the FeMo-cofactor, with no global conformational changes observed. Computational normal mode analysis on the nitrogenase complex reveal coupling in the motions of the Fe protein and the region of the MoFe protein with these three amino acids, which suggests a possible mechanism for how Fe protein might communicate subtle changes deep within the MoFe protein subtle changes that profoundly affect intramolecular electron transfer and substrate reduction.

Chapter Introduction

Mo-dependent nitrogenase catalyzes biological dinitrogen (N_2) fixation to ammonia (NH_3) with the minimum reaction stoichiometry shown in eq. 1:[2, 18]

$$N_2 + 8e^- + 16MgATP + 8H^+ \rightarrow 2NH_3 + H_2 + 16MgADP + 16Pi \quad \text{(eq. 1)}$$

Nitrogenase consists of two component proteins called the iron (Fe) protein and the molybdenum-iron (MoFe) protein (Figure 2.1).[2] The MoFe protein is an $\alpha_2ß_2$ heterotetramer consisting of two catalytic αß units, each containing a P cluster [8Fe-7S] and a FeMo-cofactor (FeMo-co; [7Fe-9S-1Mo-C-homocitrate]).[14, 19] The Fe protein is a homodimer with a [4Fe-4S] cluster bridging the two subunits and an ATP binding site on each subunit.[4] To achieve the complete reduction of N_2 at the FeMo-co in the MoFe protein, a Fe protein must transiently bind to the MoFe protein.[20] During this association of the two proteins, a single electron is passed from the Fe protein to FeMo-co, followed by the hydrolysis of the two ATP molecules bound to the Fe protein.[21] Recent evidence suggests that the electron transfer reaction proceeds in two steps with the first step being transfer of an electron from the P cluster to the FeMo-co, followed by transfer of an electron from the Fe protein to the oxidized P cluster (termed a "deficit spending" electron transfer mechanism).[7] ATP hydrolysis follows the electron transfer events, with release of the Pi and finally dissociation of the Fe protein from the MoFe protein.[21, 22] The two ADP molecules bound to the released Fe protein are exchanged with ATP and the oxidized Fe protein is reduced by dithionite (*in vitro*) or flavodoxin/ferredoxin (*in*

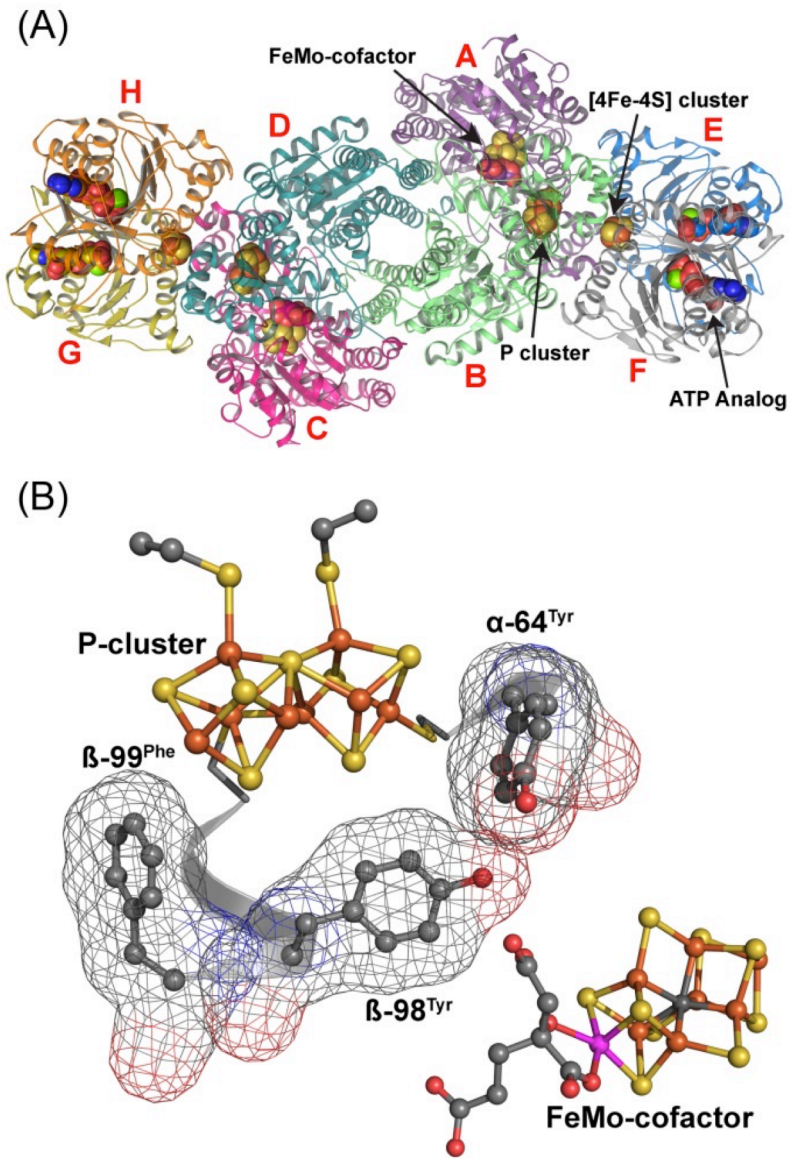


Figure 2.1. Nitrogenase and metal clusters. (A) Structure of the nitrogenase complex (PDB entry: 2AFK). Each unit is labeled from A to H according to the PDB numbering. (B) The three amino acid residues relevant to the Fe protein-independent reduction of the substrates (N_2H_4, N_3^- and H^+) by the MoFe protein are shown in ball and stick representation with the mesh representing the van der Waals surface. Also shown are the P cluster and FeMo-co in ball and stick representation. The linkage from α-64^{Tyr} to the P-cluster ligand α-62^{Cys} and from β-98^{Tyr} to the P cluster ligand β-95^{Cys} are also shown. Atoms colors are Fe in rust, S in yellow, C in grey, O in red, and Mo is magenta.

vivo).[2, 23] This catalytic cycle is repeated 8 times to achieve the accumulation of sufficient electrons for the activation and reduction of N_2 and the stoichiometric release of H_2.[2, 18] Fe protein is the only reductant known to support N_2 reduction by the MoFe protein, suggesting it plays a pivotal role in the mechanism beyond just donating electrons. Two recent reports have revealed that it is possible to deliver electrons directly to the MoFe protein in the absence of the Fe protein with reduction of a few substrates other than N_2. In one case, a Ru-ligand complex was covalently attached to the MoFe protein, and it was possible to photo-induce electron transfer into the MoFe protein to achieve very low rates of reduction of the non-physiological substrate acetylene to ethylene and cyanide to methane.[24, 25] In another case, substitution of a single amino acid within the MoFe protein located between the P-cluster and FeMo-co (ß-$98^{Tyr\rightarrow His}$) allowed a Eu-ligand complex in solution to deliver electrons to the MoFe protein to achieve reduction of hydrazine to ammonia at rates near those observed when electrons are delivered from the Fe protein.[26] This finding suggested that amino acids located between the P cluster and FeMo-cofactor within the MoFe protein might play an important but poorly understood role in regulating electron transfer events that support substrate reduction at FeMo-co. Here, we report that independent substitution of three amino acids co-located between the P cluster and FeMo-co (ß-$98^{Tyr\rightarrow His}$, α-$64^{Tyr\rightarrow His}$, and ß-$99^{Phe\rightarrow His}$) endows the resultant MoFe proteins with the ability to reduce the substrates hydrazine, azide and H^+ at significant rates using Eu(II)-ligands as reductant without the need for the Fe protein. The crystal structure of the ß-$98^{Tyr\rightarrow His}$ MoFe protein was solved, revealing subtle

conformational changes and altered solvent structure in close proximity to the FeMo-co. These small changes between the P cluster and FeMo-co may mimic conformational changes requisite to catalysis. Calculations done on the Fe protein-MoFe protein complex reveal a mechanical coupling between the Fe protein and the region containing the ß-98^{Tyr}, α-64^{Tyr}, and ß-99^{Phe} amino acids within the MoFe protein providing a possible mechanism for the communication between the Fe protein and key determinants of MoFe protein intramolecular electron transfer.

Materials and Methods

All reagents, unless stated otherwise, were purchased from Sigma-Aldrich Chemicals (St. Louis, MO). MoFe proteins were expressed in *Azotobacter vinelandii* strains DJ939 (ß-98 $^{Tyr\rightarrow His}$), DJ1956 (ß-99 $^{Phe\rightarrow His}$), and DJ1957(α-64 $^{Tyr\rightarrow His}$) that were grown as described previously.[27] The MoFe proteins from each strain were purified, with some modifications, as described to greater than 95% purity and confirmed by sodium dodecyl sulfate-polyacrylamide gel electrophoresis analysis using Coomassie blue staining.[27] Manipulation of proteins was done in septum-sealed serum vials under argon atmosphere. All transfers of gases and liquids were done using gastight syringes. Azide reduction, H_2 evolution and N_2H_4 reduction activities were determined as described earlier.[28] NH_3 was quantified using a fluorescence method with o-pthalaldehyde as described previously.[28] For all assays, Eu(II)-L was generated by electrochemical reduction, as described previously.[29]

Crystallization trials were performed on ß-98$^{Tyr\rightarrow His}$ MoFe protein that was concentrated to ~30 mg/mL and stored in the purification buffer. All trials were done under anaerobic conditions in a nitrogen atmosphere glove box (UniLAB, M. Braun) using a micro-capillary batch diffusion method.[4, 30] Crystallization was accomplished as previously described using a precipitating solution that contained 30% polyethylene glycol (PEG) 4000, 100 mM Tris HCl pH 8.0, 190 mM sodium molybdate and 1 mM sodium dithoionite.[31] Crystals of dark brown color with the approximate dimensions - 100 x 200 x 200 µm were observed after 4-6 weeks of growth. The crystals were cryo-protected by diffusion of mother liquor doped with ~15% glycerol. Crystals were harvested under a stream of continuous argon on rayon loops and immediately flash cooled in liquid nitrogen. Data were collected on beam line (BL-9-2) at the Stanford Synchrotron Radiation Laboratory under a continuous flow of liquid nitrogen at ~100 K. A data set was collected at λ=0.97, on a MAR 325 detector up to resolution 1.97 Å, and was scaled and integrated using the HKL2000 software package.[32]

The unit cell parameters of the collected data were nearly isomorphous to the published native structure (PDB ID: 3U7Q).[14] Initial rigid body fitting and refinement was carried out using AutoMR of the CCP4 suite of programs. Calculation of electron density maps and model fitting was accomplished by using coot and the model was refined using REFMAC5 to 1.97 Å resolution.[33] The final model was built with a crystallographic *R* of 21.5, with 95.6 % of the residues in the most favored Ramachandran regions, and 4.2 % in additionally allowed regions (Table S2.4). The PDBeFold Structure Similarity server at the European Bioinformatics Institute (http://www.ebi.ac.uk/msd-srv/ssm/) was used to

determine an average root-mean-square deviation (RMSD) of 0.2Å between analogous α-carbons of the ß-98$^{Tyr\rightarrow His}$ MoFe variant and the wild-type MoFe structure (3U7Q).

To characterize the mechanical aspects of the long-time scale dynamics of the nitrogenase complex, we performed a normal mode analysis based on the anisotropic Gaussian network model.[34, 35] The nitrogenase complex was represented by beads centered at the position of the alpha carbons. According to this model, two beads are connected with a harmonic spring if they are within a cutoff distance, R_{cut}, and not connected otherwise. To improve the stability of the model, in the present study the force constant, k, of the spring was chosen to vary smoothly from k_0 to zero using the sigmoidal switching function around R_{cut} given in eq. 2.[36, 37]

eq. 2 $$k(r_{ij}) = \frac{k_0}{1 + e^{(r_{ij} - R_{cut})/\gamma}}$$

where r_{ij} is the distance between the beads i and j and γ is the width of the switching function. We used a cutoff distance R_{cut} = 12 Å, with a width for the switching function of 2 Å. Different choices gave consistent results, in agreement with previous reports. According to this model, the potential energy function of the protein is given by eq. 3:

eq. 3 $$V = \frac{1}{2}\sum_{i,j=1}^{N} \sum_{\alpha,\beta=x,y,z} k(r_{ij})\, \Delta r_i^{\alpha} \Gamma_{ij}^{\alpha\beta} \Delta r_j^{\beta}$$

where Δr_i^{α} is the a component ($\alpha = x, y$, and z) of the position vector $\mathbf{r_i}$ for the i-th alpha carbon and $\mathbf{\Gamma}$ is the so-called contact matrix. The off-diagonal and diagonal elements of the contact matrix are given by eqs. 4 and 5, respectively:

eq. 4 $$\Gamma_{ij}^{\alpha\beta} = \frac{k(r_{ij})}{k_0} \frac{\mathbf{r_i} \cdot \mathbf{e}_\alpha}{|\mathbf{r_i}|} \frac{\mathbf{r_j} \cdot \mathbf{e}_\beta}{|\mathbf{r_j}|}$$

eq. 5 $$\Gamma_{ii}^{\alpha\alpha} = -\sum_{\substack{k=1 \\ k\neq i}}^{N} \sum_{\beta} \Gamma_{ik}^{\alpha\beta} - \sum_{\beta\neq\alpha} \Gamma_{ii}^{\alpha\beta}$$

where $\mathbf{e}_\alpha$ is the unit vector along the Cartesian direction α.

The correlation between the fluctuations of the protein residues were analyzed in terms of the covariance matrix **C**, whose elements $C_{ij} = \sum_\alpha \langle \Delta r_i^\alpha \Delta r_j^\alpha \rangle$, were calculated from the eigenvector decomposition of the inverse of the contact matrix (eq. 6):[34]

eq. 6 $$C_{ij} = \frac{3k_B T}{k_0} \sum_\alpha [\Gamma^{-1}]_{ij}^{\alpha\alpha} = \frac{3k_B T}{k_0} \sum_{k=7}^{3N} \sum_\alpha \lambda_k^{-1} [\mathbf{v_k} \cdot \mathbf{v_k^T}]_{ij}^{\alpha\alpha}$$

where λ_k and $\mathbf{v}_k$ are the *k*-th eigenvalue and eigenvector of the contact matrix. The six zero-frequency modes corresponding to rigid body translations and rotations of the nitrogenase complex are excluded from the summation over the normal modes. The diagonal elements of the covariance matrix C_{ii} are proportional to the beta factor of the amino acid residues, $B_i = 8\pi^2 C_{ii}/3$. As can be seen from eq. 6, the spring constant k_0 acts as a mere scaling factor for the atomic fluctuations and the beta factors, and its value was chosen in order to reproduce the *average* magnitude of the crystallographic beta factors. The model is able to reproduce faithfully the *relative* magnitude of the experimental beta factors (Figure S1), making us confident that it is also able to describe the overall large amplitude motions of the nitrogenase complex. The calculations were performed on the crystal structure of the complex between the Fe protein and the MoFe

protein from *Azotobacter vinelandii* with an ATP analog and ADP bound to the Fe protein (protein data bank codes 2AFK and 2AFI, respectively).[38]

Results and Discussion

The recent preliminary finding that substitution of ß-98$^{Tyr\rightarrow His}$ in the MoFe protein allows it to reduce hydrazine to ammonia without participation of the Fe protein or ATP, instead with electrons coming from Eu^{II}-DTPA, points to participation of the protein around ß-98^{Tyr} in the MoFe protein in regulating electron transfer between the P cluster and FeMo-co or in the reactivity of FeMo-co.[26] To further explore this possibility, we have prepared MoFe proteins having independent amino acid substitutions for three amino acids co-localized between the P cluster and FeMo-co (ß-98$^{Tyr\rightarrow His}$, ß-99$^{Phe\rightarrow His}$, and α-64$^{Tyr\rightarrow His}$) (Figure 2.1). The amino acid substitutions did lower the proton reduction to H_2 rate driven by the Fe protein and ATP to 1100 ± 25 nmol of H_2/min/mg for ß-98$^{Tyr\rightarrow His}$, and to below detection for the ß-99$^{Phe\rightarrow His}$ and α-64$^{Tyr\rightarrow His}$ variants. The wild type rate is ~2000 nmol of H_2/min/mg MoFe protein.

Activity Assays

The three variant MoFe proteins were tested for their ability to reduce substrates without Fe protein, but instead with electrons coming from Eu(II)-ligands. For these assays,

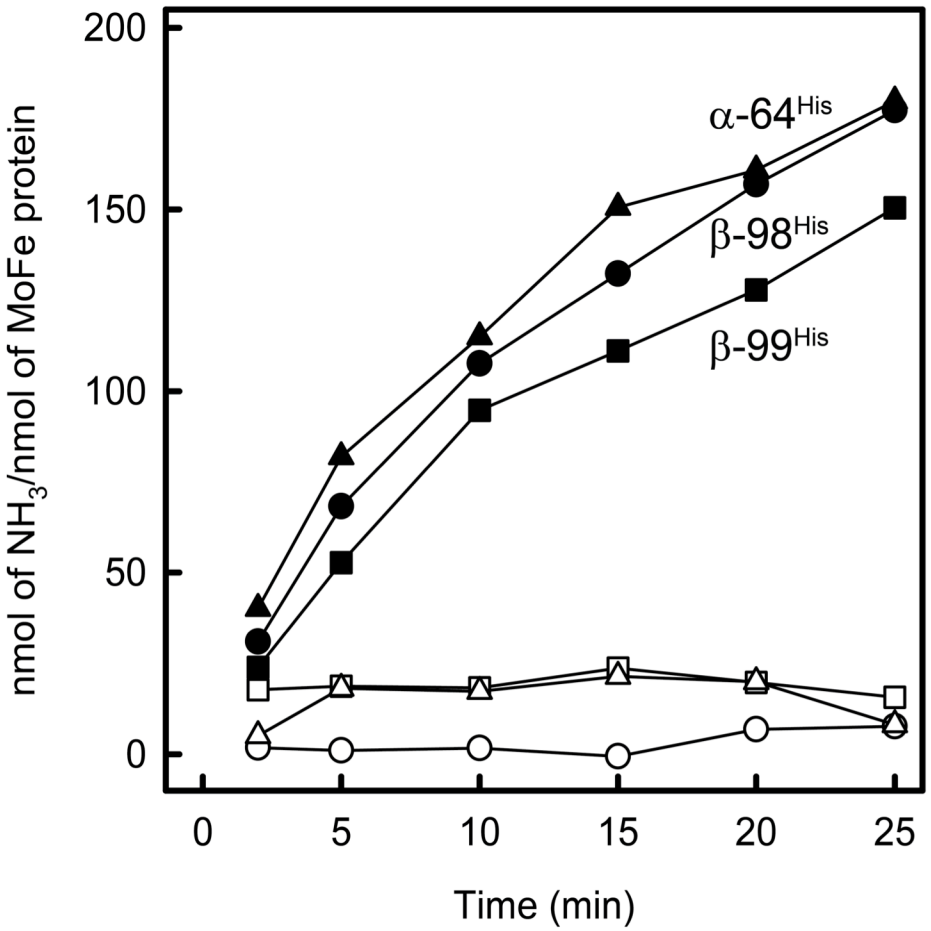


Figure 2.2. Fe protein independent hydrazine reduction catalyzed by MoFe protein variants. Time course of the reduction of hydrazine to ammonia reported as nmol of ammonia formed per nmol MoFe protein catalyzed by α-64^{His} (▲), β-98^{His} (●), or β-99^{His} (■) variant MoFe proteins. The corresponding open symbols are the no protein controls. The assay was performed with a final concentration of 1 mM Eu(II)-DTPA, 2.9 nmol (1.83 μM) MoFe protein and 100 mM hydrazine at 25°C.

Eu(II) and DTPA were added simultaneously to initiate the assay with no Fe protein added. Figure 2.2 shows the time-dependence for hydrazine (N_2H_4) reduction to ammonia

(NH_3) for the three variant proteins with rates ranging from 40 to 170 nmol H_3/nmol MoFe protein over 25 min. Activity was dependent on addition of Eu(II), DTPA, hydrazine, and MoFe protein. The reduction of hydrazine (N_2H_4) is a unique property of these variant MoFe proteins compared to the wild type MoFe protein alone, which is unable to reduce hydrazine with Eu-L as electron donor.

When the hydrazine reduction assay with Eu-DTPA as reductant was conducted for short times (2 min), high activity could be estimated because the Eu-DTPA was stable for only short times. Under these optimal conditions, the maximum specific activity for hydrazine reduction at 100 mM hydrazine was found to be 295 ± 15 nmol of NH_3/min/mg of MoFe protein for α-64$^{Tyr\rightarrow His}$, 198 ± 3 nmol of NH_3/min/mg of MoFe protein for ß-98$^{Tyr\rightarrow His}$, and 110 ± 2 nmol of NH_3/min/mg of MoFe protein for ß-99$^{Phe\rightarrow His}$. These rates ofhydrazine reduction compare to the rate of 320 nmol of NH_3/min/mg of MoFe protein catalyzed by the wild-type MoFe protein with Fe protein as the electron donor.

For the ß-98$^{Tyr\rightarrow His}$, ß-99$^{Phe\rightarrow His}$, and α-64$^{Tyr\rightarrow His}$ MoFe protein variants, the rate of reduction of hydrazine was dependent on the concentration of Eu(II)-DTPA (Figure S2), with saturation being approached above 1 mM Eu(II)-DTPA. These findings indicate that it is possible to saturate for the reductant and that there is a finite binding affinity.

In addition, the rates of hydrazine reduction were dependent on the concentration of hydrazine (Figure 2.3). Fits of the data to the Michaelis-Menten equation gave K_m values of ~48 mM for α-64$^{Tyr\rightarrow His}$, 21 mM for ß-98$^{Tyr\rightarrow His}$, and 17 mM for ß-99$^{Phe\rightarrow His}$. V_{max} values were found to be ~490 nmol NH_3/min/mg MoFe protein for α-64$^{Tyr\rightarrow His}$, 250 nmol NH_3/min/mg MoFe protein for ß-98$^{Tyr\rightarrow His}$, and 160 nmol NH_3/min/mg of MoFe protein

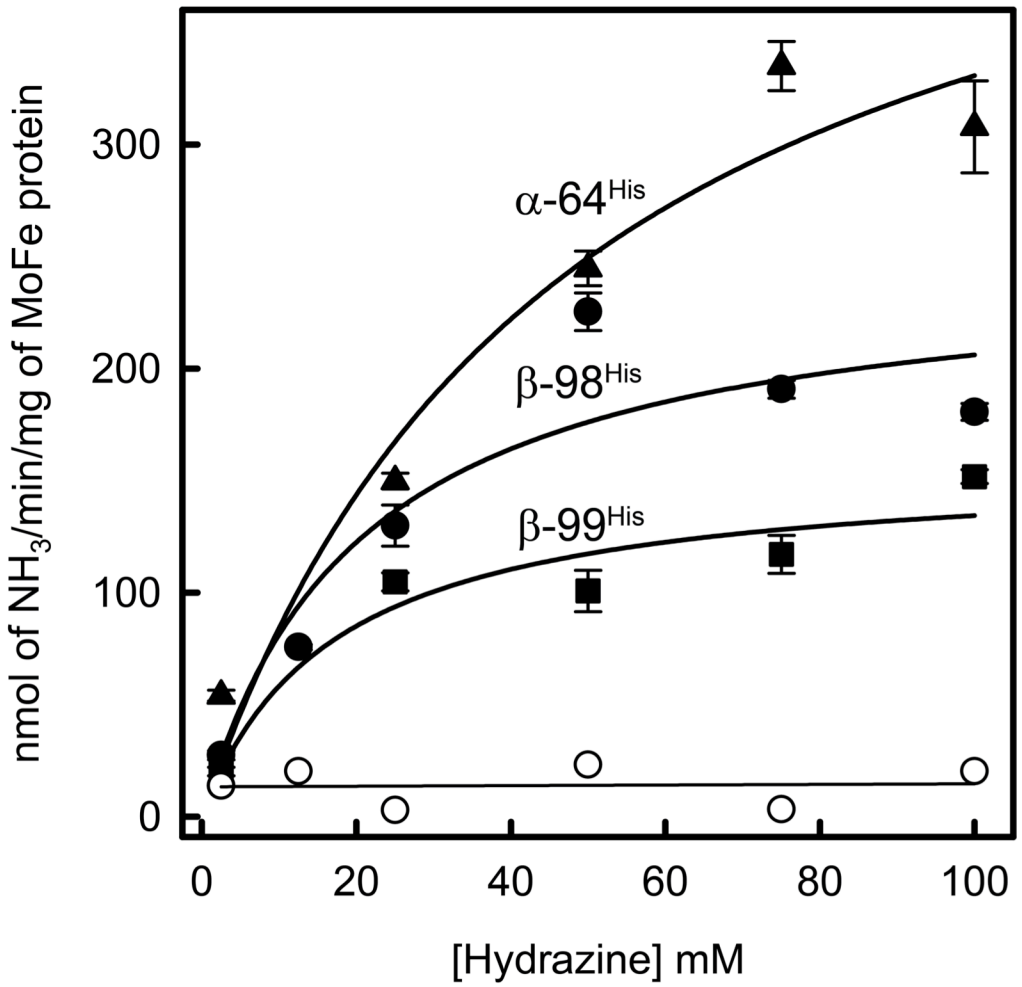


Figure 2.3. Concentration dependence of hydrazine on MoFe protein substrate reduction. The nmol of ammonia per nmol MoFe protein for the α-64^{His} (▲), β-98^{His} (●), and β-99^{His} (■) variants as a function of hydrazine concentration is shown. The open symbol corresponds to a no protein background control. All assays were conducted for two minutes at 25°C with a final concentration of 1 mM Eu^{II} DTPA, 100 mM hydrazine, and 2.9 nmols (1.83 μM) MoFe protein. The data were fit to Michaelis-Menten equation (solid lines) using SigmaPlot with r^2 values of 0.94, 0.87, and 0.91 for the α-64^{His}, β-98^{His}, and β-99^{His} MoFe protein data, respectively.

for ß-99$^{Phe\rightarrow His}$. The ß-98$^{Tyr\rightarrow His}$, ß-99$^{Phe\rightarrow His}$, and α-64$^{Tyr\rightarrow His}$ variant MoFe proteins were found to reduce azide (N_3^-) to ammonia (monitored) with Eu(II)-DTPA as electron donor (Table 1). The reduction midpoint potential of Eu(II) can be modified by changing the polyaminocarboxylate ligand (DTPA, EGTA, EDTA). The $Eu^{III/II}$-DTPA, $Eu^{III/II}$-EGTA, and $Eu^{III/II}$-EDTA redox couples have reduction potentials of -1.14, -0.88, and -0.84 Vversus the normal H_2 electrode (NHE), respectively.[29] All three ligand complexes with Eu(II) were examined with the three variant proteins for reduction of azide to ammonia (Table 2.1). For some of the variants, the EGTA and EDTA complexes with Eu(II)

Table 2.1. Product formation of MoFe protein variants using Eu(II)-L as reductant. Both the hydrazine and azide assays were conducted at 30^o C for 20 min, while the proton assays were conducted for 40 minutes at 30^o C. Hydrazine concentration was 100 mM and azide concentration was 10 mM. All assays were performed at pH 7.0. ND = none detected.

Protein	Hydrazine (nmol of NH_3/nmol MoFe protein)	Azide (nmol of NH_3/nmol MoFe protein)			Proton (nmol of H_2/nmol MoFe protein)
	Eu-DTPA	Eu-DTPA	Eu-EGTA	Eu-EDTA	Eu-EDTA
α-64^{His}	159 ± 7	26 ± 2	36 ± 5	40 ± 7	ND
ß-98^{His}	156 ± 2	30 ± 1	25 ± 2	19 ± 4	63 ± 6
ß-99^{His}	127 ± 5	ND	33 ± 3	22 ± 2	ND

showed higher rates of azide reduction. The Eu(II)-DTPA complex catalyzes proton reduction to form H_2 even in the absence of enzyme, whereas the Eu(II)-EDTA complex does not. This allowed the Eu(II)-EDTA complex to be examined as a source of electrons for proton reduction to form H_2 for the three proteins. Only the ß-$98^{Tyr\rightarrow His}$ protein showed significant H_2 evolution rates above background.

Structural Analysis

The structure of the ß-$98^{Tyr\rightarrow His}$ MoFe protein was determined and refined to 1.97 Å resolution and was compared to the structure of the wild type MoFe protein (3U7Q 1.0 Å).[14] Subtle structural differences were observed in the immediate vicinity of the amino acid substitution and in the solvent structure immediately around the FeMo-co. Most notable with respect to the later is ~1.5 Å difference in the position of a water molecule coordinating homocitrate resulting from the differences in the H-binding groups of Tyr and His at the ß-98 position (Figure 2.4). The histidine residue in the variant refines in a slightly different orientation relative to the tyrosine in the wild-type MoFe protein, and may be better posed for electron transfer due to the δ orbital dominance of this residue relative to the π orbital dominance of tyrosine. The change in side chain pKa's may also have an effect on the active site electrostatic environment and electron transfer pathway. The findings above reveal that it is possible to create a MoFe protein through amino acid substitutions that can reduce a number of substrates without the Fe protein and ATP. This suggests that these substitutions might regulate electron transfer from the P-cluster

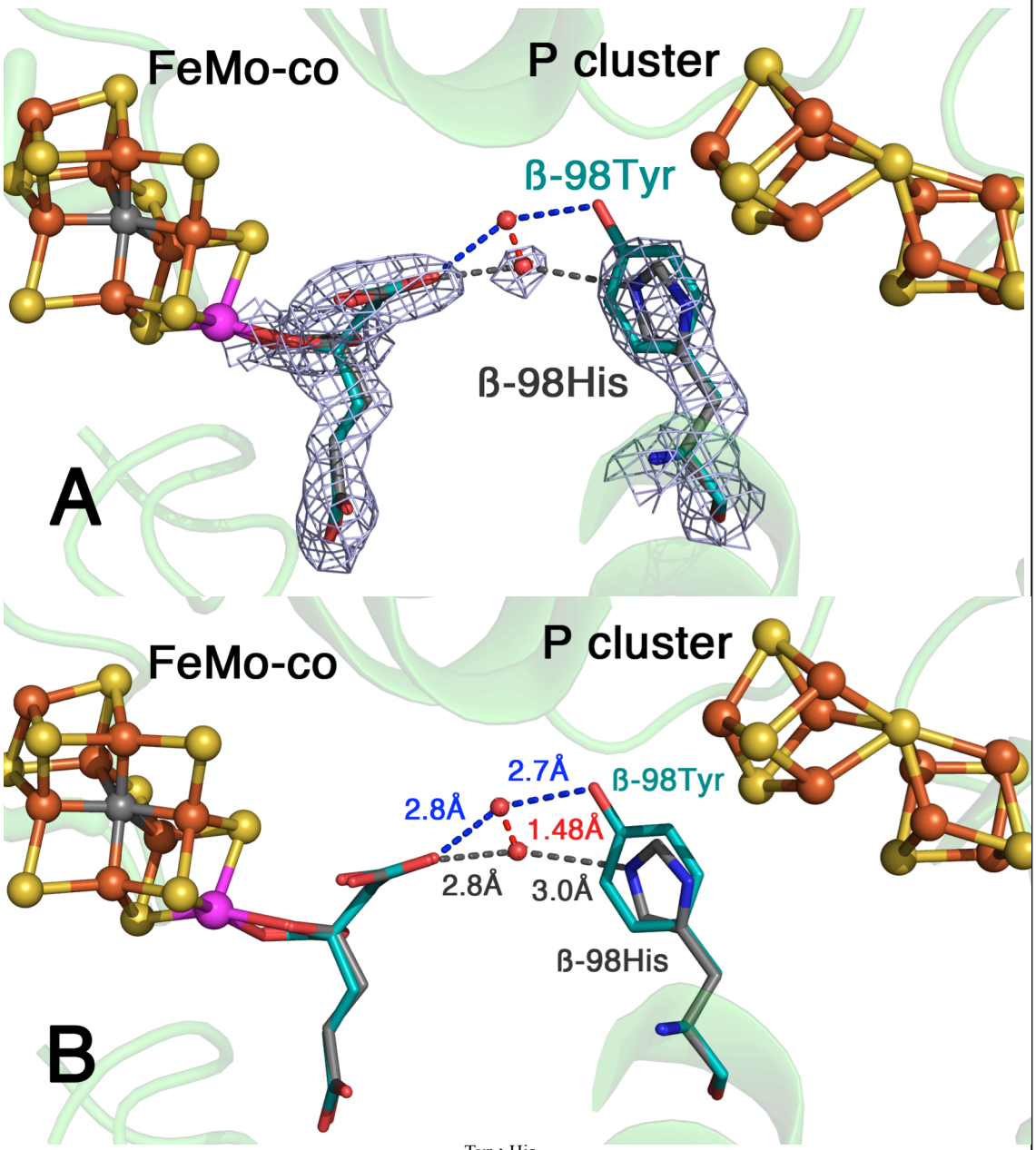


Figure 2.4. Crystal structure of the ß-98$^{Tyr\rightarrow His}$ variant MoFe protein. (Panel A) Shown is the experimental electron density superimposed with the wild-type MoFe protein (3U7Q). Subtle differences in structures between the two proteins is shown. (Panel B) View of the ß-98$^{Tyr\rightarrow His}$ variant structure superimposed with the wild type structure (3U7Q), highlighting the change in the solvent structure adjacent to the FeMo-cofactor.

to FeMo-co and/or the reactivity of FeMo-co. The nature of these conformational changes remain elusive, but the results from the present work point to possible participation of amino acids located between the P-cluster and FeMo-co.

Computational Analysis

To further explore the possible communication between the Fe protein and the MoFe protein, the vibrational normal modes that describe the large-amplitude motions of the nitrogenase complex were calculated according to a coarse-grained description of the proteins. A covariance analysis of the displacement of amino acid residues reveals a cross correlation between the motion of the two Fe proteins (Figure S3) suggesting that the motion of one of the two Fe proteins causes a response in the region between the P cluster and the FeMo-co. In particular, motion of residues α-64^{Tyr}, ß-98^{Tyr}, and ß-99^{Phe} in the MoFe protein correlates with the motion of the Fe protein. Figure 5 displays the correlation between these residues and the rest of the nitrogenase complex. As can be seen, there is a trivial in-phase correlation between the motion of residues α-64^{Tyr}, ß-98^{Tyr}, and ß-99^{Phe} and the neighbor residues within the MoFe protein, which decays quickly in space. Remarkably, Figure 2.5 shows a high degree of out-of-phase correlation between these residues and the Fe proteins. The normal mode contributing most corresponds to an out-of-phase rolling motion of the Fe proteins on the surface of the MoFe protein (Figure 2.6). These results suggest a dynamic coupling between the motion of the Fe protein and the MoFe protein region lying between the P cluster and FeMo-co,

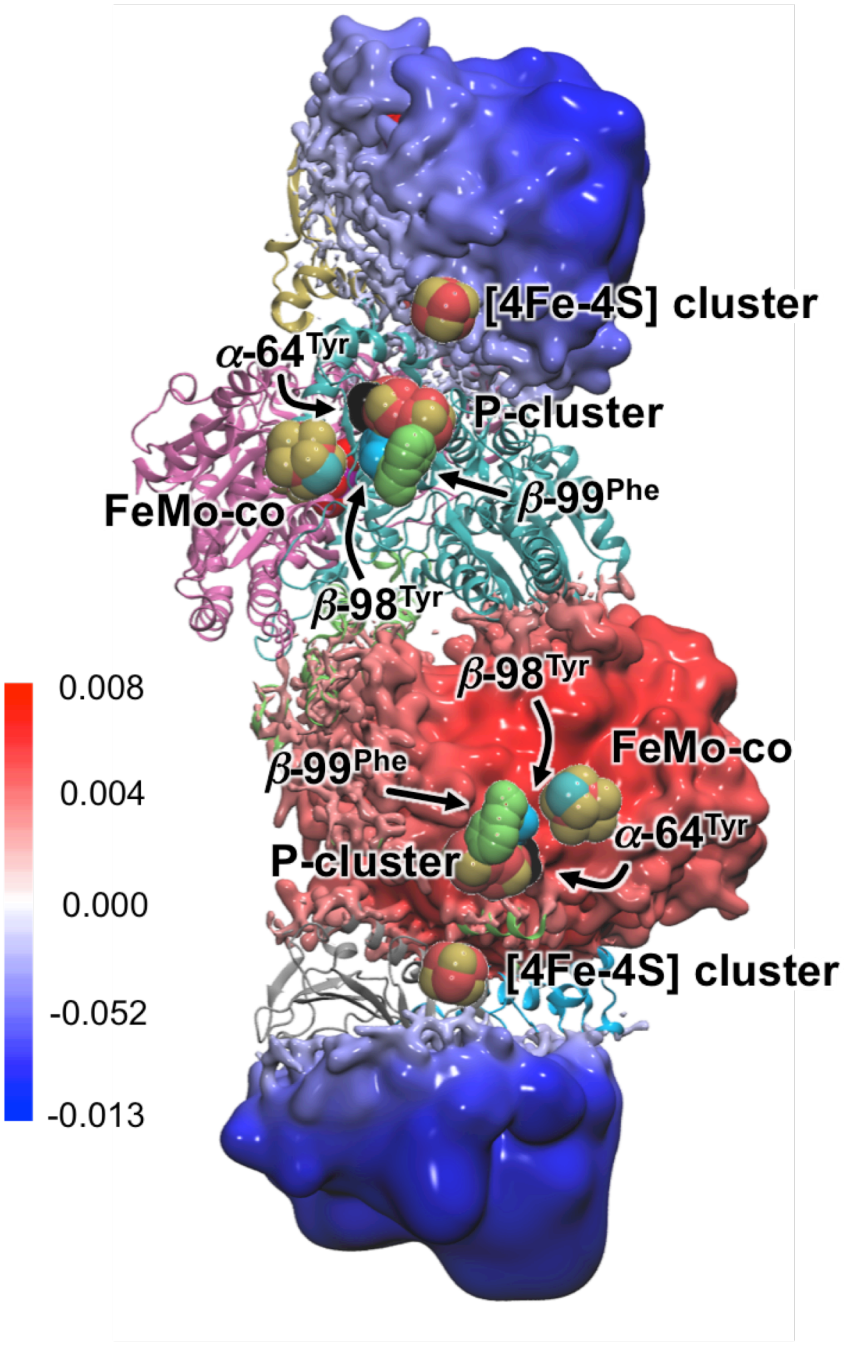


Figure 2.5. Mechanical coupling between residues α-64^{Tyr}, ß-98^{Tyr}, and ß-99^{Phe} and the rest of the MoFe protein/Fe protein complex. Regions of correlation and anti-correlation are enclosed by red and blue surfaces, respectively. The extent and the color scale of the surfaces correspond to the average of the values of covariance matrix elements (in Å^2) for the three residues. The locations of the metal clusters and α-64^{Tyr}, ß-98^{Tyr}, and ß-99^{Phe} residues are shown.

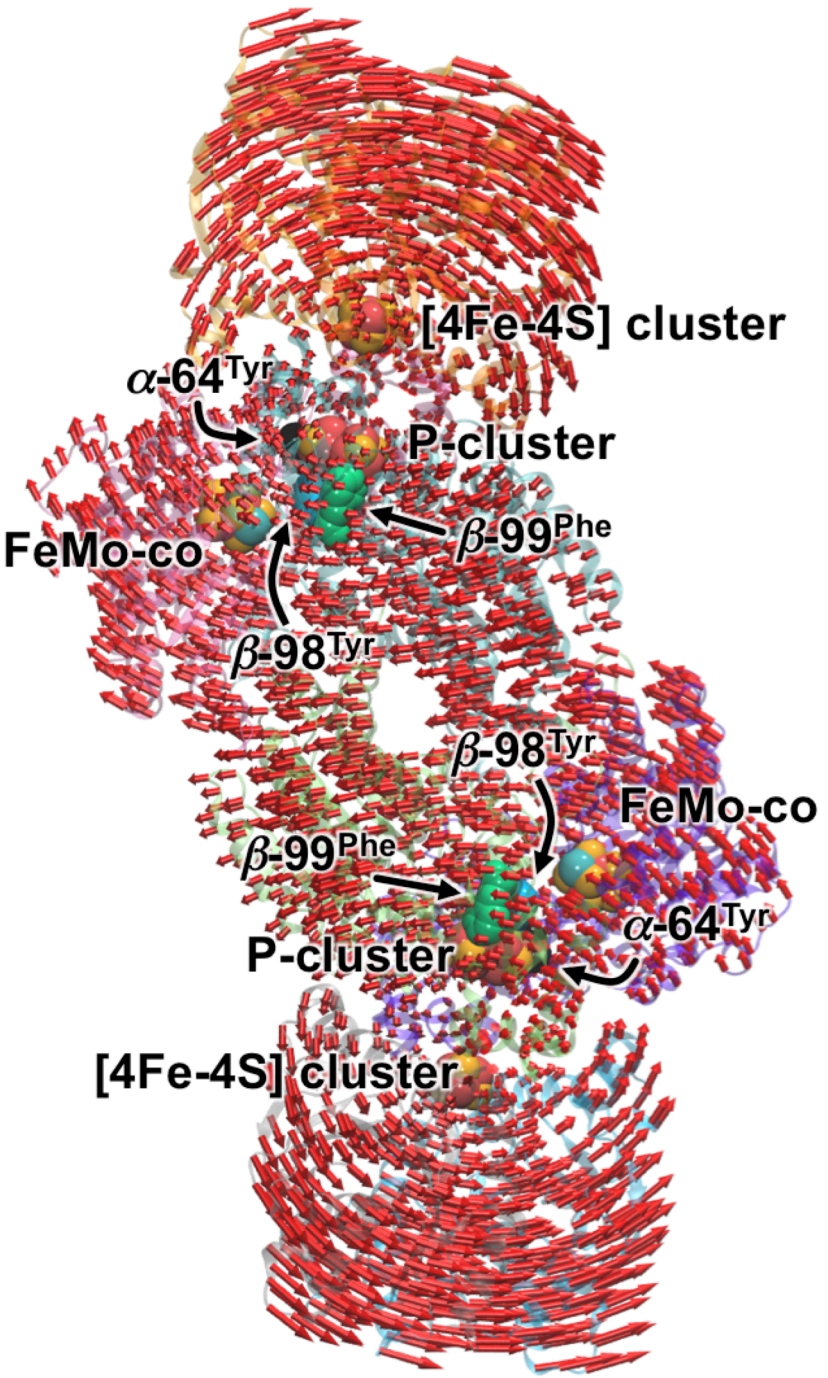


Figure 2.6. Collective motion corresponding to the rocking of the Fe protein on the MoFe protein surface. The length of the arrows is proportional to the displacement of the amino acid residues. The locations of the metal clusters and α-64^{Tyr}, ß-98^{Tyr}, and ß-99^{Phe} residues are shown.

which may provide the key to understanding the unique role of the Fe protein in regulating activity within the MoFe protein necessary for electron transfer and substrate reduction. The predicted motions within the MoFe protein are especially interesting because of the lack of any observed changes in different X-ray structures solved to date.[38]

Conclusion

Nitrogenase is a dynamic protein, with protein conformational changes playing key roles at various steps in the catalytic cycle.[39-41] The absolute need for the Fe protein and ATP binding to the MoFe protein to support N_2 reduction suggests that the protein-protein association communicates conformational changes within the MoFe protein essential to some aspects of catalysis, perhaps intramolecular electron transfer (i.e. initiation of deficit spending electron transfer) and/or substrate binding and reduction. The results add to the earlier finding that substitution of amino acids buried deep within the MoFe protein located between the P-cluster and FeMo-co can create a MoFe protein that is able to reduce a number of substrates without the Fe protein and ATP. The structure of the ß-$98^{Tyr\rightarrow His}$ reveals no global structural differences compared to the wild-type structure, with small changes localized near the amino acid substitution and homocitrate coordinated bound water. The structure reveals that subtle differences in structure couple with chemical difference in the amino acid side chains of tyrosine and histidine to alter the reactivity of the MoFe protein, suggesting that equally subtle changes might be sufficient when the Fe protein binds. Finally, computational normal mode analysis

reveals that the Fe protein and this region of the MoFe protein are connected in terms of molecular motion, suggesting a mechanism for how the Fe protein might communicate into the MoFe protein to affect activity.

CHAPTER THREE

THREE STRUCTURAL STATES OF THE NITROGENASE P-CLUSTER REVEALED IN MOFE PROTEIN STRUCTURES AT POISED POTENTIALS

Contribution of Authors and Co-Authors

Manuscript in Chapter 3

Author: Stephen M. Keable

Contributions: Purification, crystallization, electrochemical poising, structure determination

Co-Author: Andrew J. Rasmussen

Contributions: Electrochemical poising, electrochemical specialist

Co-Author: Karamatullah Danyal

Contributions: Electrochemical poising, electrochemical specialist

Co-Author: Brian J. Eilers

Contributions: Structure determination

Co-Author: Gregory A. Prussia

Contributions: Electrochemical poising

Co-Author: Axl X. LeVan

Contributions: Structure determination

Co-Author: Lance C. Seefeldt

Contributions: Corresponding author

Co-Author: John W. Peters

Contributions: Corresponding author

Manuscript Information Page

Stephen M. Keable, Andrew J. Rasmussen, Karamatullah Danyal, Brian J. Eilers, Gregory A. Prussia, Axl X. LeVan, Lance C. Seefeldt, John W. Peters
Biochemistry
Status of Manuscript:
_X__ Prepared for submission to a peer-reviewed journal
_ __ Officially submitted to a peer-review journal
____ Accepted by a peer-reviewed journal
_ _ Published in a peer-reviewed journal

Published by the American Chemical Society

CHAPTER 3

THREE STRUCTURAL STATES OF THE NITROGENASE P-CLUSTER REVEALED IN MOFE PROTEIN STRUCTURES AT POISED POTENTIALS

Abstract

The nitrogenase MoFe protein P-cluster functions in catalysis as an intermediate electron carrier between the external electron donor, the nitrogenase Fe protein, and the iron molybdenum cofactor (FeMoco) substrate reduction site within the MoFe protein. In this work the MoFe protein was poised at defined potentials with redox mediators in an electrochemical cell and three distinct structural states of the P-cluster ($P^{2+}/P^{1+}/P^{N}$) were characterized by x-ray crystallography. It is revealed here that that the three oxidation states differ in direct coordination. These results provide a complete picture of the redox dependent ligand rearrangements of three P-cluster redox states.

Chapter Introduction

Nitrogenase is the enzyme responsible for the multiple electron reduction of atmospheric dinitrogen (N_2) to ammonia (NH_3) in biological systems.[2] This complex oxygen sensitive metalloprotein orchestrates a series of ATP-dependent single electron transfers from the donor Fe protein to the catalytically active MoFe protein.[42] During catalysis, the process of electron delivery to the active site involves two types of electron transfer events: one event being the intermolecular electron transfer between the [4Fe-4S] cluster of the Fe protein and the [8Fe-7S] P-clusters of the MoFe protein, and the other being the

intramolecular electron transfer between the two P-clusters and two [7Fe-9S-C-Mo-homocitrate] FeMo-cofactor active sites within the MoFe protein.[12, 43] Recent work has helped delineate the order of these electron transfer events with a proposed "deficit-spending" model.[7] This model postulates that the interaction of the Fe protein and the MoFe protein elicit conformational changes that facilitate an initial “slow” and conformationally gated electron transfer step event between the P-cluster and the FeMo-cofactor.[7, 38] This event leaves the P-cluster with a "deficit" of one electron, (P^{1+}) relative to the all-ferrous resting (P^{N}) state. This deficit is then repaid by a second "fast step" intermolecular electron transfer event from the reduced $[4Fe\text{-}4S]^{1+}$ cluster in the Fe protein to the P^{1+}-cluster, restoring the P^{N} state.[7] This fast step is a direct electron transfer step and takes place at rates greater than 1700 s^{-1}, which could explain why the P^{1+} state is difficult to observe during turnover.[44] Thus the deficit spending model postulates that major conformational changes occur during catalysis, but the conformational changes that regulate the gated unidirectional electron flow are likely short-lived. The mechanistically relevant P^{1+} state has been observed spectroscopically in native and variant MoFe proteins.[45, 46] However, this state was only achievable using electrochemical mediators. Previous structural work has revealed two distinct conformations of the P-cluster that have been assigned to the P^{N} resting state and the P^{2+} oxidized state (Figure 3.1).[5, 11] The structures differ in the ligation of P-cluster Fe ions such that the P^{2+} oxidized state possesses two non-cysteinyl protein ligands where serine side chain oxygen and a peptide backbone amde nitrogen replace two of the ligands of

the hexacoordinated central sulfide present in the P^N state (Fig 1A). The P^{2+} conformation is typically seen in native MoFe protein structures due to the gradual

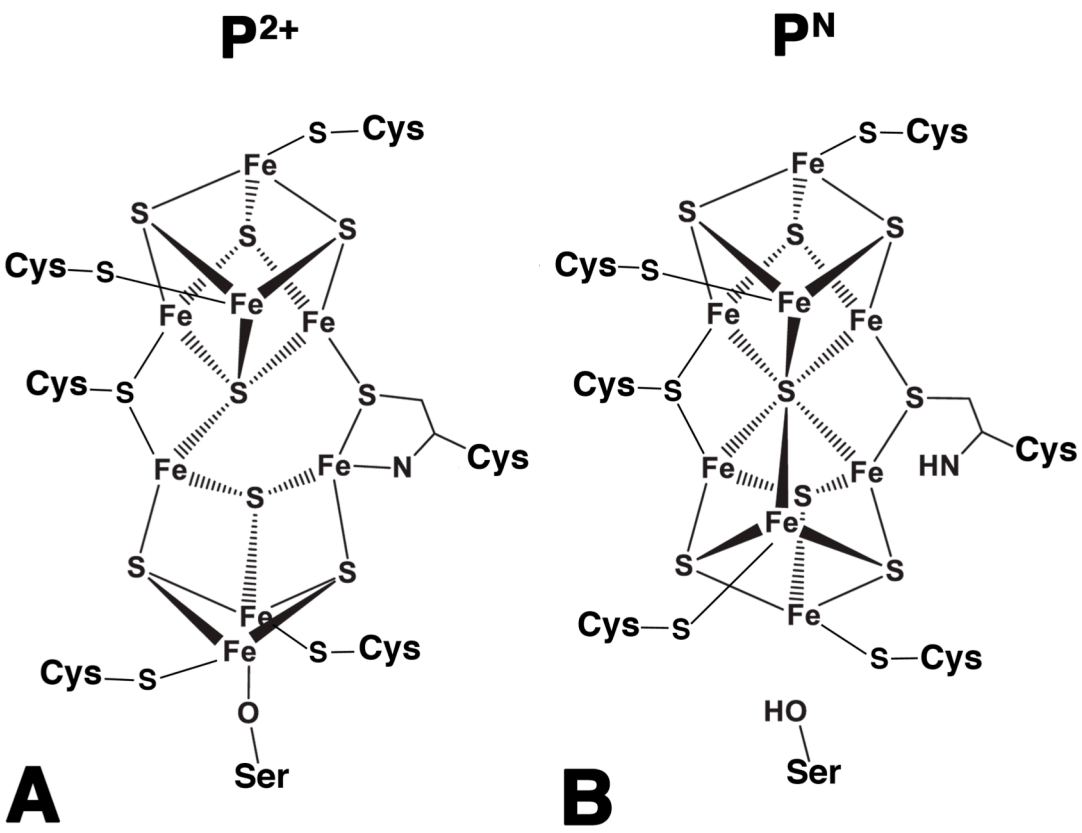


Figure 3.1. Presumed structural representations of the P^{2+} (A) and P^N (B) redox states of the P cluster, highlighting differences in ligation. (1 column)

oxidation of reductants present in the precipitant solution during crystallization. The P^N state was generated by reducing MoFe protein crystals with excess sodium dithionite just prior to flash cooling in a similar manner to the aforementioned spectroscopic studies.[11, 47]

The role of alternative electron transfer mechanisms involving direct oscillations between the P^N and P^{2+} states has been previously investigated;[48] however various lines of evidence indicate that only single electron transfer events occur between the reduced P^N state P-cluster and the active site, suggesting the P^{1+}/P^N couple is the predominant oscillation of the P-cluster under turnover conditions.[1] The P^N and P^{2+} states are structurally accessible and provide fascinating insights implicating redox dependent structural changes in the nitrogenase mechanism, but completing the understanding of the mechanistic cycle requires knowledge of the structure of the catalytically relevant P^{1+} state. To elucidate the structure of the P^{1+} state, structures of the nitrogenase MoFe protein were solved for crystals poised at defined oxidation-reduction potentials with redox mediator solutions in an electrochemical cell.

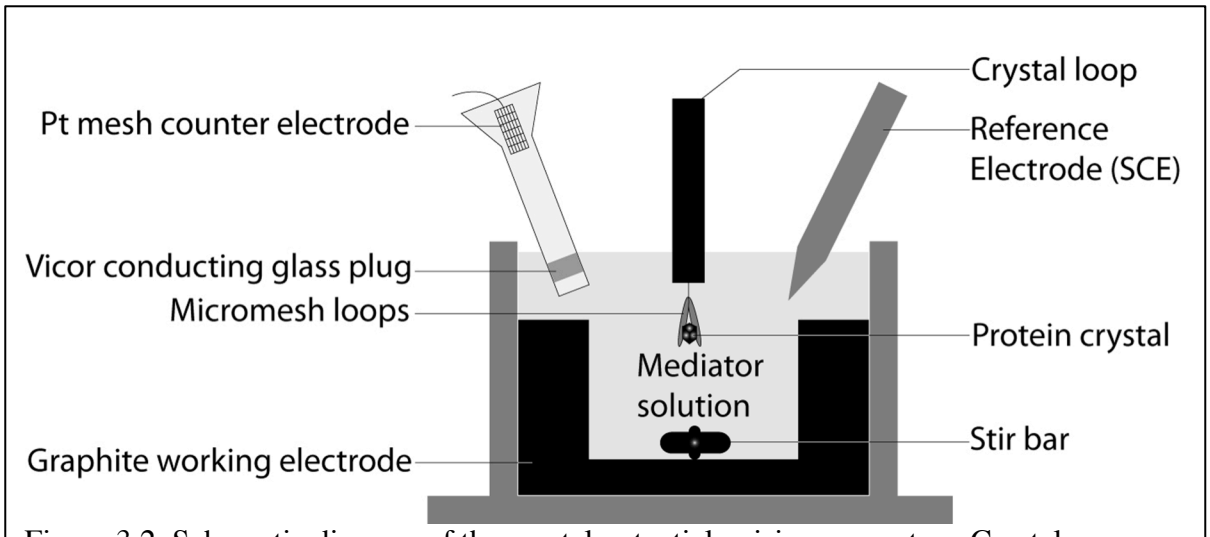


Figure 3.2. Schematic diagram of the crystal potential poising apparatus. Crystals were submerged in a stirred soution held at constant potential for 1 hour prior to flash cooling in liquid nitrogen to poise them in distinct structural states.

Crystals were poised at different potentials in an electrochemical cell containing mother liquor supplemented with redox active dyes (Figure 3.2). Constant stirring maintained a homogenous charge throughouthe solution, and a "sandwich-loop" crystal mounting technique was developed to prevent the crystals from washing off the loop during electrochemical poising.

Materials and Methods

All Chemicals were purchased from Sigma-Aldrich (St. Louis, MO) or Fischer Scientific (Fair Lawn, NJ) and were used without further purification. Wild type MoFe protein from *Azotobacter vinelandii* was purified under strict anaerobic conditions with slight modifications to previously described protocols.[49] All proteins were obtained at greater than 95% purity as judged by SDS-PAGE analysis using Coomassie blue staining and demonstrated maximal specific activity (greater than 2,000 nmol H_2/min/mg MoFe protein). Handling of proteins was done in septum-sealed serum vials under an argon atmosphere. All transfer of gases and liquids were done using gastight syringes. Protein crystals were grown by capillary batch diffusion in a 100% N_2 atmosphere MBraun glove box with previously reported precipitant solutions.[31]

Poising Crystals with Redox Mediators

Crystals were harvested anaerobically under an argon stream and immobilized on pins using a novel "sandwich" loop designed to prevent the crystals from washing away

during electrochemical studies. Two micromesh loops (MiTiGen LLC, Ithaca, NY) were affixed on top of each other to the same pin, and a small piece of monofilament was placed in between to separate them. Crystals were positioned between the loops, and the monofilament was then removed to apply tension from the loops to secure the crystals. The immobilized crystals were immediately submerged in an electrode solution mimicking the precipitant solution composed of 18% PEG 4000, 50 mM Tris-HCl buffer pH 8.0, 15% glycerol, 100 mM sodium chloride, and 1 mM of a redox mediator. The mediators used were methylene blue, flavin mononucleotide, and methyl viologen with midpoint potentials (E_m) of +11mV, -238 mV, and -488 mV respectively vs. standard hydrogen electrode.[50] The mediator solutions were degassed and placed in an electrochemical cell with a built in graphite working electrode (2.8 cm^2 surface area), a mesh platinum counter electrode separated by a vicor conducting glass plug, and a saturated calomel electrode (SCE) reference electrode (Figure 3.2). The solutions were kept under a constant stream of humidified argon to maintain anaerobicity without modifying solution volume. The electrode solutions were poised at +11mV, -238 mV, and -488 mV vs. normal hydrogen electrode (NHE) for methylene blue, flavin mononucleotide, and methyl viologen, respectively. An OMNI-101 microprocessor controlled potentiostat (Cypress Systems, Lawrence, Kansas) was used to control potential and constant stirring was used to achieve a uniform solution. The sub-merged sandwich looped crystals were allowed to soak for 1 hour and were immediately flash cooled in liquid nitrogen to preserve the poised states. Data were collected at SSRL BL12-2 for native *A. vinelandii* MoFe protein poised at three defined potentials. Due to

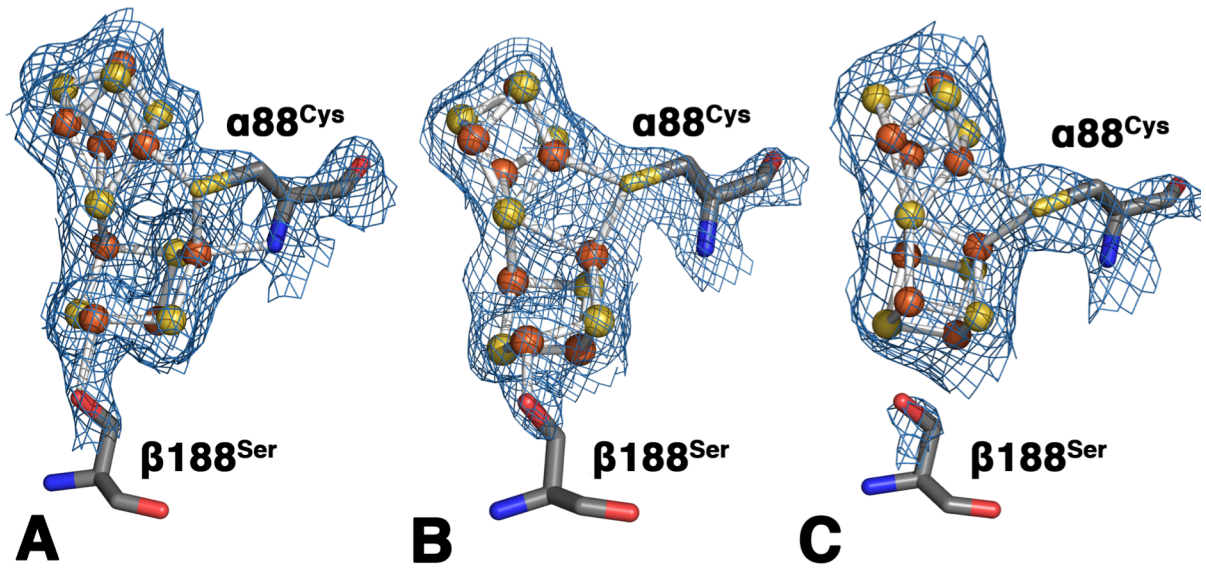


Figure 3.3. Models of the P^{2+} **(A)**, P^{1+} **(B)** and P^{N} **(C)** structural states of the P-cluster superimposed with $2F_o$-F_c electron density of MoFe protein crystals poised with redox mediators held at a defined potentials. Density contoured to 2σ.

the increased susceptibility to radiation damage caused by the mediator solution treatment, partial data sets were collected to observe unaltered structural features, and a decrease in data quality was observed relative to untreated crystals. Processed data completeness (~60%) and resolution (~2.2 Å) was similar for all poised data sets (SI Tables S3.1-.3.3).[33] The unit cell parameters were isomorphous with the previously determined MoFe protein structure and the structure of the P^{2+} state in the PDB (2MIN) was refined against each data set.[51] Although the data overall for the three states is not of high quality, the previously characterized P^{N} and P^{2+} states, as well as the newly characterized P^{1+} state could be clearly visualized and distinguished in electron density (Figure 3.3).

In addition, the data were of sufficient quality to obtain interpretable difference electron density maps that support the individual assignments of the three structural states.

Results and Discussion

Crystals treated with flavin mononucleotide held at -238 mV for one hour revealed a novel intermediate structure distinct from the P^N and P^{2+} structures in ligation assigned as

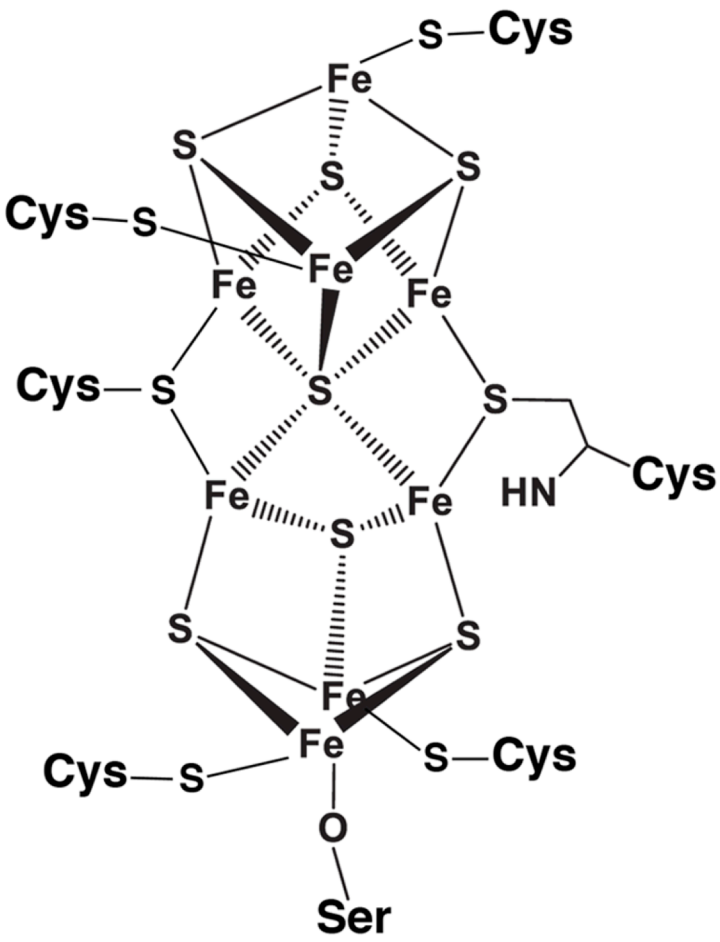


Figure 3.4. Structural representation of the P^{1+} redox state of the nitrogenase P-cluster deduced from the present studies.

the P^{1+} (Figure 3.4). Electron density maps were of sufficient quality to clearly distinguish the P^{1+} structural state from the previously reported P-cluster structures (Figure 3.3).

Interestingly, the P^{1+} state was only observed on one αβ dimer of the 2-fold symmetric $\alpha_2\beta_2$ heterotetrameric MoFe protein. The P^{1+} state structure has a ligand arrangement intermediate between the P^N and P^{2+} states. The P^{1+} state possesses serine coordination to

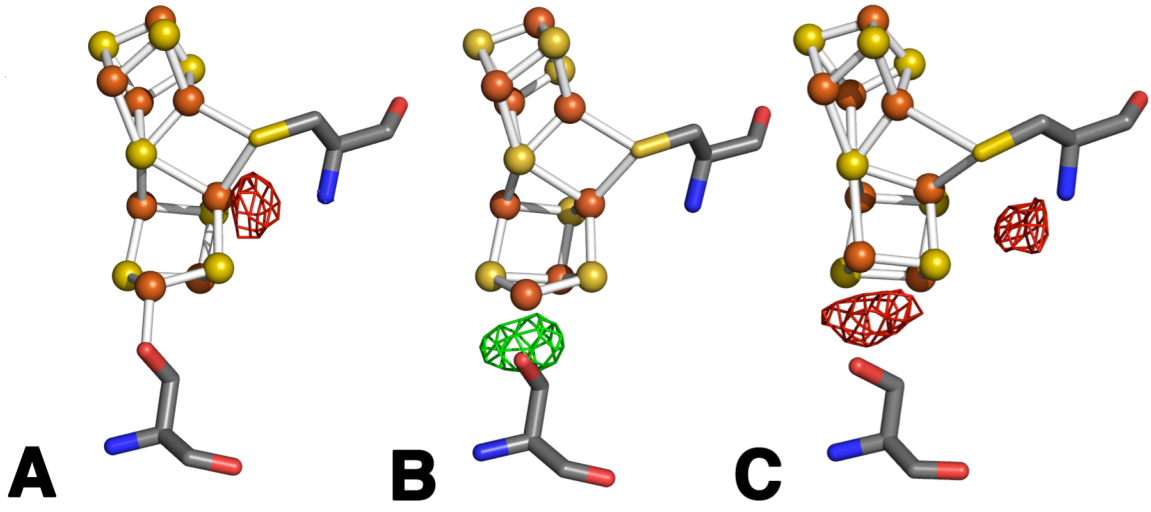


Figure 3.5. F_o-F_c difference electron density analysis of electrochemically poised P-cluster structures. The P^{1+} model is shown **(A)** with F_o-F_c (P^{1+}-P^{2+}) difference electron density contoured to 5σ. The P^{1+} model is shown **(B)** without a bond between $\beta188^{Ser}$ and the P-cluster, with F_o-F_c (P^{1+}-P^N) difference electron density contoured to 2σ (peak still clearly present at 3σ). The P^N model **(C)** with F_o-F_c (P^N-P^{2+}) difference electron density contoured to 3σ highlighitng the differecnces between the 2 electron reduced and oxidized poised structures.

Fe, but lacks the amide nitrogen ligation seen in the P^{2+} state. F_o-F_c difference density analysis experiments were carried out between the P^{1+} and P^N, P^{1+} and P^{2+}, and the P^N and P^{2+} structures to confirm the new structural state, and the states of the previously reported P-cluster structures (Figure 3.5).

The observation that the amide nitrogen ligand is exchanged by ligation to the central S prior to the serine oxygen coordination in the redox progression during reduction can be rationalized from the perspective of the Hard/Soft and Acid/Base (HSAB) Theory since nitrogen is a slightly harder and weaker ligand than oxygen and would weaken further upon reduction. Thus, the suite of P-cluster structures provides evidence to suggest that the first oxidizing equivalent changes the structure of the Fe atom near the Ser-β188, and may oxidize this Fe first. The second oxidizing equivalent would then oxidize the Fe atom near the Cys-α88. This newly visualized P^{1+} state is compatible with the proposed deficit spending mechanism and demonstrates a redox-mediated ligand exchange mechanism for possibly regulating electron flow for the P^{1+}/ P^N redox couple. Previous mutagenesis studies targeting the Ser-β188 P-cluster ligand have utilized the introduction of a stronger ligand, such as cysteine, or removal of coordination by glycine substitution to stabilize the P-cluster in the P^{1+} and P^N states by shifting the resting potential of the cluster -90 mV and +60 mV, respectively.[12, 52] Also of interest is these amino acid substitutions confer lower specific activities to the variants by disrupting a key exchangeable ligand.[7, 12] These observations add support to our P^{1+} assignment of this structure and the prominence of a ligand exchange mechanism in nitrogenase catalysis. Recently, we have shown that amino acid substitutions near the proximal side of the P-

cluster cubane relative to FeMo-co (Fe 1-4 based on the PDB numbering scheme), such as Tyr-His- β98, Phe-His-β99, and Tyr-His-α-64His, generate protein variants that are capable of being reduced by low reduction potential mediators which have Eu(II) ligated

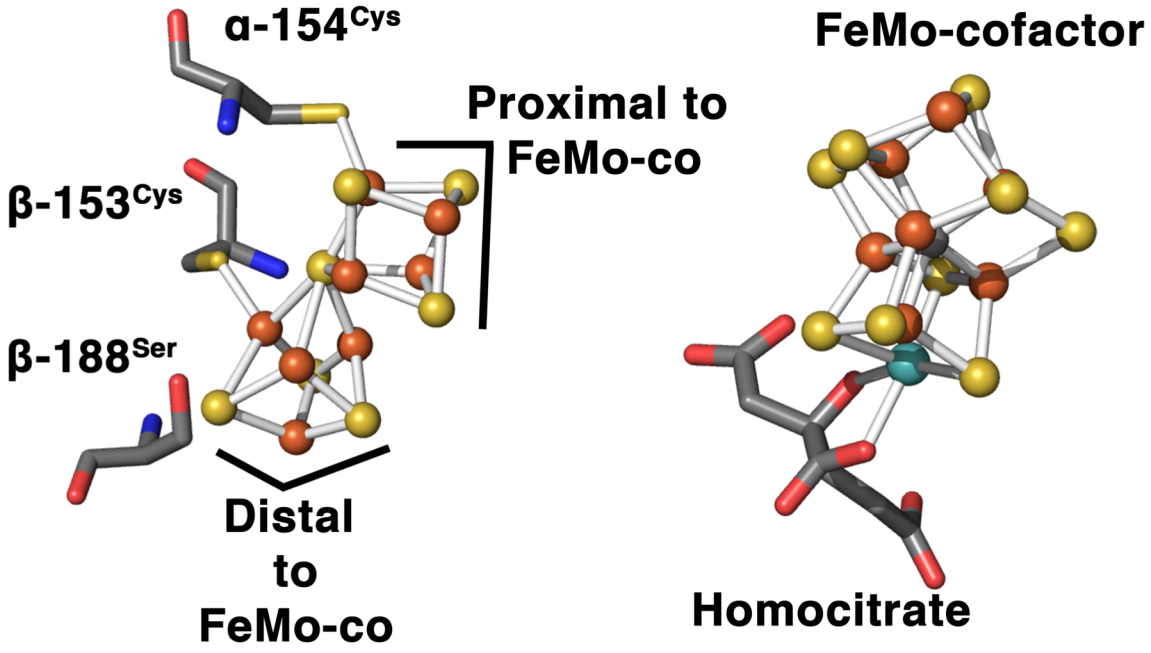


Figure 3.6. Ball and stick representations of the P-cluster and FeMo-cofactor, highlighting the orientation of the P-cluster cubanes with respect to the FeMo-cofactor.

to polyaminocarboxylate ligands, while substitutions near the Fe5-8 cubane (distal to side to FeMo-co) do not show this behavior.[26, 53] Analyzing this information in light of our current finding, we can assign directional character to the P-cluster. Here based on the substitution studies, the proximal side of the cubane relative to FeMo-co would be involved in the electron transfer between the P-cluster and FeMo-co during the slow step,

while the distal cubane undergoes structural conformational changes in order to accommodate the loss of an electron from the P-cluster (Figure 3.6).

We have also recently shown that electron transfer between the Fe protein and the MoFe protein precedes ATP hydrolysis. Conformational changes within the P-cluster of the MoFe protein during the deficit spending events could potentially serve as triggers for the initiation of the ATP hydrolysis step within the Fe protein. This would result in the Fe protein cycle of electron transfer being a conformationally controlled series of events. Furthermore, it has been previously suggested that the Fe protein – MoFe protein interaction could cause the Ser-β188 to transiently coordinate to the P-cluster, creating an activated P-cluster state (designated P^{N*}) with a lowering of the potential to facilitate electron transfer between the P-cluster and FeMo-cofactor.[7]

Conclusion

The one electron ligand exchange also raises the possibility of the P-cluster's involvement in the proposed proton coupled electron transfer (PCET) mechanism in nitrogenase. The Ser-β188 ligand has been suggested to be protonated when not coordinated to the P cluster, and sequential hydride formation has been postulated as part of the catalytic cycle,[18] therefore the single redox P^{1+}/P^{N} couple fits well into the most recent proposed deficit spending mechanism. Additionally, previous spectroscopic studies have also shown residues around the distal side of the P-cluster cubane (relative to FeMo-co) to be involved in PCET.[52] Although this unique iron-sulfur cluster has been

shown to undergo unprecedented redox-mediated structural changes, a complete understanding of the unidirectional PCET is difficult without more information regarding the complex and dynamic global conformational changes that occur when the Fe protein interacts with the MoFe protein. Current structural techniques have failed to provide details of these transient global conformational changes. By utilizing a new redox crystallography approach, we are now able to populate some of these difficult to obtain transient states and piece together the details of one of nature's most enigmatic catalytic cycles. The work presented here also has relevance to probing electron flow and redox mediated structural changes in numerous metalloprotein systems, providing possible insights into biological electron transfer.

CHAPTER FOUR

ACETYLENE INTERACTION WITH THE NITROGENASE FEMO-COFACTOR INVESTIGATED BY STRUCTURAL AND COMPUTATIONAL ANALYSIS

Contribution of Authors and Co-Authors

Manuscript in Chapter 4

Author: Stephen M. Keable

Contributions: Purification, crystallization, structure determination

Co-Author: Jacopo Vertemara

Contributions: Computational analysis

Co-Author: Karamatullah Danyal

Contributions: Growth and purification

Co-Author: Andrew J. Rasmussen

Contributions: Growth and purification

Co-Author: Brian J. Eilers

Contributions: Structure determination

Co-Author: Oleg A. Zadvornyy

Contributions: Structure determination

Co-Author: Luca De Gioia

Contributions: Computational analysis

Co-Author: Giuseppe Zampella

Contributions: Computational analysis

Co-Author: Lance C. Seefeldt

Contributions: Corresponding author

Co-Author: John W. Peters

Contributions: Corresponding author

Manuscript Information Page

Stephen M. Keable, Jacopo Vertemara, Karamatullah Danyal, Andrew J. Rasmussen, Brian J. Eilers, Oleg A. Zadvornyy, Luca De Gioia, Giuseppe Zampella, Lance C. Seefeldt, John W. Peters
Biochemistry
Status of Manuscript:
_X__ Prepared for submission to a peer-reviewed journal
_ __ Officially submitted to a peer-review journal
____ Accepted by a peer-reviewed journal
_ _ Published in a peer-reviewed journal

Published by the American Chemical Society

CHAPTER 4

ACETYLENE INTERACTION WITH THE NITROGENASE FEMO-COFACTOR INVESTIGATED BY STRUCTURAL AND COMPUTATIONAL ANALYSIS

Abstract

The nitrogenase active site FeMo-cofactor is an unprecedented [7Fe-9S-C-Mo-homocitrate] metallo-cluster with multiple sites that have been proposed to be the location of substrate reduction. The ambiguity of the nitrogenase substrate reduction site(s) has long been a contentious issue. Reported here is a 1.70 Å crystal structure of a nitrogenase MoFe protein variant with the mechanistically relevant substrate acetylene in close proximity to the Fe6 position of FeMo-co. Computational analysis of this structure indicates favorable acetylene binding at this position versus wild type. Acetylene is considered a model substrate analogue to atmospheric nitrogen in this system, and characterization of this ligand-binding site provides crucial insight into the mechanism of dinitrogen reduction.

Chapter Introduction

The molybdenum dependent nitrogenase is an integral component of the global nitrogen cycle, catalyzing the reduction of atmospheric nitrogen to ammonia. The nitrogenase system contains two metalloprotein components deemed the Fe protein and the MoFe protein, which must undergo multiple cycles of MgATP dependent association and

dissociation events to deliver electrons from the Fe protein to the substrate binding and catalytic sites in the MoFe protein.[1, 43] The MoFe protein is an $\alpha_2\beta_2$ heterotetramer that contains 2 [8Fe-7S] P-clusters and 2 active site [7Fe-9S-C-Mo-homocitrate] FeMo-cofactors.[1, 5] The Fe protein is a heterodimer bridged by a [4Fe-4S] cubane and has two sites for MgATP binding and hydrolysis, one in each subunit.[4] Due to the complex interplay between the component proteins, characterization of high-turnover substrates in crystals structures of the native protein has been unattainable. To overcome this barrier, utilization of site a directed variant with unique biochemical properties has allowed for the structural assignment of the substrate analog acetylene in close proximity to the FeMo-cofactor. Previous EPR spectroscopy studies have demonstrated the intrinsic ability of several site directed variants to allow substrates such as actylene to persist at the active site of resting state MoFe protein.[13] To capitalize on this finding, protein crystallization trials of these variants were initiated in the presence of acetylene to capture substrate interaction with the FeMo-cofactor for structural characterization. Reported here is the crystal structure and computational analysis of the nitrogenase MoFe protein variant α-$96^{Arg\rightarrow Gln}$, with the substrate acetylene in close proximity to Fe6 of the FeMo-cofactor. Computational analysis suggests that access of acetylene to the FeMo-cofactor environment at this position is energetically favorable (Figure 4.1). These results are consistent with previously reported genetic, spectroscopic and computational findings and establish a mechanistically relevant site for substrate reduction.[54-56]

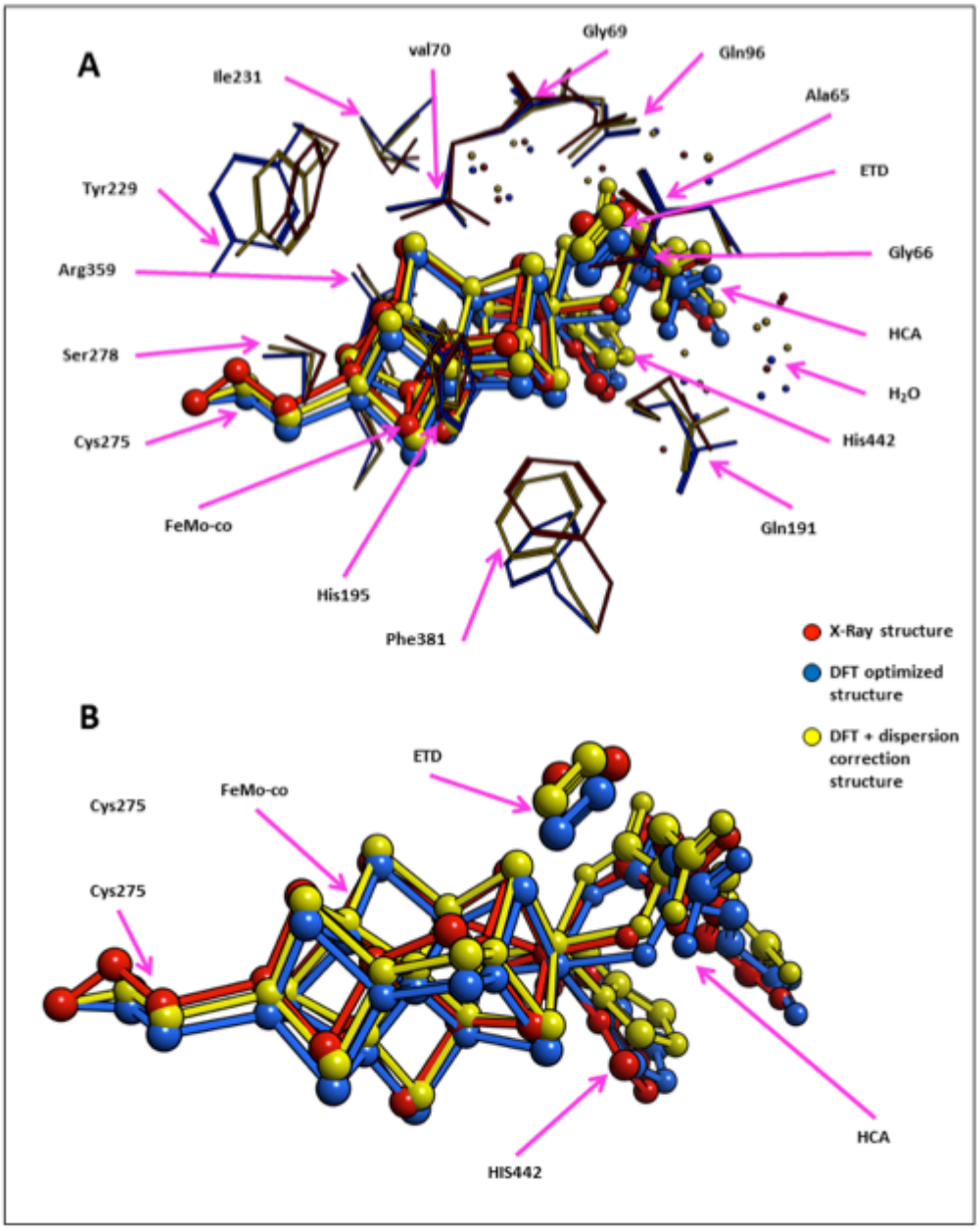


Figure 4.1. (A) Superposition of both FeMo-co and surrounding first-sphere residues of X-Ray structure R96Q (in red), DFT optimized structure (in blue) and DFT optimized structure including dispersion contributions (in yellow). (B) Blowup of FeMo-co and acetylene in the three structures.

Materials and Methods

Nitrogenase MoFe protein was expressed in *Azotobacter vinelandii* strain DJ1264 (α-$96^{Arg \rightarrow Gln}$) and grown as previously described.[27] The variant MoFe protein was purified to >95% purity, confirmed by SDS gel electrophoresis, using slight modifications to previously reported procedures.[27] All protein manipulations were carried out in ealed serum vials under argon atmosphere or in MBraun anaerobic glove box under 100%. MoFe protein crystals were grown by capillary batch diffusion in a solution containing 30% (w/v) polyethylene glycol (PEG) 4000, 0.1 M Tris (pH 8.0), 0.17 M Na_2MoO_4, and 0.001 M sodium dithionite. Prior to crystallization, both the protein solution and the precipitant solution were saturated with acetylene gas by sparging for 5 minutes. Crystals of dark brown color with dimensions of ~ 200 μm X 200 μm X 200 μm were observed within 4-6 weeks. Crystals were treated with acetylene saturated mother liquor supplemented with 15% (v/v) glycerol prior to flash cooling in liquid nitrogen. Data collection was carried out under a continuous nitrogen stream (~100 K) on beam line 12-2 at the Stanford Synchrotron Radiation Laboratory (Table S4.1).

DFT calculations were been carried out using the TURBOMOLE 7.0.1 suite of programs.[57] Mixed basis set has been used: a split valence triple-ζ basis set with polarization (TZVP)[58] for FeMo-cofactor (E0, S=3/2 state), His442, Cys275, homocitrate (that are all covalently bound to Fe-S cluster) and acetylene; a triple-ζ basis set with double polarization and diffuse functions (def2-TZVPD)[59] for Mo atom; a single-ζ basis set (SVP)[55] for amino acid side chain atoms. The pure exchange-correlation functional BLYP[60] has been adopted in that it was already validated in literature for QM nitrogenase

investigations.[61] Dispersion correction to SCF energy has been performed using the approach proposed by Grimme for DFT.[62] Polarization effects of both solvent and active site amino acid side chains has been evaluated according to the conductor-like screening model (COSMO, ε= 40).[63-65] Spin configuration of iron atoms within FeMo-co has been verified to correspond to that generally accepted for E0 (i.e., all iron ions are reciprocally antiferromagnetically coupled).

The DFT procedure is briefly described as follows:

1) DFT geometry optimization of FeMo-cofactor/acetylene complex and relevant (15) amino-acid residues (see Figure 1 for the full list included in simulations) starting from X-ray structure R96Q. Aminoacid residues have been truncated at Cα so all the atoms of sidechains are present in the model. To our knowledge, this is the largest size setup related to QM-only (i.e., no atom in the model is treated by semi-empiric and/or classic Force Field based methods) investigations on nitrogenase. The original purpose of maintaining zwitterionic forms of aminoacids has been subsequently dropped as it yields unrealistic bond dissociations during simulations. Twelve molecules of water of crystallization has been included in calculation so as to simulate explicitly the presence of solvent. Both possible protonation states of homocitrate covalently bound to Fe-S cluster have been considered

2) A first level refinement has been performed including effects of dispersive forces in the model. This has been necessary to treat attractive component of the

potential energy curve associated with London-type interactions, that is normally missing in standard density functionals, due to the fact that the stabilizing effect of dispersion occurs from medium- to long-range distance (where electron densities based on truncated basis sets do not overlap)

3) A second level refinement has required single-point corrections including effect of polarizing environment of the active site pocket (ε=40, as often used in literature[8] for a large number of protein active sites, see also Computational details)

4) A third level refinement has been applied evaluating (and correcting by means of Counterpoise method) the so-called BSSE (Bias Se Superposition Error), a computational issue originating in QM calcculations (with finite size basis sets, namely all those employed) when evaluating energetics of bi-molecular complex formation (starting from separate molecules)

$\Delta E_{binding}$ was calculated using this formula:

$\Delta E\_\text{binding} = E_{AB} - (E_A + E_B)$

Where E_{AB}, E_A, and E_B is the energy of FeMo-co/acetylene complex, FeMo-cofactor (all atoms included in "AB" but those of acetylene) and acetylene, respectively.

Summarized in Table 4.1. are the energetics of binding at the various levels of modelling used in the study.

Table 4.1.	$\Delta E_{binding}$ (kcal/mol)
DFT/BLYP	+2,1
DFT/BLYP/dispersion	-17.3
DFT/BLYP/dispersion/ COSMO (ε=40)	13.0
DFT/BLYP/dispersion/ COSMO (ε=40)/BSSE (BSSE_avg)	-4.0(-8.5)

Computational Analysis of Acetylene Bound MoFe

All interatomic distances (Fe-S, Fe-C , Mo-X bonds) of FeMo-co in the X-ray structure are quite well reproduced by DFT (on average, differing less than 0.06 Å). Analysis of the DFT optimized structure versus the X-ray structure reveal slight shifts in atom positions (Figure 4.2.). Figures 1 and 2 illustrate a picture in which acetylene undergoes a sort of partial rotation about one of its C2 axis, which causes it to come closer to FeMo-co than it is located in the crystal structure. The extent of rearrangement looks, however, compatible with both resolution of the experimental structure and also with the dispersive nature of the weak interaction FeMo-co-acetylene. DFT results are thus confirming also from a structural standpoint, the assignment of the acetylene molecule in close proximity of FeMo-co of α-$96^{Arg\rightarrow Gln}$ nitrogenase MoFe protein variant, as observed by X-ray

crystallography. A summary of the interatomic distances for the crystal structure and two DFT structures is illustrated in Table SI 4.2.

All data reported in table and also Figures 4.1 and 4.2 are based on simulations featuring protonated homocitrate (the most likely, in the light of the highly negative charge of

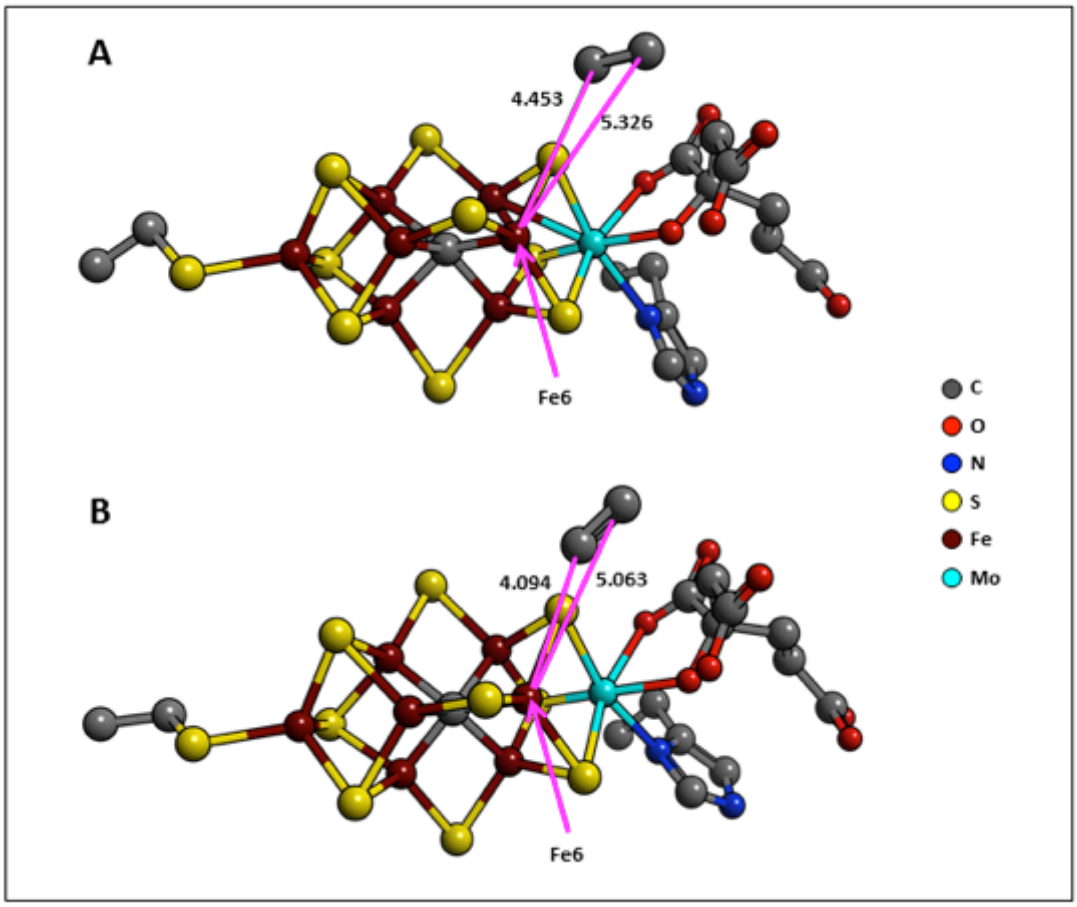


Figure 4.2. Fe6-C_2H_2 distances taken as reference to evaluate the acetylene shift from X-ray crystal structure position (A) to DFT optimized structure (B).

FeMo-co). Simulations carried out by using deprotonated homocitrate has revealed a very disfavoured docking process of acetylene into nitrogenase active site pocket and have therefore been dropped in subsequent analysis. The effect of neutralizing the -4

charge of the computational model set up in the present study has been investigated by placing 4 K^+ ions at the exact position where X-ray structure detect the centroid of the ammonium plus three guanidinium groups belonging to Lys 301 and Arg 25, 200 and 436, respectively (Figures 4.3 & 4.4., SI Table 4.3). The simplest level of theory used (DFT/ BLYP) shows interesting results, since the slight endergonic binding has to be considered in the light of the precision limit of DFT. Therefore +2.1 kcal/mol may be actually indicative of a "near-to-equilibrium" situation (i.e., $\Delta E_{binding} \approx 0$). When switching to more sophisticated treatments of the system nature under investigation (thus considering dispersion interaction attractive holes and refining polarization effects by solvent medium), the predicted binding energy is clearly indicative of exergonic process. The quite large absolute value of the binding energy (though COSMO screening model partially mitigates this effect) seems to be overestimating an interaction that is expected to be weak (due to the induced dipole moments in acetylene). However, when considering the BSSE effect (both entirely and and its half also, as reported by some authors[10]) the issue is actually fixed. At this point the only contribution left to include would be the entropy cost paid by acetylene to access the FeMo-co site. Yet, frequency calculations on such a large-sized system have proved to be prohibitive. A qualitative considerations can be made, however, regard to this point: the positive contribution arising from that (i.e., entropy loss) is expected to be paid by substrate already along/through the diffusion channel leading from outside the protein directly to its active site. Thus, when acetylene gets out of the channel to move in proximity of FeMo-co

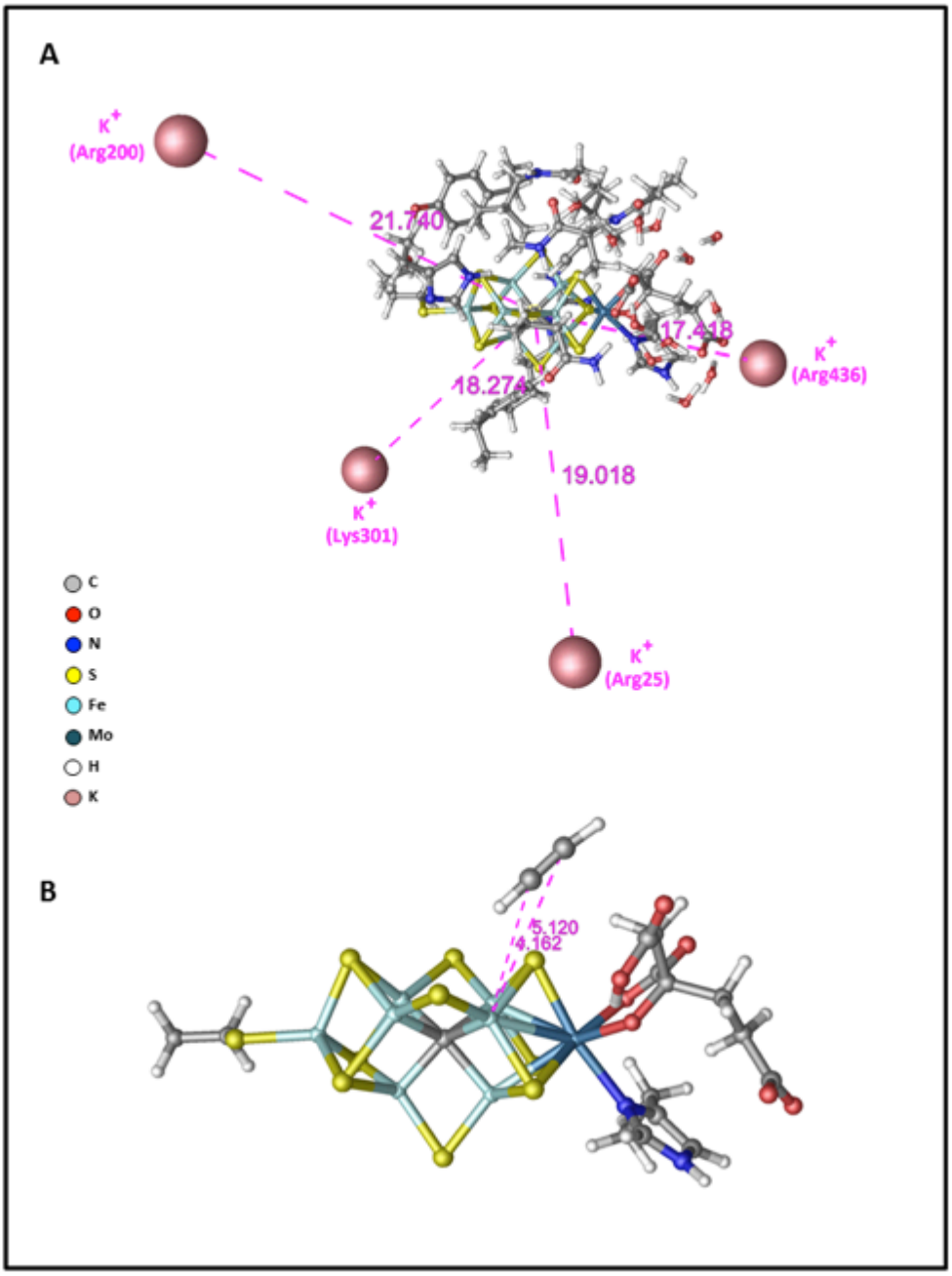


Figure 4.3. Neutrally charged model with four K^+ ions (aa residues modelled by K^+ are shown; the distance between each potassium and interstitial C is also displayed). Panel B shows distances (in Å) between Fe6 and acetylene after the DFT converged simulation.

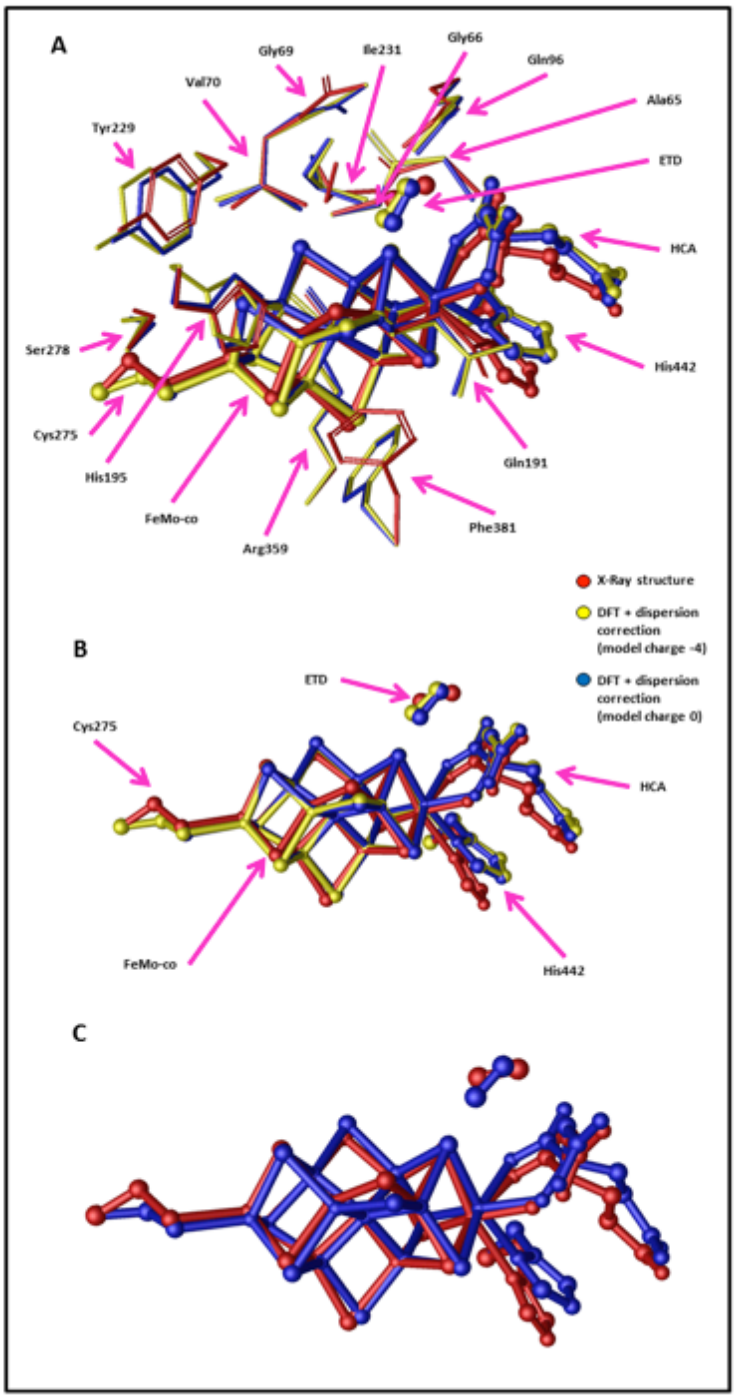


Figure 4.4. Picture shows X-ray structure R96Q in red, model with total charge -4 in yellow and model with neutral charge in blue (charge is neutralized by four K^+ ions located at the centroid of positively charged residues). In this sketch hydrogen atoms have been omitted as well as K^+. (Panel A) Overlap of FeMo-cofactor and first-shell residues of X-ray structure R96Q and the two DFT optimized models (all including dispersion energy effects). (Panel B) Blow-up of FeMo-cofactor and acetylene in the three structures (XRD/DFT(charge=-4)/DFT(charge=0). (Panel C) Blow-up of FeMo-cofactor and acetylene in case of X-ray structure and neutrally charged DFT model.

(namely where it has been detectd by crystallographic analysis and DFT), it has practically lost the most of its entropy content. The present results are in line with a thermodynamically facile accommodation of acetylene close to FeMo-co of α-96$^{Arg\rightarrow Gln}$ MoFe active site.

Computational studied were also carried out on the wild type nitrogenase active site pocket to determine if acetylene biding is more or less favorable compared to the α-96$^{Arg\rightarrow Gln}$ MoFe variant. The computational model of wild type nitrogenase active site has been obtained starting from X-ray structure 1M1N (PDB code); the amino acids residues taken into explicit account are exactly the same used for the α-96$^{Arg\rightarrow Gln}$ MoFe variant structure, with the (trivial) sole exception of Arg96. Two sets of calculations have been performed:

- The first one with total charge equal to -3 (arising from FeMo-co+aa present in the DFT model of WT system)
- A second one with total charge 0 (-3 charge has been neutralized by three K^+, placed according to criteria previously described).

The same corrections to pure DFT energy that was used for the α-96$^{Arg\rightarrow Gln}$ MoFe nitrogenase protein variant study have been applied also here (dispersion correction, implicit solvation model and counterpoise correction).

Different rotamers of Arg96 have been energetically sampled. Results herein reported deals with the structural isomer featuring the Arg orientation/disposition more similar to that observed in 1M1N crystal structure. Table SI 4. summarizes the energetics of binding at the various levels of modeling used in the study.

Results are in line with experiments, the acetylene binding energy to the active site pocket results more favourable for the mutant system than for the wild type enzyme for each set of calculations. Also, the quantitative difference (α-96$^{Arg\rightarrow Gln}$ MoFe vs WT) in terms of binding energy is compatible with non-polar nature of the substrate

An explanation can be found in the different chemico-physical properties (electrostatic features) of the region available for acetylene binding in proximity of FeMo-co: in presence of the substitution Arg→Gln the pocket environment (Figure 4.5) becomes

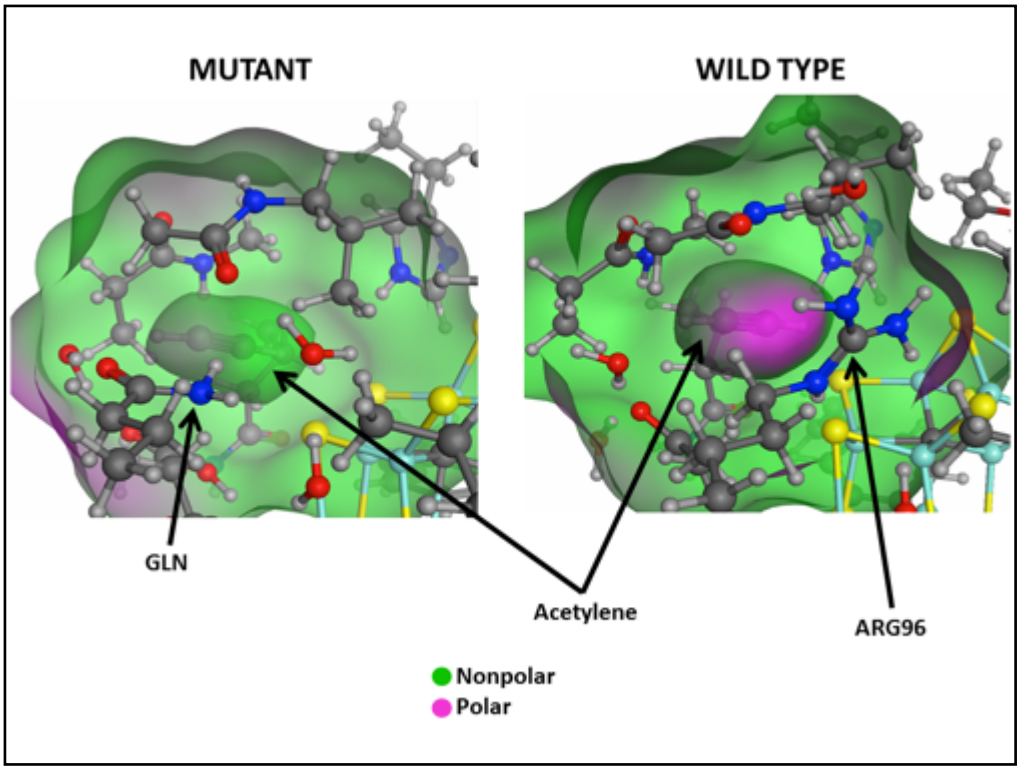


Figure 4.5. The electrostatic features of the protein region surrounding acetylene in the α-96$^{Arg\rightarrow Gln}$ MoFe variant and wild type enzyme. Green regions represent nonpolar environment whereas magenta is used for polar environment characterization.

"more hydrophobic" than that of the wild type enzyme. That is clearly expected in the light of the charged-to-neutral residue switch.

Considering the nonpolar nature of acetylene, the mutated MoFe protein has therefore active site features that make it more suitable for substrate (and analogues) accommodation. It is worth noting this result is purely thermodynamic and indicates that, taken for granted the kinetic accessibility of acetylene into the region close to cofactor both in WT and in α-96$^{Arg\rightarrow Gln}$ MoFe cases), it would be better accommodated within the α-96$^{Arg\rightarrow Gln}$ MoFe catalytic pocket than within that of the WT enzyme.

Table SI 5. reports a comparison of the most relevant interatomic distances (in Å) for α-96$^{Arg\rightarrow Gln}$ MoFe X-ray structure and the two DFT optimized models with total charge =0 (mutant and wild type). The scope is to evaluate possible structural variations (moves) of the substrate on going from R96Q to WT system. One of the two carbon atoms slightly moves in the WT (respect to R96Q), probably to find better accommodation in response to the Q-to-R switch.

Structural Analysis of Acetylene Bound MoFe

As previously stated, EPR measurements of the α-96$^{Arg\rightarrow Gln}$ MoFe variant have demonstrated the substrate acetylene to persist at the resting statFeMo-cofactor. Other biochemical and spectrscopic studies have suggested the location of substrate reduction to occur at the Fe6 position of the FeMo-cofactor.[1, 66] Our analysis of the nitrogenase α-96$^{Arg\rightarrow Gln}$ MoFe variant 1.70 Å crystal structure treated with acetylene, shows elongated

electron density ~4.4 Å away from the Fe6 position of the active site cofactor (Figure 4.6).

The glutamine substitution near the active site allows for a larger cavity in proximity to the proposed catalytic face of the FeMo-cofactor, and as shown through our computational analysis, is a more favorable pocket for acetylene to access than in the wild type protein. Furthermore, this substitution may facilitate acetylene to persist near the active site due to the new coordination environment. Other than the substitution at the 96 position, and the newly observed density assigned to be acetylene, the structure is very similar to the wild type, with no global conformational change observed. A

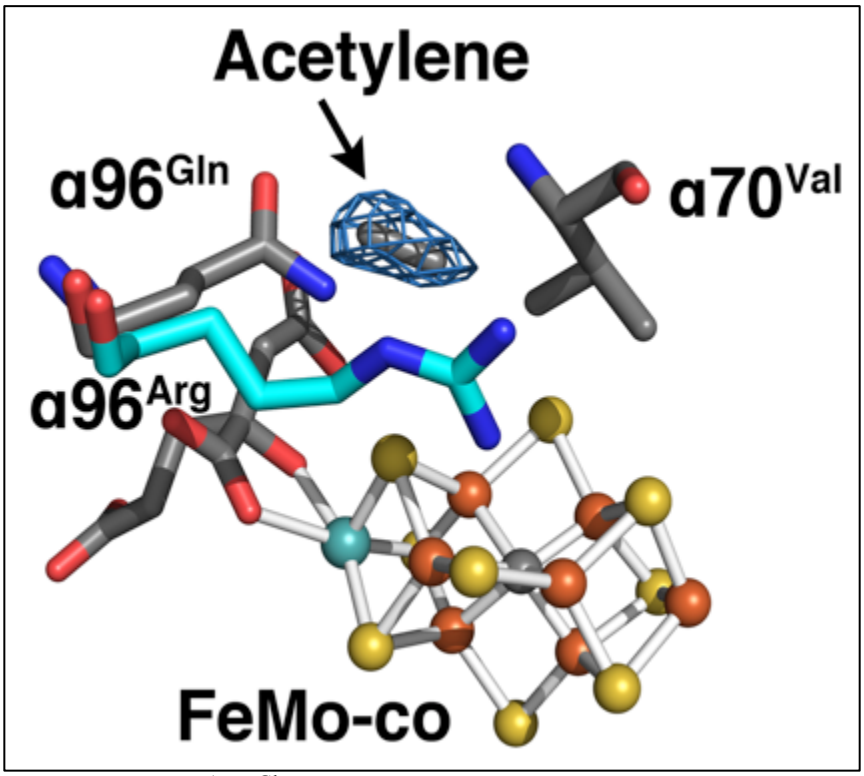


Figure 4.6. The α-96$^{Arg\rightarrow Gln}$ MoFe protein variant with acetylene modeled into $2F_o$-F_c experimental electron density (contoured to 1.0σ) in close proximity to the FeMo-cofactor. The WT MoFe α-96^{Arg} residue is shown in blue.

secondary structure similarity comparison was conducted using the SSM at European Bioinformatics Institute (http://www.ebi.ac.uk/msd-srv/ssm) and an examination of the root mean square standard deviation (RMSD) among all residues revealed a near identity between the two structures, with an average RMSD of 0.2 Å.

Conclusion

This crystal structure, supported by rigorous computational calculations, reveals for the first time the location of coordination of the mechanistically relevant substrate acetylene. This represent a significant advance in our knowledge of MoFe-mediated nitrogen reduction, considering the decades of work devoted to this system. Anthropogenic demand for fixed nitrogen is inevitably increasing, requiring novel methods to supplement existing sources. Crystal structures and computational analysis of FeMo-co interaction with substrates will certainly aid in the development of advanced mimetic nitrogen reducing catalysts.

CHAPTER FIVE

LIGHT-DRIVEN DINITROGEN REDUCTION CATALYZED BY A CDS:NITROGENASE MOFE PROTEIN BIOHYBRID

Contribution of Authors and Co-Authors

Manuscript in Chapter 5

Author: Katherine A. Brown

Contributions: Experimental design, nanoparticle synthesis, kinetic studies, data analysis

Co-Author: Derek F. Harris

Contributions: Kinetic studies, data analysis

Co-Author: Molly B. Wilker

Contributions: Nanoparticle synthesis, data analysis

Co-Author: Andrew J. Rasmussen

Contributions: Kinetic studies, data analysis

Co-Author: Hayden Hamby

Contributions: Nanoparticle synthesis, data analysis

Co-Author: Stephen M. Keable

Contributions: Protein purification, sample preparation/consolation

Co-Author: Gordana Dukovic

Contributions: PI of lab that provided nanoparticles

Co-Author: John W. Peters

Contributions: PI of lab that provided protein samples

Co-Author: Lance C. Seefeldt

Contributions: PI of lab that provided kinetic studies

Co-Author: Paul W. King

Contributions: Corresponding autor

Manuscript Information Page

Katherine A. Brown, Derek F. Harris, Molly B. Wilker, Andrew J. Rasmussen, Hayden Hamby, Stephen M. Keable, Gordana Dukovic, John W. Peters, Lance C. Seefeldt, Paul W. King
Science
Status of Manuscript:
___ Prepared for submission to a peer-reviewed journal
___ Officially submitted to a peer-review journal
____ Accepted by a peer-reviewed journal
_X_ Published in a peer-reviewed journal

Published by the American Association for the Advancement of Science

CHAPTER 5

LIGHT-DRIVEN DINITROGEN REDUCTION CATALYZED BY A CDS:NITROGENASE MOFE PROTEIN BIOHYBRID

Abstract

The splitting of dinitrogen (N_2) and reduction to ammonia (NH_3) is a kinetically complex and energetically challenging multistep reaction. In the Haber-Bosch process, N_2 reduction is accomplished at high temperature and pressure, whereas N2 fixation by the enzyme nitrogenase occurs under ambient conditions using chemical energy from adenosine 5′-triphosphate (ATP) hydrolysis. We show that cadmium sulfide (CdS) nanocrystals can be used to photosensitize the nitrogenase molybdenum-iron (MoFe) protein, where light harvesting replaces ATP hydrolysis to drive the enzymatic reduction of N_2 into NH_3. The turnover rate was 75 per minute, 63% of the ATP-coupled reaction rate for the nitrogenase complex under optimal conditions. Inhibitors of nitrogenase (i.e., acetylene, carbon monoxide, and dihydrogen) suppressed N_2 reduction. The CdS:MoFe protein biohybrids provide a photochemical model for achieving light-driven N_2 reduction to NH_3.

Chapter Introduction

The reduction of dinitrogen (N_2) to ammonia (NH_3) is the single largest input of fixed

nitrogen (N) into the global biogeochemical cycle. Although the overall reaction releases energy, the cleavage of the nitrogen-nitrogen triple bond has a very large activation barrier. In the industrial Haber-Bosch process, NH_3 is produced via a dissociative reaction involving coactivation of dihydrogen (H_2) and N_2 over an Fe-based catalyst.[67] The H_2 used for the reaction is produced by steam reforming of natural gas and results in coproduction of appreciable amounts of CO_2. The energy required (>600 kJ mol^{-1} NH_3) to achieve the high temperatures (500°C) and pressures (200 atm) necessary to drive the reaction is also largely derived from fossil fuels.[68, 69]

In nitrogen-fixing bacteria, the enzymatic reduction of N_2 to NH_3 is catalyzed by nitrogenase enzymes and proceeds via the hydrogenation of N_2 through metal-hydride intermediates rather than from reaction with H_2.[70] The Mo-dependent nitrogenase is a multiprotein complex composed of MoFe and Fe proteins, named after the metals in their active sites. Although nitrogenase functions at room temperature (25°C) and pressure (1 atm), it requires a large input of chemical energy provided by the hydrolysis of adenosine 5′-triphosphate (ATP) (Figure 5.1A).[70] A minimum of 16 moles of ATP ($\Delta G° = –488$ kJ mol^{-1} or 5 eV mol^{-1} of N_2 reduced) is required to reduce N_2 to NH_3. During catalysis, the Fe protein associates with and dissociates from the MoFe protein, resulting in the eight sequential electron transfer/ATP hydrolysis events required to generate 1 mole of NH_3.[43] Reducing equivalents accumulate at the catalytic site FeMo cofactor (FeMo-co) as Fe-hydrides,[71] which directly participate in conversion of N_2 to 2 moles of NH_3 with an obligatory stoichiometric reduction of two protons to make H_2 (Figure 5.1A).[70, 72] Low-potential chemical donors or photoexcited chromophores can directly deliver

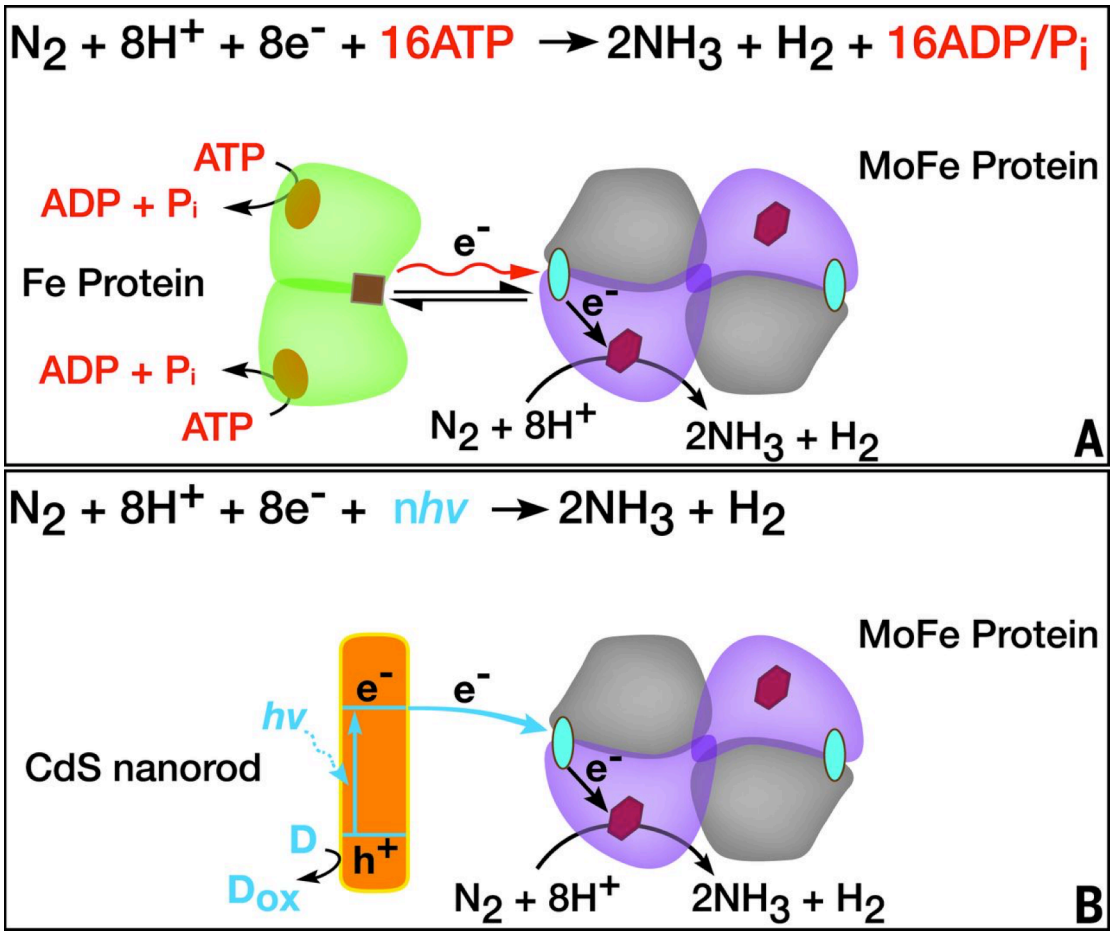


Figure 5.1. Reaction scheme for N_2 reduction to NH_3 by nitrogenase and the CdS:MoFe protein biohybrids. (A) reaction catalyzed by nitrogenase Fe protein (homodimer represented in green; MgATP binding site, orange sphere; [4Fe–4S] cluster, brown square) and MoFe protein (α2β2 tetramer represented in gray and purple; FeMo-co, red hexagon; [8Fe–7S] P-cluster, blue sphere). Hydrolysis of 16 ATP by Fe protein (*E*m = –0.42 V) is required for the sequential transfer (signified by the equilibrium arrow) of eight electrons (e–) to MoFe protein (*E*m = –0.31 V) for catalytic reduction of N_2 to $2NH_3$ and $1H_2$.[50] (B) The reaction catalyzed by CdS:MoFe protein biohybrids (measured product ratios were $1NH_3/10H_2$, with $n \approx 98$ absorbed photons; table S5.12). Under illumination, photon absorption (405 nm photon = 3.06 eV) by CdS nanorods (orange; lowest-energy transition, *E*g = 2.72 eV; fig. S5.1) generates electrons (E = –0.8 eV) and holes (E = +1.9 eV) (*15–17*), where direct electron injection from CdS into MoFe protein (blue arrow) is thermodynamically favored (Δ*E* = 0.5 V). The ground state of the CdS nanorod is regenerated by the oxidation of a sacrificial electron donor (D), such as HEPES (*E*m = + 0.8 V versus SHE).

electrons to the MoFe protein. Complexes between MoFe protein and the low-potential donor Eu(II)-L[26, 53] or Ru-photosensitizers[24, 25] support the catalytic reduction of protons or nonphysiological C or N substrates (e.g., C_2H_2, HCN, N_2H_4, N_3^-). However, these complexes are unable to catalyze N_2 reduction, and rates for nonphysiological substrates are low (up to 8.5 min^{-1}) compared to physiological reaction rates (e.g., 500 min^{-1} for C_2H_2 reduction). In the case of Ru-photosensitizers, it was shown that the Ru conjugate was unstable, resulting in the loss of photocatalytic rates and low quantum yields (QY ≤ 1%).[24, 25]

Materials and Methods

The CdS NRs synthesis was adapted from a published procedure for a seeded- growth procedure.[73] CdS seeds were synthesized from an initial mixture of 0.100 g cadmium oxide (CdO, 99.99%, Aldrich), 0.603 g octadecylphosphonic acid (ODPA, 99%, PCI), and 3.299 g trioctylphosphine oxide (TOPO, 99%, Aldrich), which were degassed then heated to 300 ºC under Ar for 30 min to dissolve the CdO. The solution was cooled to 120 ºC, degassed for 30 min, then heated to 320 ºC under Ar. After the temperature stabilized, sulfur stock solution (0.179 g hexamethyldisilathiane ((TMS)2S, synthesis grade, Aldrich) in 3 g of tributylphosphine (TBP, 97%, Aldrich) was quickly injected. The nanocrystals were allowed to grow at 250 ºC for 7.5 min, after which, the reaction was stopped by cooling and subsequently injecting toluene. The CdS seeds were precipitated with methanol. After transfer to the glovebox and washing with

toluene/methanol (2x), the final product was dissolved in trioctylphosphine (TOP, 97%, Strem). The CdS seeds had an absorbance peak at 408 nm, and the estimated molar absorptivity (ε) of the CdS seeds was 3.96 x 10^5 cm^{-1} M^{-1} at 408 nm.[74] To synthesize the rods, 0.086 g CdO, 3 g TOPO, 0.290 g ODPA, and 0.080 g hexylphosphonic acid (HPA, 99%, PCI) were degassed under vacuum at 120 ºC. The solution was heated to 350ºC under Ar for 30 min then 1.5 mL of TOP was added. When the temperature of the Cd- containing solution stabilized at 350 °C, the seed-containing solution (0.124 g of sulfur (S, 99.998%, Aldrich) in 1.5 mL of TOP mixed with 8×10^{-8} mol CdS QD seeds) was quickly injected. After an 8 min reaction time, the particles were cooled, transferred to the glovebox, and precipitated with a 1:1:1 mixture of acetone, toluene, and methanol to prepare for cleaning. The nanocrystals were cleaned by first redissolving in toluene, washing with octylamine, and precipitation with methanol. The nanocrystals were then redissolved in chloroform, washed with nonanoic acid, and precipitated with ethanol. The resulting particles were redissolved in toluene.

The CdS nanocrystals had an average diameter of 38 ± 5 Å, and an average length of 168 ± 16 Å as determined by measurements of 200 particles in transmission electron micrograph (TEM) images (Fig. S5.1). The ε value of the CdS nanocrystals was determined by correlating absorption spectra with Cd^{2+} concentrations determined from elemental analysis by inductively coupled plasma optical emission spectroscopy (ICP-OES). The estimated ε_{350} value of the CdS nanocrystals is 5.8 x 10^6 M^{-1} cm^{-1} based on a value of 1710 M^{-1} cm^{-1} per Cd^{2+} and an estimated number of Cd^{2+} per

nanocrystal from the average nanocrystal dimensions.

The synthesis was adapted from previously published procedures.[75, 76] For the preparation of CdSe nanocrystals capped with organic ligands, 4 g TOPO, 2.5 g hexadecylamine (HDA, 98%, Aldrich) and 0.075 g tetradecylphosphonic acid (TDPA, 99%, PCI) were dried and degassed under vacuum at 120 °C in a 25 mL three-neck flask. Under Ar, 1 mL of a stock solution of Se precursor [0.79 g of selenium shot (99.99%, Aldrich) in 8.3 g of TOP] was added and the mixture was again dried and degassed under vacuum at 110 °C. With the reaction temperature stabilized at 300 °C under Ar, 1.5 mL of Cd precursor stock solution [0.12 g of cadmium acetate (99.999%, Strem) in 2.5 g of TOP] was quickly injected under vigorous stirring, resulting in nucleation of CdSenanocrystals. The temperature was set to 260 °C for nanocrystal growth. Growth times of 0.3 min, 1.0 min and 15 min were used to produce nanocrystals of varying diameters. After growth, the reaction mixture was cooled to 90 °C. The mixture was added to a 20 % (v/v) ethanol in chloroform solution and centrifuged to precipitate the nanocrystals. Under an inert atmosphere in a glovebox, the supernatant was discarded and the nanocrystals were redissolved in toluene. The solution was centrifuged to precipitate excess HDA. The resulting nanocrystals were washed with a 1:2 mixture of isopropanol:ethanol and redispersed in toluene. Nanoparticle diameters of 2.5, 2.7 and 3.4 nm were determined from the first excited state $1S_{3/2}(h) \rightarrow 1S(e)$ transition peak wavelength (515, 535 and 567 nm) as described in Yu *et al*.[74]

CdS and CdSe nanocrystals were solubilized in water by ligand exchange with

mercaptopropionic acid (MPA) by a procedure adapted from Amirav et al.[75] and described in Brown et al.[77] The resulting MPA-capped particles were dried under vacuum and dispersed in Tris buffer, pH 7.

TEM sample grids were prepared by drop casting on carbon film, 300 mesh copper grids from Electron Microscopy Sciences. The image at the 100 nm scale was acquired with a FEI Tecnai Spirit BioTwin operating at 100 keV and equipped with a bottom mounted FEI Eagle 4K camera. The image at the 20 nm scale was acquired with a FEI Tecnai F-20 operating at 200 keV and equipped with a Gatan Ultrascan US-4000 camera. Lengths and diameters were determined from an average of 200 nanocrystals.

Azotobacter vinelandii strain DJ995 (wild type MoFe protein) and DJ1003 (apo–MoFe protein) was grown and the corresponding nitrogenase MoFe proteins, with a 7xHis-tag near the carboxyl-terminal end of the α-subunit, were expressed and purified as described.[27] Protein concentrations were determined by the Biuret assay. The purities of these proteins were >95% based on SDS-PAGE analysis with Coomassie staining.

Handling of proteins and buffers was done in septum-sealed serum vials under an argon atmosphere or on a Schlenk vacuum line. All liquids were transferred using gas-tight syringes. All reagents were obtained from Sigma Aldrich (St. Louis, MO) or Fisher Scientific (Fair Lawn, NJ) and were used without further purification.

Different nanocrystal:MoFe protein biohybrids were prepared under a 100% N_2 atmosphere by mixing individual solutions of 10 μM CdS or CdSe nanocrystals and 4.3 μM MoFe protein tetramer (1 mg mL^{-1}) to achieve a final molar ratio of 2:1

nanocrystal:MoFe protein tetramer. The mixtures were diluted into 50 mM Tris-HCl, 5 mM NaCl, pH 7 and mM ascorbic acid to a final concentration of 200 nM nanocrystals and 100 nM MoFe protein tetramer and a final volume of 300 μL. Reactions were stirred for 30 min under illumination with a 405 nm diode light source (Ocean Optics) at 11 mW (~1.8 mW cm^{-2} at the sample) in sealed vials with a total volume of 1.5 mL. The amount of $H2$ produced was determined by gas chromatography (GC) on 0.2 mL of the headspace gas phase. Turnover frequencies (means of $N = 4$ samples) were calculated as the nmol of H_2 produced during the illumination time.

Donors were tested with CdS:MoFe protein biohybrids that were prepared under a 100% $N2$ atmosphere by mixing individual solutions of 2.5 μM CdS and 2.13 μM MoFe protein tetramer (0.5 mg mL^{-1}) to achieve a final molar ratio of 1:1 CdS:MoFe protein tetramer. The mixtures were diluted into 50 mM Tris-HCl, 5 mM NaCl, pH 7 and the hole scavenger under investigation (HEPES, MES and MOPS @ 500 mM, ascorbic acid @ 100 mM, or Tris alone @ 50 mM) to a final concentration of 16.7 nM CdS and MoFe protein and a final volume of 300 μL. Control reactions of CdS alone were prepared at a final concentration of 16.7 nM CdS in identical buffer conditions for each hole scavenger. Reactions were stirred for 30 min under illumination with a 405 nm diode light source (Ocean Optics) at 11 mW (~1.8 mW cm^{-2} at the sample) in sealed vials with a total volume of 1.5 mL.

CdS:MoFe protein biohybrids were prepared under a 100% $N2$ atmosphere by mixing individual solutions of 2.5 μM CdS and 2.13 μM MoFe protein tetramer (0.5

mg mL^{-1}) to achieve a final molar ratio of 1:1 CdS:MoFe protein tetramer. The mixtures were diluted into 500 mM HEPES, pH 7 to a final concentration of 16.7 nM CdS and MoFe protein and a final volume of 300 µL. Reactions were stirred under illumination with a 405 nm diode light source (Ocean Optics) at 25 mW cm^{-2} (~3.5 mW cm^{-2} at the sample) in sealed vials with a total volume of 1.5 mL. The amount of NH_3 produced was measured by colorimetric assay (BioVision), described in detail below. The amount of H_2 produced by CdS:MoFe protein biohybrids was determined by gas chromatography (GC) on 0.2 mL of the headspace gas phase. Reaction velocities (averages derived from 4 samples) were calculated as the total nmol of H_2 produced by each sample during the total illumination time (Figure. S5.3).

The amount of NH_3 produced was measured using a colorimetric ammonia assay kit (BioVision). Briefly, 50 µL of the CdS:MoFe protein reaction (total volume of 300 µL) was mixed with 50 µL of kit reaction buffer and incubated at 37 °C for 1 h. Calibration curves were prepared from CdS nanocrystals (16.67 nM) that had been kept in the dark with the appropriate amount of ammonium chloride (Fig. S5.2A). The presence of CdS in the kit shifted the baseline of the 570 nm absorbance signal but did not affect the slope of the A_{570} value vs. mol of NH_4Cl nor the linearity of the calibration curves. The sample absorbance at 570 nm was used to determine the amount of NH_3 present based on the calibration standards.

Samples of CdS:MoFe protein were prepared as described above in 100% N_2 atmosphere. The sample headspace was then equilibrated under 100% Ar, or 10%

acetylene, CO or H_2 and 90% N_2 prior to illumination. Solutions were stirred under illumination with 405 nm diode light (3.5 mW cm^{-2} at the sample) in sealed vials. The total amount of NH_3 and H_2 produced were measured as described above. Ammonia production was verified by a second, independent method of ammonia detection based on fluorescence detection using o-phthaladehyde.[28] CdS nanorods demonstrate a quenching effect on the fluorescence of this assay, so they were removed before the assay. After illumination, the samples were run through a 10 kDa spin concentrator (Corning Spin-X UF) at 14,000 rpm for 5 min to separate CdS:MoFe protein biohybrids. 50 μL of the flow trough was added to 1 mL of a solution of 20 mM o- phthalaldehyde, 0.2 M phosphate buffer (pH 7.3), 5% ethanol, 3.4 mM β-mercaptoethanol. Samples were incubated in the dark for 30 min at room temperature. The fluorescence ($\lambda_{excitation}/\lambda_{emission}$ = 410 nm/472 nm) of the solutions was measured using a Shimadzu Model RF-5301 PC spectrofluorometer. A calibration curve was created by preparing a solution of CdS:MoFe protein biohybrids (16.67 nM) in assay buffer, incubating it in the dark for 90 min, then running it through a 10 kDa spin concentrator. Ammonium chloride was then added, in appropriate amounts, to aliquots of the filtered solution to a final volume of 50 μL then reacted, incubated, and assayed as described above (Fig. S5.2B). Ammonia production above background levels was in agreement with the results of the colorimetric assay.

Results and Discussion

Here, we examined N_2 reduction by the MoFe protein when it is adsorbed onto CdS nanocrystals to form biohybrid complexes. Semiconductor nanocrystals are quantum-confined materials with size-tunable photoexcited electron and hole energy levels.[78] Different nanocrystalline materials were tested (table S5.4), and CdS nanorods ($d \approx 38 \pm 5$ Å, $l \approx 168 \pm 16$ Å; Figure. S5.1) were observed to deliver photogenerated electrons to the MoFe protein with the highest enzymatic turnover. The size, shape, and surface electrostatics of the CdS nanorods complement the MoFe protein dimensions ($d \approx 69$ Å, $l \approx 110$ Å) and surface electrostatics to support self-assembly into complexes.[77, 79] The lowest-energy transition of the CdS nanorods is in the visible region of the solar spectrum (Eg = 2.72 eV, λabsorption = 456 nm, Figure S5.1), and the reduction potential of the first photoexcited state transition, –0.8 V versus NHE,[77, 80, 81] is sufficiently negative to reduce the MoFe protein (–0.31 V)[50] to drive electron transfer for catalytic reduction of N_2 to NH_3 (Figure 5.1B).

Photoexcitation of the CdS:MoFe protein biohybrids

Photoexcitation of the CdS:MoFe protein biohybrids under a 100% N_2 atmosphere resulted in the direct light-driven reduction of N_2 to NH_3 (Figure 5.2, Figure. S5.2 and tables S5.5 to S5.7). Transfer of low-potential electrons to the MoFe protein from the photoexcited CdS nanorod replaced ATP-coupled electron transfer by the Fe protein. The

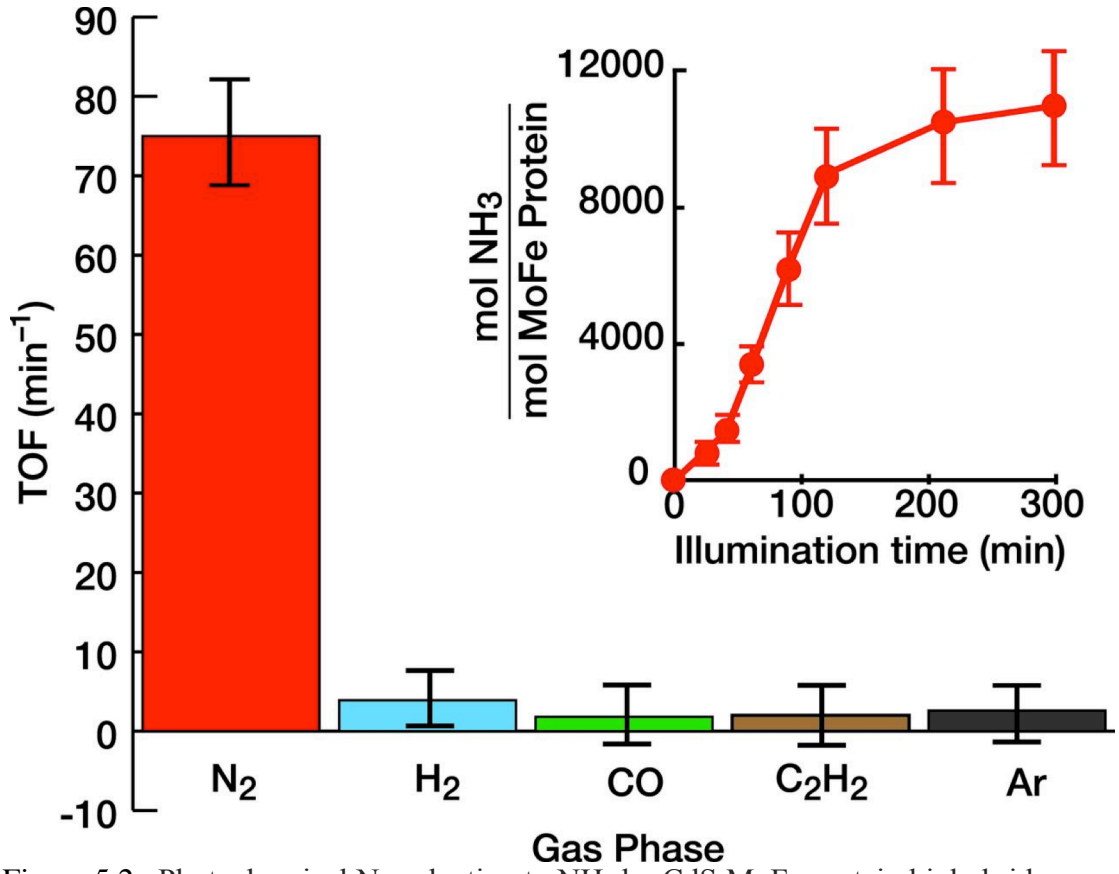


Figure 5.2. Photochemical N_2 reduction to NH_3 by CdS:MoFe protein biohybrids. The TOF of catalytic reduction of N_2 to NH_3 was measured under 100% N_2 (red). The effects of MoFe protein inhibitors on the TOF are shown for 10% of either H_2 (cyan), carbon monoxide (CO, green), or acetylene (C_2H_2, brown) in a bulk phase of 90% N_2. TOF for the CdS:MoFe protein biohybrids under 100% Ar (gray) is shown as a negative control for comparison. Measured values were taken after 2 hours of illumination at 25°C for reactions comprising 1:1 molar ratios of CdS nanorods and MoFe protein tetramer. Data are means of $N = 4$ independent measurements ± SD calculated by standard error propagation. (Inset) Time course of NH_3 production by CdS:MoFe protein biohybrids under 100% N_2. TON = 1.1×10^4 mol NH_3 (mol MoFe protein)$^{-1}$ (table S5.14).

reaction required a sacrificial electron donor, HEPES, which produced a high turnover frequency (TOF) with a low background compared to other donors (table S5.5). Control reactions that lacked a key component (e.g., HEPES, CdS, light, or a functional MoFe protein) or utilized apo-MoFe protein that lacks FeMo-co did not produce NH_3 (tables

S5.6 and S5.8). Illumination under ~3.5 mW cm^{-2} of 405-nm light led to peak NH_3 production rates of 315 ± 55 nmol NH_3 (mg MoFe protein)$^{-1}$ min^{-1} at a TOF of 75 min^{-1} (Figure 5.2 and table S5.9). The values correspond to 63% of the NH_3 production [500 nmol NH_3 (mg MoFe protein)$^{-1}$ min^{-1}], and TOF (119 min^{-1}) catalyzed by the Fe protein and ATP-dependent reaction under optimal conditions (table S5.9). The estimated QY of 3.3% for conversion of absorbed photons to NH_3 (QY = 23.5% for the coproduction of NH_3 and H_2; tables S5.10 and S5.11) is higher than reported for other nonphysiological reactions.[24, 25] N_2 reduction persisted for up to 5 hours under constant illumination (Figure 5.2, inset; tables S5.12 and S5.13) with a turnover number (TON) of 1.1×10^4 mol NH_3 (mol MoFe protein)$^{-1}$. This indicates that the MoFe protein in CdS:MoFe protein biohybrids can function at rates comparable to physiological TOF by nitrogenase. The mechanism of N_2 reduction by the MoFe protein coproduces H_2 (Figure 5.1), which was also observed as a coproduct during CdS:MoFe protein photocatalytic N_2 reduction (Figure. S5.3 and tables S5.7 and S5.8). This supports a mechanism of N_2 reduction by the CdS:MoFe protein biohybrids that is analogous to the mechanism of MoFe protein:Fe protein catalysis. CdS inhibition of Fe protein–dependent catalysis (table S5.14) indicates that CdS binds at or near the Fe protein binding site on MoFe protein (Figure 5.1B); however, it is not known whether the P-cluster serves as an intermediate in electron transfer during photocatalysis.

Additional evidence that the N_2 reduction reaction occurs at FeMo-co of the MoFe protein was observed with known inhibitors of Mo-dependent nitrogenase activity. Acetylene (C_2H_2), carbon monoxide (CO), and H_2 are all known to specifically inhibit the

N_2 reduction reaction at FeMo-co.[82, 83] Acetylene acts as a substrate to inhibit N_2 and proton reduction at FeMo-co. In contrast, CO inhibits N_2 reduction by blocking the N_2 binding site at FeMo-co, but proton reduction to H_2 is unaffected.[84] The addition of either H_2, CO, or C_2H_2 at 10% to a 90% N_2 gas phase decreased the N_2 reduction rates by CdS:MoFe protein biohybrids to the background levels observed with apo-MoFe protein (Figure 5.2 and tables S5.15 and S5.16). The results are consistent with the effect of these inhibitors on preventing MoFe protein catalysis in the Fe protein, ATP-driven physiological reaction. Photochemical H_2 production by CdS:MoFe protein biohybrids was also inhibited by 10% C_2H_2, but only slightly decreased under 10% CO compared to rates under 100% N_2 (Figure S5.3). Consistent with N_2 being a substrate of CdS:MoFe protein biohybrids, the rates of H_2 production were 25% higher when N_2 was replaced with 100% argon (Figure S5.3). Together, the inhibition results are consistent with photocatalysis by CdS:MoFe protein biohybrids occurring at the FeMo-co site of the MoFe protein by a mechanism that is similar to that for the Fe protein, ATP-coupled reaction.

Although the CdS nanorods have a low photoexcited state potential (–0.8 V versus NHE), other reductants, such as Eu(II)-L, have lower potentials (as low as –1.2 V versus NHE), yet only the CdS nanorods support N_2 reduction by MoFe protein. This indicates that some aspect of the nanorods, other than photochemical driving force alone, contributes to the achievement of N_2 reduction. One possible explanation is the rapid delivery of successive electrons due to strong light absorption by the CdS nanorods, which could allow achievement of the four-electron reduced FeMo-co state (E4) that is required for N_2

binding and reduction.[70, 71] Slow accumulation of electrons (low e-flux) on FeMo-co in the presence of other (photo)chemical donors[24-26, 53] could allow less reduced FeMo-co states (e.g., E2) to oxidize by evolving H_2 before N_2 binds. It is also possible that the binding of the CdS nanorod to the MoFe protein could induce protein conformational changes necessary to achieve N_2 reduction that normally occur upon Fe protein binding.[53]

Conclusion

The ability to create complexes between nanomaterials and MoFe protein and other enzymes establishes that photoexcited electrons can be used to drive difficult catalytic transformations while providing new tools for mechanistic investigations. Likewise, the light-harvesting properties of nanomaterials are highly tunable, and their unique optical properties can be used to probe in fine detail how changes in structure and energetics control electron transfer and macroscopic reaction rates. Biohybrid complexes can be used to examine how the flux and thermodynamics of photoexcited electron transfer influence the turnover and fidelity of catalytic product formation. Pairing biohybrid photochemical complexes with time-resolved methods is likely to enable profound new insights into the stepwise processes that underpin these challenging chemical reactions.

Concluding Remarks

Biological nitrogen fixation plays a crucial role in feeding humanity, and further research of this process may allow for advances in synthetic nitrogen fixation. The research described in this document addresses some of the outstanding unknowns that still remain with regards to our understanding of MoFe mediated nitrogen catalysis. As with many difficult questions, some ambiguity may remain in the outcomes of these studies, however, the evidence is compelling and provides intriguing insight into this complex process. The unidirectional gated electron transfer orchestrated by this enzyme is an elegant operation, and two of the studies presented here may help to elucidate this mechanism.

First, in chapter 2, research was presented that shows three key aromatic amino acids buried deep within the protein, can have profound biochemical effects on the mechanism of electron transfer when substituted. Instead of utilizing the requisite Fe protein electron donor, a histidine substitution conferred the ability to accept electetrons from polyaminocarboxylate ligated Eu(II). Furthermore, computational analysis suggests a dynamic coupling between the motion of the Fe protein and the MoFe protein region where these key aromatic residues reside, while crystallographic analysis reveals only minor changes around the active site, with no global conformational changes observed. Indeed these results only bring up new questions that may be answered once we are able to truly observe the global conformational changes that take place during catalysis.

Chapter 3 reported on an unobserved structural conformation of the P-cluster that had been previously characterized spectroscopically, but not structurally. Using two loops staked on top of each other, we were able to trap crystals and soak them in the presence of redox mediators held at defined potentials for expended periods of time. We were able to observe redox mediated conformational changes to the P-cluster in crystal structures, however, exposure to the mediators increased the crystals sensitivity to radiation damage, and reduced the quality of the data. Although the data for mediator treated structures were not of high quality, the previously characterized P^N and P^{2+}, and the newly observed P^{1+} state, could be clearly visualized in electron density. Additionally, the data were of sufficient quality to generate interpretable difference electron density maps to support the individual assignments of the three states. This study provides fascinating insight into some of the conformational changes associated with gated electron transfer during catalysis. However, once again these structural differences are limited to the P-cluster and an understanding of the global conformational changes is required to fully describe electron transfer in this system.

The 4^{th} chapter describes a study in which the nitrogenase substrate acetylene was characterized in close proximity to the FeMo-cofactor active site of a MoFe protein variant through crystallographic and computational analysis. The substrate acetylene is considered a model substrate analog to nitrogen, and is routinely used to measure the specific activity of purified nitrogenase. It was previously shown that substitutions of a key residue near the FeMo-cofactor allowed for the substrate acetylene to persist at the active site under resting state conditions. This observation allowed for the unique

opportunity to capture substrates at the active site in a crystal structure without the need for Fe protein electron donation. A crystal structure was solved using crystals where acetylene was saturated into the protein solution and precipitant solution. An elongated electron density feature was observed in close proximity to the active site, and in fact was positioned near an iron atom proposed to be the site of substrate binding. A rigorous computational analysis was carried out on this crystal structure and the conclusions support the assignment of acetylene at this position. This represents the first known structure of a mechanistically relevant substrate interacting with the active site of nitrogenase, and indeed provides previously unknown insight into nitrogenase catalysis. Finaly, chapter 5 revisits Fe protein independent electron transfer by describing a study in which cadmium sulfide (CdS) nanocrystals where used to achieve substrate turnover through photoreduction. This is result provides further insight into how the nitrogenase MoFe protein can create complexes with nanomaterials to drive electron transfer. Furthermore, the light harvesting properties of nanomaterials are highly tunable, and probing byohybrid photochemical complexes with time-resolved methods is likely to provide new insights into how electron transfer influences the turnover and fidelity of product formation.

In addition to the knowledge gained into nitrogenase catalysis, mechanistic insight derived from this research has the potential to impact the broader field of metalloprotein research through the parallels that can be draw from this system. This fascinating ambient condition reaction catalyzed by the nitrogenase biochemical apparatus has profound implications for humanity. The ultimate aim of this basic research is to lay the foundation

for the development of advanced bio-mimetic materials that could catalyze nitrogen fixation under less energy intensive conditions. Modeling and fabrication of these bio-inspired materials will be incumbent upon a more comprehensive understanding of the mechanistic fundamentals of this complex multi-component metalloreductase.

REFERENCES CITED

1. Seefeldt, L. C., Hoffman, B. M., and Dean, D. R. (2009) Mechanism of Mo-dependent nitrogenase, *The Annual Review of Biochemistry 78*, 701-722.

2. Burgess, B. K., and Lowe, D. J. (1996) Mechanism of Molybdenum Nitrogenase, *Chemical Reviews 96*, 2983-3012.

3. Hoffman, B. M., Lukoyanov, D., Dean, D. R., and Seefeldt, L. C. (2013) Nitrogenase: a draft mechanism, *Accounts of chemical research 46*, 587-595.

4. Georgiadis, M. M., Komiya, H., Chakrabarti, P., Woo, D., Kornuc, J., and Rees, D. (1992) Crystallographic structure of the nitrogenase iron protein from *Azotobacter vinelandii*, *Science 257*, 1653-1659.

5. Chan, M. K., Kim, J., and Rees, D. (1993) The nitrogenase FeMo-cofactor and P-cluster pair: 2.2 A Resolution Structures, *Science 260*, 7.

6. Shah, V. K., and Brill, W. J. (1981) Isolation of a molybdenum--iron cluster from nitrogenase, *Proceedings of the National Academy of Sciences 78*, 3438-3440.

7. Danyal, K., Dean, D. R., Hoffman, B. M., and Seefeldt, L. C. (2011) Electron transfer within nitrogenase: evidence for a deficit-spending mechanism, *Biochemistry 50*, 9255-9263.

8. Martin, A., Burgess, B., Iismaa, S., Smartt, C., Jacobson, M., and Dean, D. (1989) Construction and characterization of an *Azotobacter vinelandii* strain with mutations in the genes encoding flavodoxin and ferredoxin I, *Journal of bacteriology 171*, 3162-3167.

9. Thorneley, R. N., and Lowe, D. J. (1985) Kinetics and mechanism of the nitrogenase enzyme system, *Molybdenum enzymes 7*, 89-116.

10. Kim, J., and Rees, D. (1992) Structural models for the metal centers in the nitrogenase molybdenum-iron protein, *Science 257*, 1677-1682.

11. Peters, J. W., Stowell, M. H., Soltis, S. M., Finnegan, M. G., Johnson, M. K., and Rees, D. C. (1997) Redox-dependent structural changes in the nitrogenase P-cluster, *Biochemistry 36*, 1181-1187.

12. Chan, J. M., Christiansen, J., Dean, D. R., and Seefeldt, L. C. (1999) Spectroscopic evidence for changes in the redox state of the nitrogenase P-cluster during turnover, *Biochemistry 38*, 5779-5785.

13. Benton, P. M., Mayer, S. M., Shao, J., Hoffman, B. M., Dean, D. R., and Seefeldt, L. C. (2001) Interaction of acetylene and cyanide with the resting state of nitrogenase α-96-substituted MoFe proteins, *Biochemistry 40*, 13816-13825.

14. Spatzal, T., Aksoyoglu, M., Zhang, L., Andrade, S. L., Schleicher, E., Weber, S., Rees, D. C., and Einsle, O. (2011) Evidence for interstitial carbon in nitrogenase FeMo cofactor, *Science 334*, 940-940.

15. Seefeldt, L. C., Hoffman, B. M., and Dean, D. R. (2012) Electron transfer in nitrogenase catalysis, *Current opinion in chemical biology 16*, 19-25.

16. Dos Santos, P. C., Igarashi, R. Y., Lee, H.-I., Hoffman, B. M., Seefeldt, L. C., and Dean, D. R. (2005) Substrate interactions with the nitrogenase active site, *Accounts of chemical research 38*, 208-214.

17. Barney, B. M., Yurth, M. G., Dos Santos, P. C., Dean, D. R., and Seefeldt, L. C. (2009) A substrate channel in the nitrogenase MoFe protein, *JBIC Journal of Biological Inorganic Chemistry 14*, 1015-1022.

18. Yang, Z. Y., Danyal, K., and Seefeldt, L. C. (2011) Mechanism of Mo-dependent nitrogenase, *Methods in Molecular Biology 766*, 9-29.

19. Einsle, O., Tezcan, F. A., Andrade, S. L., Schmid, B., Yoshida, M., Howard, J. B., and Rees, D. C. (2002) Nitrogenase MoFe-protein at 1.16 Å resolution: a central ligand in the FeMo-cofactor, *Science 297*, 1696-1700.

20. Hageman, R. V., and Burris, R. H. (1978) Nitrogenase and nitrogenase reductase associate and dissociate with each catalytic cycle, *Proceedings of the National Academy of Sciences 75*, 2699-2702.

21. Duval, S., Danyal, K., Shaw, S., Lytle, A. K., Dean, D. R., Hoffman, B. M., Antony, E., and Seefeldt, L. C. (2013) Electron transfer precedes ATP hydrolysis during nitrogenase catalysis, *Proceedings of the National Academy of Sciences of the United States of America 110*, 16414-16419.

22. Lowe, D., Ashby, G., Brune, M., Knights, H., Webb, M., and Thorneley, R. (1995) ATP hydrolysis and energy transduction by nitrogenase, In *Nitrogen Fixation: Fundamentals and Applications*, pp 103-108, Springer.

[23] Shah, V. K., Stacey, G., and Brill, W. J. (1983) Electron transport to nitrogenase. Purification and characterization of pyruvate: flavodoxin oxidoreductase. The nifJ gene product, *Journal of Biological Chemistry 258*, 12064-12068.

24. Roth, L. E., Nguyen, J. C., and Tezcan, F. A. (2010) ATP-and iron– protein-independent activation of nitrogenase catalysis by light, *Journal of the American Chemical Society 132*, 13672-13674.

25. Roth, L. E., and Tezcan, F. A. (2012) ATP-uncoupled, six-electron photoreduction of hydrogen cyanide to methane by the molybdenum–iron protein, *Journal of the American Chemical Society 134*, 8416-8419.

26. Danyal, K., Inglet, B. S., Vincent, K. A., Barney, B. M., Hoffman, B. M., Armstrong, F. A., Dean, D. R., and Seefeldt, L. C. (2010) Uncoupling nitrogenase: catalytic reduction of hydrazine to ammonia by a MoFe protein in the absence of Fe protein-ATP, *Journal of the American Chemical Society 132*, 13197-13199.

27. Christiansen, J., Goodwin, P. J., Lanzilotta, W. N., Seefeldt, L. C., and Dean, D. R. (1998) Catalytic and Biophysical Properties of a Nitrogenase Apo-MoFe Protein Produced by an ifB-Deletion Mutant of Azotobacter v inelandii, *Biochemistry 37*, 12611-12623.

28. Corbin, J. L. (1984) Liquid chromatographic-fluorescence determination of ammonia from nitrogenase reactions: A 2-min assay, *Applied and environmental microbiology 47*, 1027-1030.

29. Vincent, K. A., Tilley, G. J., Quammie, N. C., Streeter, I., Burgess, B. K., Cheesman, M. R., and Armstrong, F. A. (2003) Instantaneous, stoichiometric generation of powerfully reducing states of protein active sites using Eu (II) and polyaminocarboxylate ligands, *Chemical Communications*, 2590-2591.

30. Ng, J. D., Gavira, J. A., and García-Ruíz, J. M. (2003) Protein crystallization by capillary counterdiffusion for applied crystallographic structure determination, *Journal of structural biology 142*, 218-231.

31. Sarma, R., Barney, B. M., Keable, S., Dean, D. R., Seefeldt, L. C., and Peters, J. W. (2010) Insights into substrate binding at FeMo-cofactor in nitrogenase from the structure of an alpha-70(Ile) MoFe protein variant, *Journal of Inorganic Biochemistry 104*, 385-389.

32. Otwinowski, Z., and Minor, W. (1997) [20] Processing of X-ray diffraction data collected in oscillation mode, *Methods in enzymology 276*, 307-326.

33. Murshudov, G. N., Vagin, A. A., and Dodson, E. J. (1997) Refinement of macromolecular structures by the maximum-likelihood method, *Acta Crystallographica Section D: Biological Crystallography 53*, 240-255.

34. Atilgan, A., Durell, S., Jernigan, R., Demirel, M., Keskin, O., and Bahar, I. (2001) Anisotropy of fluctuation dynamics of proteins with an elastic network model, *Biophysical journal 80*, 505-515.

35. Tirion, M. M. (1996) Large amplitude elastic motions in proteins from a single-parameter, atomic analysis, *Physical review letters 77*, 1905.

36. Balabin, I. A., Yang, W., and Beratan, D. N. (2009) Coarse-grained modeling of allosteric regulation in protein receptors, *Proceedings of the National Academy of Sciences 106*, 14253-14258.

37. Leioatts, N., Romo, T. D., and Grossfield, A. (2012) Elastic network models are robust to variations in formalism, *Journal of chemical theory and computation 8*, 2424-2434.

38. Tezcan, F. A., Kaiser, J. T., Mustafi, D., Walton, M. Y., Howard, J. B., and Rees, D. C. (2005) Nitrogenase Complexes: Multiple Docking Sites for a Nucleotide Switch Protein, *Science 309*, 1377-1380.

39. Danyal, K., Mayweather, D., Dean, D. R., Seefeldt, L. C., and Hoffman, B. M. (2010) Conformational gating of electron transfer from the nitrogenase Fe protein to MoFe protein, *Journal of the American Chemical Society 132*, 6894-6895.

40. Mayweather, D., Danyal, K., Dean, D. R., Seefeldt, L. C., and Hoffman, B. M. (2012) Temperature invariance of the nitrogenase electron transfer mechanism, *Biochemistry 51*, 8391-8398.

[41. Tezcan, F. A., Kaiser, J. T., Howard, J. B., and Rees, D. C. (2014) Structural evidence for asymmetrical nucleotide interactions in nitrogenase, *Journal of the American Chemical Society 137*, 146-149.

42. J B Howard, a., and Rees, D. C. (1994) Nitrogenase: A Nucleotide-Dependent Molecular Switch, *Annual Review of Biochemistry 63*, 235-264.

43. Hageman, R. V., and Burris, R. (1978) Nitrogenase and nitrogenase reductase associate and dissociate with each catalytic cycle, *Proceedings of the National Academy of Sciences 75*, 2699-2702.

44. Lowe, D. J., Fisher, K., and Thorneley, R. N. F. (1993) Klebsiella pneumoniae nitrogenase: pre-steady-state absorbance changes show that redox changes occur in the MoFe protein that depend on substrate and component protein ratio; a role for P-centres in reducing dinitrogen?, *Biochemical Journal 292*, 93-98.

45. Lindahl, P. A., Papaefthymiou, V., Orme-Johnson, W. H., and Münck, E. (1988) Mössbauer studies of solid thionin-oxidized MoFe protein of nitrogenase, *Journal of Biological Chemistry 263*, 19412-19418.

46. Yoo, S. J., Angove, H. C., Papaefthymiou, V., Burgess, B. K., and Münck, E. (2000) Mössbauer Study of the MoFe Protein of Nitrogenase from Azotobacter vinelandii Using Selective 57Fe Enrichment of the M-Centers, *Journal of the American Chemical Society 122*, 4926-4936.

47. Tittsworth, R. C., and Hales, B. J. (1993) Detection of EPR signals assigned to the 1-equiv-oxidized P-clusters of the nitrogenase MoFe-protein from Azotobacter vinelandii, *Journal of the American Chemical Society 115*, 9763-9767.

48. Lowery, T. J., Wilson, P. E., Zhang, B., Bunker, J., Harrison, R. G., Nyborg, A. C., Thiriot, D., and Watt, G. D. (2006) Flavodoxin hydroquinone reduces Azotobacter vinelandii Fe protein to the all-ferrous redox state with a S = 0 spin state, *Proceedings of the National Academy of Sciences 103*, 17131-17136.

49. Burgess, B. K., Jacobs, D. B., and Stiefel, E. I. (1980) Large-scale purification of high activity Azotobacter vinelandii nitrogenase, *Biochimica et Biophysica Acta (BBA)-Enzymology 614*, 196-209.

50. Lanzilotta, W. N., and Seefeldt, L. C. (1997) Changes in the midpoint potentials of the nitrogenase metal centers as a result of iron protein-molybdenum-iron protein complex formation, *Biochemistry 36*, 12976-12983.

51. Otwinowski, Z., and Minor, W. (1997) Methods in Enzymology, edited by CW Carter & RM Sweet, Vol. 276, Macromolecular Crystallography, part A, New York: Academic Press.

52. Lanzilotta, W. N., Christiansen, J., Dean, D. R., and Seefeldt, L. C. (1998) Evidence for coupled electron and proton transfer in the [8Fe-7S] cluster of nitrogenase, *Biochemistry 37*, 11376-11384.

53. Danyal, K., Rasmussen, A. J., Keable, S. M., Inglet, B. S., Shaw, S., Zadvornyy, O. A., Duval, S., Dean, D. R., Raugei, S., and Peters, J. W. (2015) Fe Protein-Independent Substrate Reduction by Nitrogenase MoFe Protein Variants, *Biochemistry 54*, 2456-2462.

54. Christiansen, J., Cash, V. L., Seefeldt, L. C., and Dean, D. R. (2000) Isolation and characterization of an acetylene-resistant nitrogenase, *Journal of Biological Chemistry 275*, 11459-11464.

55. Lee, H.-I., Igarashi, R. Y., Laryukhin, M., Doan, P. E., Dos Santos, P. C., Dean, D. R., Seefeldt, L. C., and Hoffman, B. M. (2004) An organometallic intermediate during alkyne reduction by nitrogenase, *Journal of the American Chemical Society 126*, 9563-9569.

56. Schimpl, J., Petrilli, H. M., and Blöchl, P. E. (2003) Nitrogen Binding to the FeMo-Cofactor of Nitrogenase, *Journal of the American Chemical Society 125*, 15772-15778.

57. Ahlrichs, R., Bär, M., Häser, M., Horn, H., and Kölmel, C. (1989) Electronic structure calculations on workstation computers: The program system turbomole, *Chemical Physics Letters 162*, 165-169.

58. Schäfer, A., Huber, C., and Ahlrichs, R. (1994) Fully optimized contracted Gaussian basis sets of triple zeta valence quality for atoms Li to Kr, *The Journal of Chemical Physics 100*, 5829-5835.

59. Schäfer, A., Horn, H., and Ahlrichs, R. (1992) Fully optimized contracted Gaussian basis sets for atoms Li to Kr, *The Journal of Chemical Physics 97*, 2571-2577.

60. Lee, C., Yang, W., and Parr, R. G. (1988) Development of the Colle-Salvetti correlation-energy formula into a functional of the electron density, *Physical review B 37*, 785.

61. Dance, I. (2005) The hydrogen chemistry of the FeMo-co active site of nitrogenase, *Journal of the American Chemical Society 127*, 10925-10942.

62. Grimme, S. (2004) Accurate description of van der Waals complexes by density functional theory including empirical corrections, *Journal of computational chemistry 25*, 1463-1473.

63. Klamt, A. (1995) Conductor-like screening model for real solvents: a new approach to the quantitative calculation of solvation phenomena, *The Journal of Physical Chemistry 99*, 2224-2235.

64. Klamt, A. (1996) Calculation of UV/Vis spectra in solution, *The Journal of Physical Chemistry 100*, 3349-3353.

65. Vicatos, S., Roca, M., and Warshel, A. (2009) Effective approach for calculations of absolute stability of proteins using focused dielectric constants, *Proteins: Structure, Function, and Bioinformatics 77*, 670-684.

66. Igarashi, R. Y., Dos Santos, P. C., Niehaus, W. G., Dance, I. G., Dean, D. R., and Seefeldt, L. C. (2004) Localization of a catalytic intermediate bound to the FeMo-cofactor of nitrogenase, *Journal of Biological Chemistry 279*, 34770-34775.

67. Ertl, G. (2008) Reactions at surfaces: From atoms to complexity (Nobel lecture), *Angewandte Chemie International Edition 47*, 3524-3535.

68. Kim, D., Sakimoto, K. K., Hong, D., and Yang, P. (2015) Artificial photosynthesis for sustainable fuel and chemical production, *Angewandte Chemie International Edition 54*, 3259-3266.

69. Lan, R., Irvine, J. T., and Tao, S. (2013) Synthesis of ammonia directly from air and water at ambient temperature and pressure, *Scientific reports 3*.

70. Hoffman, B. M., Lukoyanov, D., Yang, Z.-Y., Dean, D. R., and Seefeldt, L. C. (2014) Mechanism of nitrogen fixation by nitrogenase: the next stage, *Chemical reviews 114*, 4041-4062.

71. Lukoyanov, D., Yang, Z.-Y., Dean, D. R., Seefeldt, L. C., and Hoffman, B. M. (2010) Is Mo involved in hydride binding by the four-electron reduced (E4) intermediate of the nitrogenase MoFe protein?, *Journal of the American Chemical Society 132*, 2526-2527.

72. Lukoyanov, D., Yang, Z.-Y., Khadka, N., Dean, D. R., Seefeldt, L. C., and Hoffman, B. M. (2015) Identification of a Key Catalytic Intermediate Demonstrates That Nitrogenase Is Activated by the Reversible Exchange of N2 for H2, *Journal of the American Chemical Society 137*, 3610-3615.

73. Carbone, L., Nobile, C., De Giorgi, M., Sala, F. D., Morello, G., Pompa, P., Hytch, M., Snoeck, E., Fiore, A., and Franchini, I. R. (2007) Synthesis and micrometer-scale assembly of colloidal CdSe/CdS nanorods prepared by a seeded growth approach, *Nano letters 7*, 2942-2950.

74. Yu, W. W., Qu, L., Guo, W., and Peng, X. (2003) Experimental determination of the extinction coefficient of CdTe, CdSe, and CdS nanocrystals, *Chemistry of Materials 15*, 2854-2860.

75. Amirav, L., and Alivisatos, A. P. (2010) Photocatalytic hydrogen production with tunable nanorod heterostructures, *The Journal of Physical Chemistry Letters 1*, 1051-1054.

76. Mekis, I., Talapin, D. V., Kornowski, A., Haase, M., and Weller, H. (2003) One-pot synthesis of highly luminescent CdSe/CdS core-shell nanocrystals via organometallic and "greener" chemical approaches, *The Journal of Physical Chemistry B 107*, 7454-7462.

77. Brown, K. A., Wilker, M. B., Boehm, M., Dukovic, G., and King, P. W. (2012) Characterization of photochemical processes for H2 production by CdS nanorod–[FeFe] hydrogenase complexes, *Journal of the American Chemical Society 134*, 5627-5636.

78. Alivisatos, A. P. (1996) Semiconductor clusters, nanocrystals, and quantum dots, *Science 271*, 933.

79. Brown, K. A., Dayal, S., Ai, X., Rumbles, G., and King, P. W. (2010) Controlled assembly of hydrogenase-CdTe nanocrystal hybrids for solar hydrogen production, *Journal of the American Chemical Society 132*, 9672-9680.

80. Brus, L. (1986) Electronic wave functions in semiconductor clusters: experiment and theory, *The Journal of Physical Chemistry 90*, 2555-2560.

81. Tseng, H.-W., Wilker, M. B., Damrauer, N. H., and Dukovic, G. (2013) Charge transfer dynamics between photoexcited CdS nanorods and mononuclear Ru water-oxidation catalysts, *Journal of the American Chemical Society 135*, 3383-3386.

82. Dilworth, M. (1966) Acetylene reduction by nitrogen-fixing preparations from Clostridium pasteurianum, *Biochimica et Biophysica Acta (BBA)-General Subjects 127*, 285-294.

83. Schöllhorn, R., and Burris, R. (1967) Acetylene as a competitive inhibitor of N-2 fixation, *Proceedings of the National Academy of Sciences 58*, 213-216.

84. Winter, H. C., and Burris, R. (1976) Nitrogenase, *Annual review of biochemistry 45*, 409-426.

APPENDICES

APPENDIX A

SUPPLEMENTAL INFORMATION FROM CHAPTER 2

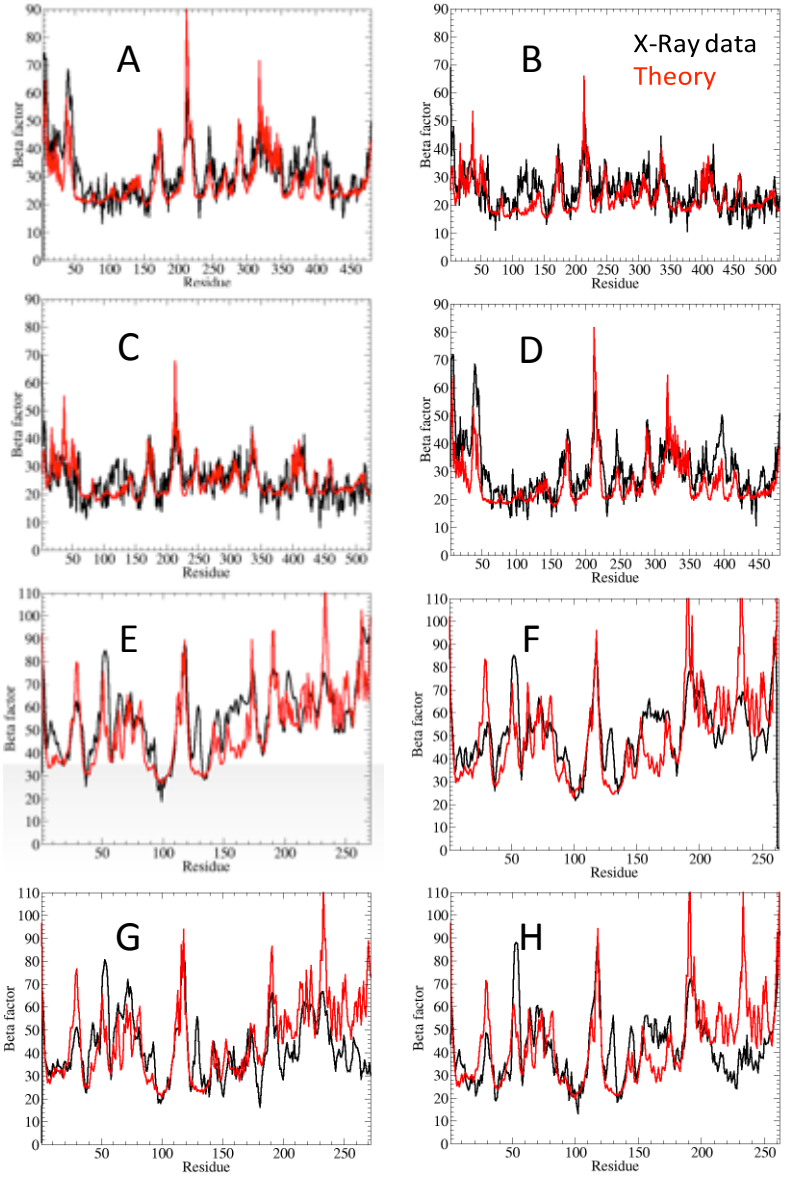


Figure S2.1. Beta factors for the nitrogenase complex. Comparison between the crystallographic (black line) and calculated (red line) beta factors (in $Å^2$) for the Fe protein/MoFe protein complex (crystal structure 2AFK). For sake of clarity, the beta factors are reported separately for each subunit (see Figure 1).

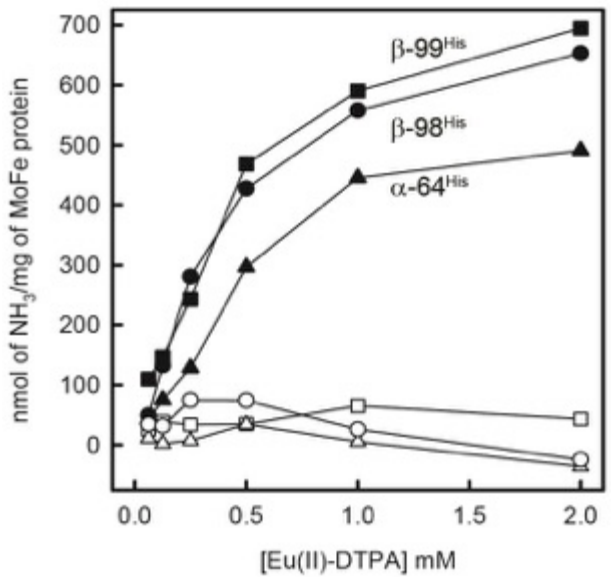


Figure S2.2: Concentration dependence of Eu (II)-DTPA on MoFe protein substrate reduction. The nmol of ammonia formed per mg MoFe protein is shown as a function of the concentration of Eu(II)–DTPA for the α-64^{His} (▲),β-98^{His} (●), and β-99^{His} (■) MoFe proteins. The corresponding open symbols are the no protein controls. All assays were conducted for 20 min with a final concentration of 100 mM hydrazine and 2.9 nmol (1.83 μM) of MoFe protein at 25^{o}C.

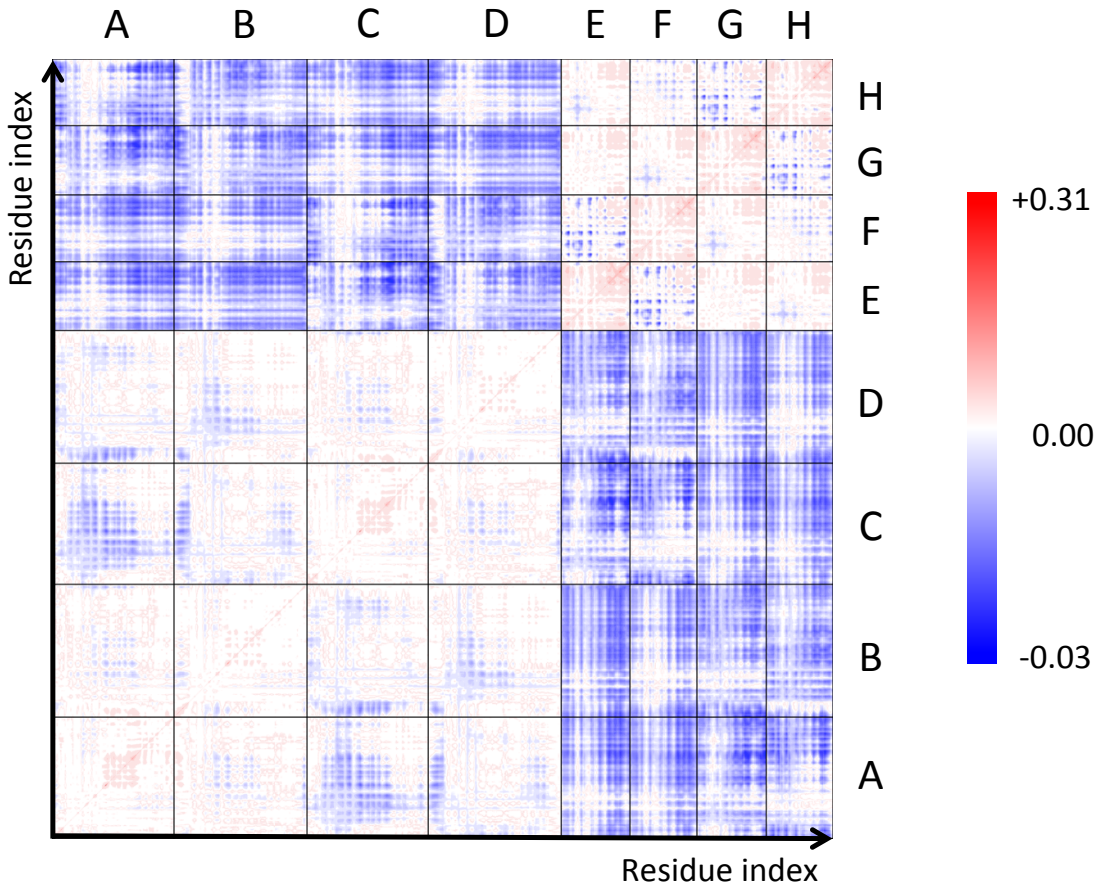


Figure S2.3: Covariance. Covariance matrix (in $Å^2$) for the MoFe protein/Fe protein complex. For sake of clarity, the matrix in divided in quadrants corresponding to the various possible subunit pairs (see Figure 1). Regions of correlated (in-phase) and anti-correlated (out-of-phase) motions are shown in red and blue, respectively.

Table S2.4: Data Statistics for ß-98$^{Tyr\rightarrow His}$ Structure	
cell dimensions	a = 80.80 Å b = 130.83 Å c = 108.11 Å α = γ = 90.00° b = 111.14
space group	$P2_1$
wavelength	λ_1 = 0.97947
resolution(Å)	35-1.97
completeness (%)	96.39 (84.1)[b]
obsd reflections	134339
unique reflections	127252
Avg redundancy	3.5
I/σ	2.5 (25.7) [b]
R_{sym}(%)	8.0 (37.6) [b]
Refinement Statistics	
Resolution (Å)	35-1.97
R_{cyrst}[c] (%)	21.5
R_{free}[c] (%)	26.8
Real Space CC[d] (%)	91.1
Mean B Value (overall; Å)	26.6
Coordinate Error (based on maximum likelihood, Å)	0.22
RMSD from ideality:	
Bonds (Å)	0.018
Angles (°)	3.044
Ramchandran Plot[e]:	
Most favored (%)	94.27
Additional allowed (%)	5.63
Outliers (%)	0.10

[b]Numbers in parenthesis refer to the highest resolution shell.

[c]R_{sym}=100*$S_hS_i|I_i(h)-<I(h)>|/S_hI(h)$ where $I_i(h)$ is the i^{th} measurement of reflection h and $<I(h)>$ is the average value of the reflection intensity.

[c]R_{cryst} = $S||F_o|-|F_c||/S|F_o|$ where F_o and F_c are the observed and calculated structure factor amplitudes used in refinement. R_{free} is calculated as R_{cryst}, but using the "test" set of structure factor amplitudes that were withheld from refinement. [d]Correlation coefficient (CC) is agreement between the model and $2mF_o$-DF_c electron density map. [e]Calculated using Molprobity

APPENDIX B

SUPPLEMENTAL INFORMATION FROM CHAPTER 3

Table S3.1: Data Statistics for P^{1+} Structure	
cell dimensions	a = 80.79 Å
	b = 130.78 Å
	c = 107.88 Å
	α = γ = 90.00°
	b = 110.85
space group	$P2_1$
wavelength	λ_1 = 0.97947
resolution(Å)	50-2.10
completeness (%)	57.06 (60.8)[b]
obsd reflections	150869
unique reflections	70560
Avg redundancy	2.1
I/σ	4.0 (1.3) [b]
R_{sym}(%)	14.2 (54.4) [b]
CC(1/2)	0.992 (0.814)[b]
Refinement Statistics	
Resolution (Å)	50-2.0
R_{cyrst}[c] (%)	24.86
R_{free}[c] (%)	28.75
Real Space CC[d] (%)	
Mean B Value (overall; Å)	46.5
Coordinate Error (based on maximum likelihood, Å)	0.22
RMSD from ideality:	
Bonds (Å)	0.013
Angles (°)	2.291
Ramchandran Plot[e]:	
Most favored (%)	94.92
Additional allowed (%)	4.67
Outliers (%)	0.40

[b]Numbers in parenthesis refer to the highest resolution shell.

[c]R_{sym}=100*$S_hS_i|I_i(h)-<I(h)>|/S_hI(h)$ where $I_i(h)$ is the i^{th} measurement of reflection h and $<I(h)>$ is the average value of the reflection intensity.

[c]R_{cryst} = $S||F_o|-|F_c||/S|F_o|$ where F_o and F_c are the observed and calculated structure factor amplitudes used in refinement. R_{free} is calculated as R_{cryst}, but using the "test" set of structure factor amplitudes that were withheld from refinement. [d]Correlation coefficient (CC) is agreement between the model and $2mF_o$-DF_c electron

density map. [e]Calculated using Molprobity

Table S3.2: Data Statistics for P^N Structure

cell dimensions	a = 79.09 Å
	b = 132.81 Å
	c = 108.77 Å
	α = γ = 90.00°
	b = 109.45
space group	$P2_1$
wavelength	λ_1 = 0.97947
resolution(Å)	50-2.2
completeness (%)	53.1 (57.5)[a]
obsd reflections	107763
unique reflections	56701
Avg redundancy	1.9
I/σ	5.9 (2.0) [a]
R_{sym}(%)	8.8 (38.8) [a]
CC(1/2)	.992(.340)[a]

[a]Numbers in parenthesis refer to the highest resolution shell.

Table S3.3: Data Statistics for P+2 Structure

cell dimensions	a = 81.18 Å
	b = 130.99 Å
	c = 107.85 Å
	α = γ = 90.00°
	b = 110.77
space group	$P2_1$
wavelength	λ_1 = 0.97947
resolution(Å)	50-2.10
completeness (%)	67.7 (68.9)[b]
obsd reflections	197146
unique reflections	95737
Avg redundancy	2.1
I/σ	4.6 (1.5) [b]
R_{sym}(%)	13.2 (42.8) [b]
CC(1/2)	0.994 (0.816)

[b]Numbers in parenthesis refer to the highest resolution shell.

APPENDIX C

SUPPLEMENTAL INFORMATION FROM CHAPTER 4

Table S4.1: Data Statistics for α-96$^{Arg\rightarrow Gln}$ Crystal Structure	
cell dimensions	a = 76.78 Å b = 128.20 Å c = 107.23 Å α = γ = 90.00° b = 109.09
space group	$P2_1$
wavelength	λ_1 = 0.97947
resolution(Å)	50-1.70
completeness (%)	89.6
obsd reflections	150869
unique reflections	70560
Avg redundancy	2.1
I/σ	4.0 (1.3) [b]
R_{sym}(%)	14.2 (54.4) [b]
CC(1/2)	0.992 (0.814)[b]
Refinement Statistics	
Resolution (Å)	50-1.70
R_{cyrst}[c] (%)	17.09
R_{free}[c] (%)	21.03
Real Space CC[d] (%)	
Mean B Value (overall; Å)	26.49
Coordinate Error (based on maximum likelihood, Å)	0.09
RMSD from ideality:	
Bonds (Å)	0.018
Angles (°)	2.79
Ramchandran Plot[e]:	
Most favored (%)	94.92
Additional allowed (%)	4.67
Outliers (%)	0.40

[b]Numbers in parenthesis refer to the highest resolution shell.

[c]R_{sym}=100*$S_hS_i|I_i(h)-<I(h)>|/S_hI(h)$ where $I_i(h)$ is the i^{th} measurement of reflection h and $<I(h)>$ is the average value of the reflection intensity.

[c]R_{cryst} = $S||F_o|-|F_c||/S|F_o|$ where F_o and F_c are the observed and calculated structure factor amplitudes used in refinement. R_{free} is calculated as R_{cryst}, but using the "test" set of structure factor amplitudes that were withheld from refinement. [d]Correlation coefficient (CC) is agreement between the model and $2mF_o$-DF_c electron density map. [e]Calculated using Molprobity

	X-Ray	DFT/Q=-4	DFT/Q=-4 vs X-ray	DFT/Q=0	DFT/Q=-0 vs X-ray
S Cys275 - Fe1	2.385	2.327	-0.058	2.273	-0.112
N His442 - Mo	2.425	2.339	-0.086	2.300	-0.125
O1 HCA - Mo	2.112	2.186	0.074	2.091	-0.021
O2 HCA - Mo	2.203	2.199	-0.004	2.124	-0.079
C int - Fe6	1.944	2.077	0.133	1.980	0.036
C int - Fe7	1.956	1.978	0.022	1.980	0.024
C int - Fe3	1.970	1.936	-0.034	2.096	0.126
C int - Fe2	1.962	1.974	0.012	1.929	-0.033
C int - Fe4	1.964	1.927	-0.037	1.945	-0.019
C int - Fe5	1.933	1.991	0.058	1.991	0.058
Fe1-S1	2.125	2.267	0.142	2.278	0.153
Mo-S2	2.320	2.421	0.101	2.427	0.107
Fe6-C1 ETD	4.453	4.094	-0.359	4.162	-0.291
Fe6-C2 ETD	5.326	5.063	-0.263	5.120	-0.206

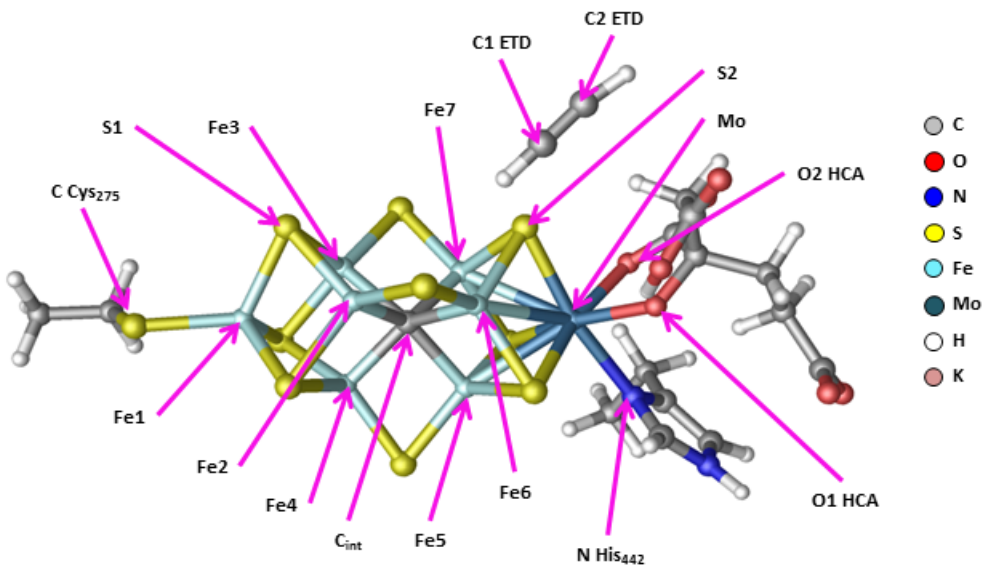


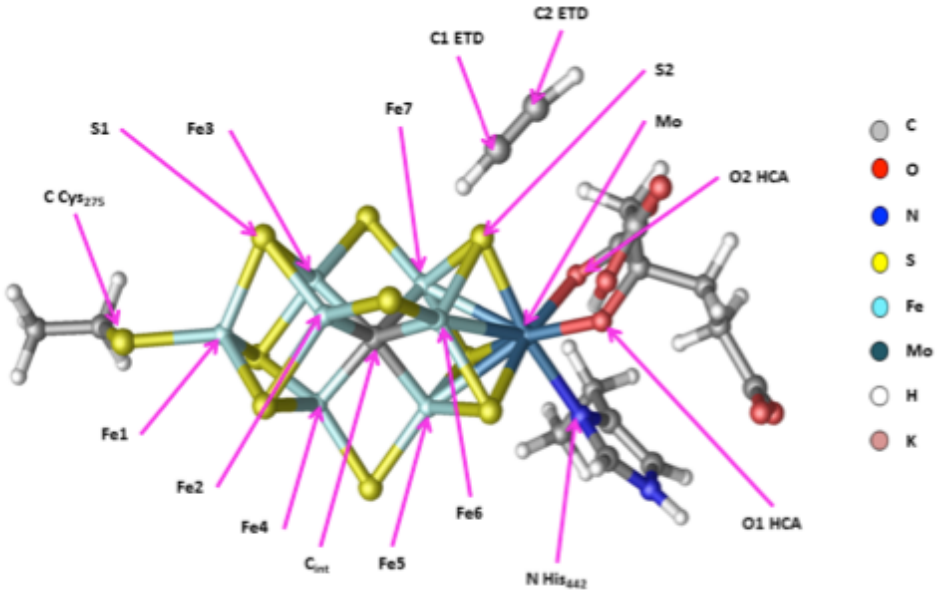
Table S4.1. Main interatomic distances (in Å) for X-Ray structure and the two DFT optimized models, bearing different total charge.

	Total charge model = -4		Total charge model = 0	
	DFT	DFT/solvation (ε=40)	DFT	DFT/solvation (ε=40)
ΔE	-17.3	-13.0	-18.1	-17.5
ΔE + BSSE (BSSE_avg)	-8.3 (-12.8)	-4.0 (-8.5)	-9.1 (-13.6)	-8.5 (-13.0)

Table S4.3. Comparative summary of binding energy of acetylene to active site, as computed by including different effects (total charge, solvation and counterpoise correction to BSSE; in parenthesis the correction is averaged as described in Ref 10, see also note 1). Present data already include dispersive effects (that are thus omitted in the shown notation). Energy is reported in kcal/mol.

	$\Delta E_{binding}$ (kcal/mol)			
	CHARGE	**DFT/BLYP/dispersion**	**DFT/BLYP/dispersion/COSMO (ε=40)**	**DFT/BLYP/dispersion/ COSMO (ε=40)/BSSE (BSSE_avg)[1]**
R96Q	-4	-17.3	-13.0	-4.0 (-8.5)
	0	-18.1	-17.5	-8.5 (-13.0)
WT	-4	-16.2	-12.3	-3.3 (-7.8)
	0	-14.8	-13.3	-4.3 (-8.8)

Table S4.4. Summary of the energetics of binding at various levels of modeling used in comparison between the wild type and variant proteins. [1]See note 3



	(Å)				
Interatomic distance.	**X-ray**	**R96Q**	**ΔX-ray (R96Q)**	**WT**	**ΔX-ray (WT)**
S Cys275 - Fe1	2.385	2.273	-0.112	2.273	-0.112
N His442 – Mo	2.425	2.300	-0.125	2.259	-0.166
O1 HCA – Mo	2.112	2.091	-0.021	2.123	0.011
O2 HCA – Mo	2.203	2.124	-0.079	2.165	-0.038
C int - Fe6	1.944	1.980	0.036	1.978	0.034
C int - Fe7	1.956	1.980	0.024	1.989	0.033
C int - Fe3	1.970	2.096	0.126	2.125	0.155
C int - Fe2	1.962	1.929	-0.033	1.933	-0.029
C int - Fe4	1.964	1.945	-0.019	1.936	-0.028
C int - Fe5	1.933	1.991	0.058	1.998	0.065
Fe1-S1	2.125	2.278	0.153	2.305	0.180
Mo-S2	2.320	2.427	0.107	2.421	0.101
Fe6-C1 acetylene	4.453	4.162	-0.291	3.965	-0.488
Fe6-C2 acetylene	5.326	5.120	-0.206	5.052	-0.274

Table S4.5. Comparison of the most relevant interatomic distances (in Å) for R96Q X-ray structure and the two DFT optimized models with total charge =0 (mutant and wild type). The scope is to evaluate possible structural variations (moves) of the substrate on going from R96Q to WT system. One of the two carbon atoms slightly moves in the WT (respect to R96Q), probably to find better accommodation in response to the Q-to-R switch.

APPENDIX D

SUPPLEMENTAL INFORMATION FROM CHAPTER 5

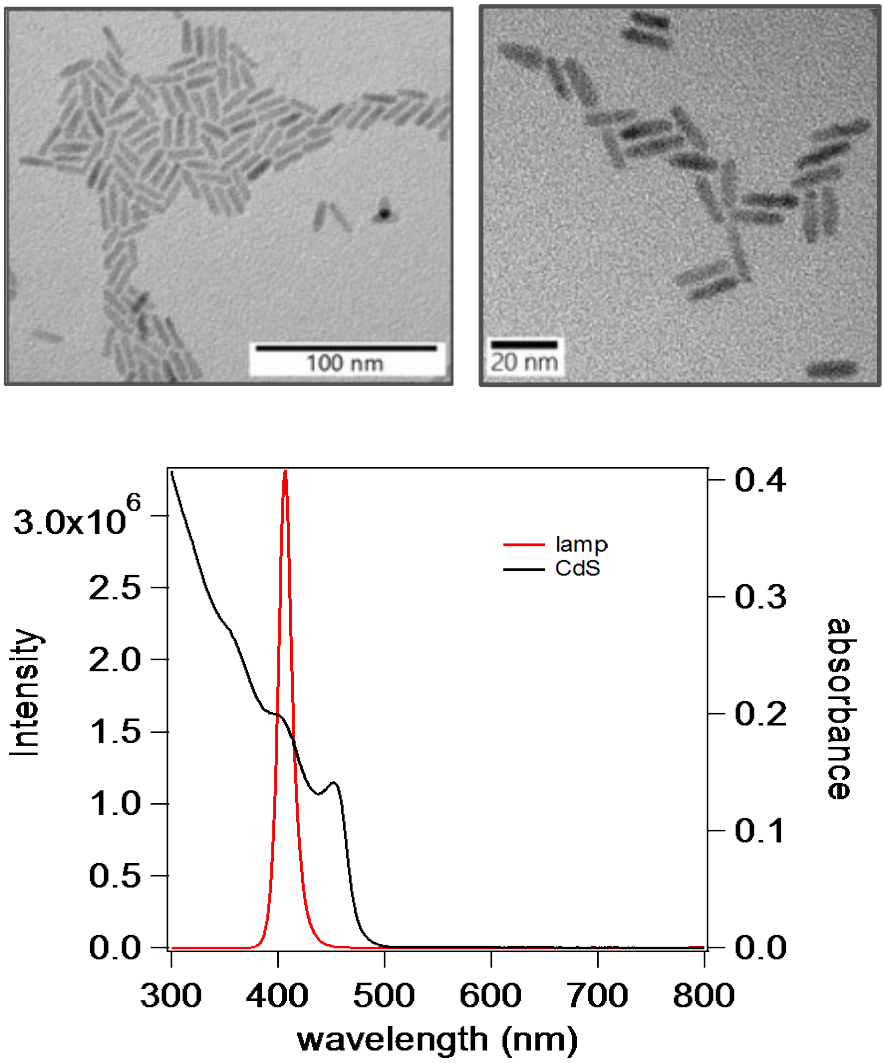


Figure S5.1(Top). TEM images of CdS nanocrystals with average dimensions of 38 ± 5 Å (*d*) x 168 ± 16 Å (*l*) (Mean of *N* = 200 measurements, ± SD). (Bottom). UV-vis spectrum of the CdS nanocrystals (black plot) overlayed with the emission spectrum of the 405 nm diode light source (red plot).

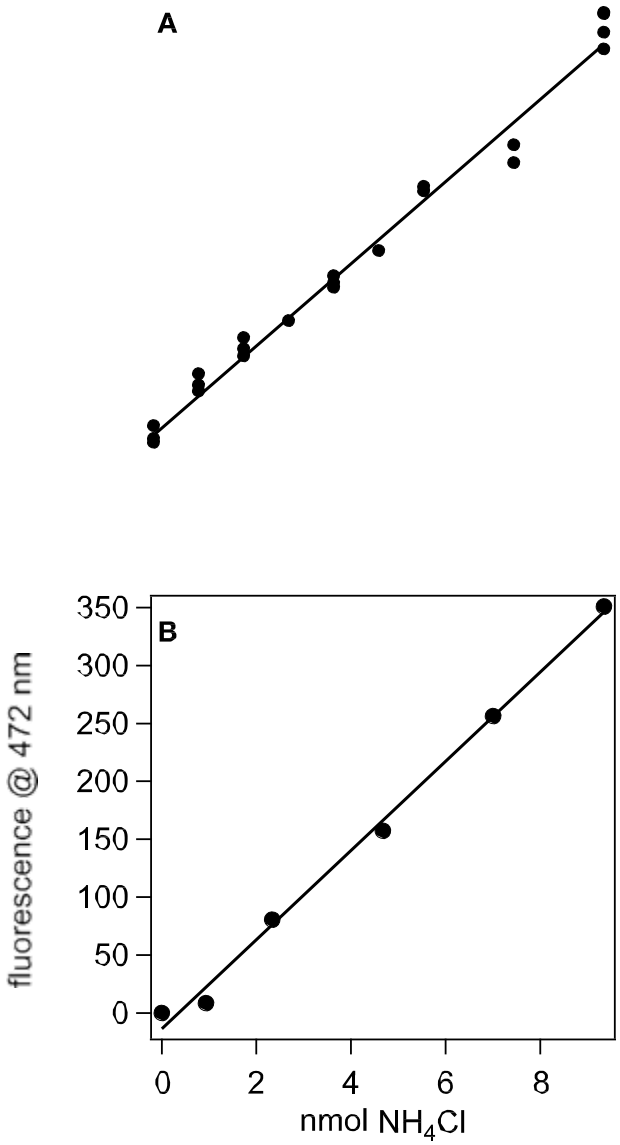


Figure S5.2. A. Calibration curve for colorimetric NH_3 assay using the BioVision kit. Ammonium chloride in the amount indicated on the x-axis was added to 50 µL of CdS nanoparticles (16.67 nM), then mixed with 50 µL of kit reaction buffer and incubated at 37 ^{0}C for 1 h. The absorbance at 570 nm was measured by plate reader (Tecan Infinate M200 Pro). The line shows linear fit (y = a*x + b) of $N = 4$ independent calibration curves (a = 0.0091 ± 0.0002, b = 0.061 ± 0.001; ± SD). The 570 nm absorbance value in the absence of added NH_4Cl (shown on the plot) is 0.0613 ± 0.0012 (mean of $N = 4$ measurements, ± SD). B. Calibration curve for o-phthalaldehyde colorimetric NH_3 assay. A solution of CdS:MoFe protein biohybrids (16.67 nM) in assay buffer were prepared, incubated in the dark for 90 min, then run through a 10 kDa spin concentrator (Corning Spin-X UF) at 14,000 rpm for 5 min to separate CdS:MoFe protein biohybrids. Ammonium chloride in the amount indicated

on the x-axis was added to aliquots of the filtered solution to a volume of 50µL. 1 mL of the o-phthalaldehyde solution was added and samples were incubated in the dark for 30 min at room temperature. The fluorescence ($\lambda_{excitation}/\lambda_{emission}$ 410 nm/472 nm) of the solutions was measured using a Shimadzu Model RF-5301 PC spectrofluorometer and the software provided with the instrument. The line shows linear fit ($y = a*x + b$) of the calibration curve ($a = 38.505$, $b = 165.43$).

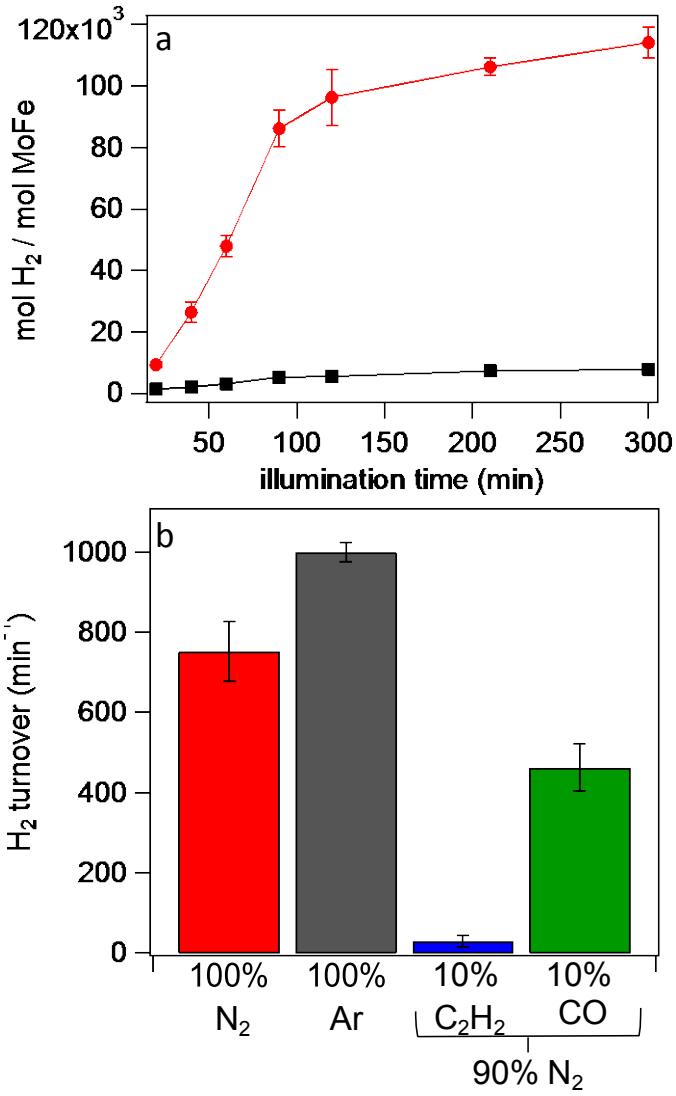


Figure S5.3. Photochemical H_2 production by CdS:MoFe protein biohybrids. (a) Time course of H_2 production by CdS:MoFe protein biohybrids (red circles) and CdS:apo–MoFe protein biohybrids (black squares). Reactions; 16.7 nM CdS, 16.7 nM MoFe protein or 16.7 nM apo–MoFe protein, 500 mM HEPES, pH 7.0. Reactions were equilibrated under 100% N_2 stirred under illumination with 3.5 mW cm^{-2} (at the sample) 405 nm light at 25 °C. (b) Effects of addition of MoFe protein inhibitors on the turn over frequency (TOF) of H_2 production by CdS:MoFe protein biohybrids. Reactions were 16.7 nM CdS, 16.7 nM MoFe protein in 500 mM HEPES, pH 7.0 under 100% N_2 (red), 100% Ar (grey), or 90% N_2 with 10% of acetylene (C_2H_2, blue), or carbon monoxide (CO, green). Reactions were stirred for 2 h under illumination with 3.5 mW cm^{-2} 405 nm light at 25 °C. Mean of N = 4 independent measurements, ± SD.

Table S5.4. Turnover frequencies (TOF) of H_2 production for 30 min illumination of MoFe protein with different nanocrystal materials and diameters.

Nanocrystal material	Nanocrystal diameter (nm)	[a]TOF (s^{-1})	[b]ε (M^{-1} cm^{-1})
CdS nanorods	3.8	6.2 ± 1.7	4.1 x 10^6
CdSe quantum dots	2.5	1.5 ± 0.1	7.6 x 10^4
	2.7	0.22 ± .04	1.4 x 10^5
	3.4	0.19 ± .02	4.6 x 10^5

[a]Reactions were stirred under illumination with 405 nm diode light at ~1.8 mW cm^{-2} at the sample. Levels of H_2 were measured after 30 min by GC. Mean of $N = 4$ independent reactions, ± SD.

[b]Calculated from the nanoparticle absorbance spectra and the established first excited state 1S3/2(h) →1S(e) transition peak wavelength and extinction coefficient.

Table S5.5. Turnover frequencies for H_2 production by CdS:MoFe protein biohybrids with various hole scavengers

[a]**Hole Scavenger**	[b]**nmol H_2 produced CdS:MoFe protein**	[c]**nmol H_2 produced CdS alone**	**Corrected TOF (min^{-1})**
HEPES	14.7	0.7	93.8
MOPS	13.1	1.5	76.9
MES	19.6	6.15	89.9
Ascorbic Acid	14.7	8.3	73.2
Tris	ND	ND	-

[a]Donor concentrations: HEPES, MES, and MOPS, 500 mM; Ascorbic Acid, 100 mM; Tris, 50 mM.

[b]16.7 nM CdS, 16.7 nM MoFe protein. Reactions were stirred for 30 min under illumination with 405 nm diode light at ~1.8 mW cm^{-2}. The levels of H_2 were measured by GC. Average of $N = 2$ independent reactions. ND, not–detected.

[c]16.7 nM CdS. Reactions were stirred for 30 min under illumination with 405 nm diode light at ~1.8 mW cm^{-2}. The levels of H_2 were measured by GC. Average of $N = 2$ independent reactions.

Measurements of NH_3 produced by CdS:MoFe protein biohybrids by the colorimetric ammonia assay.

Table S5.6

[a]Sample	Gas Phase	[b]Absorbance 570 nm	[c]nmol NH_3 in aliquot	[d]nmol NH_3 in reaction
CdS:MoFe protein	100% N_2	0.136 ± 0.005	8.2 ± 0.6	48.7 ± 3.4
	10% C_2H_2 90% N_2	0.069 ± 0.002	0.9 ± 0.3	5.2 ± 1.6
	10% CO 90% N_2	0.069 ± 0.002	0.8 ± 0.3	4.8 ± 1.6
	10% H_2 90% N_2	0.069 ± 0.002	0.8 ± 0.3	4.7 ± 1.7
	100% Ar	0.070 ± 0.002	1.0 ± 0.3	6.0 ± 1.7
CdS:apo–MoFe protein	100% N_2	0.067 ± 0.002	0.6 ± 0.3	3.6 ± 1.6
CdS:hydrogenase (illuminated)	100% N_2	0.068 ± 0.002	0.9 ± 0.3	5.3 ± 2.0
CdS: hydrogenase (dark)	100% N_2	0.068 ± 0.002	0.8 ± 0.4	5.0 ± 2.1
Assay Blank	100% N_2	0.061 ± 0.002	0.01 ± 0.2	0.1 ± 1.4

[a]Results are the means of $N = 4$ independent reactions (± SD). CdS:hydrogenase reaction were performed with [FeFe]–hydrogenase I from *Clostridium acetobutylicum*, previously shown to form biohybrids with CdS and to photocatalyze H_2 evolution and are used here as a negative control for photocatalytic NH_3 production. Reactions with the MoFe protein alone did not produce any detectable N_2 reduction activity.

[b]Mean A_{570} values of $N = 4$ independent reactions (± SD) measured after 2 h of illumination for a 50 µl aliquot of the 300 µl reaction.

[c]Calculated from conversion of A_{570} values to a linear fit of the standard plot for NH_4Cl in Fig. S2A. The linear fit equation, y = a*x + b, where a = 0.0091 ± 0.0002, and b = 0.061 ± 0.001. Value shown is for a 50 µl aliquot of a 300 µl reaction. $N = 4$ independent reactions (± SD).

[d]Total nmol of NH_3 for a 300 µl reaction for each condition (Total nmol in each 300 µl reaction = nmol in 50 µl aliquot x 6). The total nmol NH_3 was used to calculate rate values shown in Fig. 2. Mean of $N = 4$ independent reactions (± SD).

Table S5.7. Average raw fluorescence measurements for photochemical NH_3 production by CdS:MoFe protein biohybrids measured by the o-phthalaldehyde fluorescence assay.

Sample	[a]**Fluorescence @ 472 nm**
CdS:MoFe protein	165.28 ± 57.05
CdS:apo–MoFe protein	77.18 ± 13.31
CdS:MoFe protein (dark)	10.98 ± 29.37

[a]Mean of $N = 4$ independent samples, ± SD.

Table S5.8. Results of NH_3 and H_2 production by CdS:MoFe protein biohybrids in reactions that are lacking a specific component.

[a]Sample	Absorbance 570 nm	[b]Total nmol NH_3 produced	[c]mol NH_3 mol MoFe protein^{-1} min^{-1}	[c]nmol NH_3 mg MoFe protein^{-1} min^{-1}	mol H_2 mol MoFe protein^{-1} min^{-1}	nmol H_2 mg MoFe protein^{-1} min^{-1}
Complete (MoFe protein, CdS, light, HEPES)	0.136 ± 0.005	48.7 ± 2.9	81.2 ± 4.8	340 ± 20	752 ± 75	3146 ± 313
–HEPES	0.068 ± 0.005	4.3 ± 1.3	7.1 ± 2.2	29.8 ± 9	2.5 ± 1.0	10.4 ± 4.2
–CdS	0.070 ± 0.003	5.5 ± 2.3	9.1 ± 3.8	38.2 ± 16.0	1.5 ± 0.5	6.3 ± 2.1
–Light	0.069 ± 0.003	5.2 ± 1.9	8.6 ± 3.2	36.1 ± 13.2	1.7 ± 0.5	6.9 ± 2.1
–MoFe protein	0.062 ± 0.001	0.2 ± 0.9	[d]0.3 ± 1.5	–	[d]319 ± 43	–
–FeMo–co (apo–MoFe protein)	0.067 ± 0.002	3.6 ± 1.6	6.0 ± 2.7	24.9 ± 11.1	46 ± 5	193 ± 22

[a]Reactions were stirred under illumination with 405 nm diode light at 3.5 mW cm^{-2}. The amount of NH_3 and H_2 were measured after 2 h.

[b]Values were calculated using A_{570} values from Fig. S2A for a 50 µl aliquot of a 300 µl reaction. The A_{570} value was fit to the linear equation, y = a*x + b, where a = 0.0091 ± 0.0002, and b = 0.061 ± 0.001 to obtain the value in nmol of NH_3 in 50 µl, and multiplied by 6 to obtain the total NH_3 produced in the 300 µl reaction. Mean of *N* = 4 independent reactions (± SD).

[c]NH_3 levels were measured by the Biovision colorimetric assay and are not corrected for the background from apo–MoFe reactions. Background corrected turnover numbers are listed in Table S10.

[d]Normalized as nmol product nmol^{-1} CdS.

Table S5.9. Comparison of NH_3 and H_2 production rates by nitrogenase (MoFe protein:Fe protein) and CdS:MoFe protein biohybrids under optimized conditions for each of the two reactions.

Sample	mol NH_3 (mol MoFe protein)$^{-1}$ min^{-1}	nmol NH_3 (mg MoFe protein)$^{-1}$ min^{-1}	mol H_2 (mol MoFe protein)$^{-1}$ min^{-1}	nmol H_2 (mg MoFe protein)$^{-1}$ min^{-1}
[a]MoFe protein:Fe Protein + ATP	119	500	460	1932
[b]CdS:MoFe protein biohybrids	75.2 ± 6.2	314 ± 47	729 ± 76	3037 ± 317

[a]Reactions consisted of 0.1 mg MoFe protein, 0.5 mg Fe protein and ATP under 100% N_2 at 30 °C. The NH_3 produced was measured by the fluorescence assay.
[b]Reactions were conducted as described in materials and methods. NH_3 was measured using the colorimetric assay. Mean of $N = 4$ independent reactions, ± SD. Values are corrected for non-catalytic background levels of NH_3 measured in CdS:apo–MoFe protein samples listed in Table S5.8.

Table S5.10. Parameters used to estimate the quantum yield of product formation from N_2 reduction by CdS:MoFe protein biohybrids.

Parameter	Value
Lamp output (405 nm)	34 ± 7 mW
[a]Light power at sample	1.8 ± 0.4 mW
[b]Incident photon rate	$3.6 \pm 0.7 \times 10^{-7}$ mol min^{-1}
[c]Total incident photon	$4.3 \pm 1 \times 10^{-5}$ mol
[d]Photons absorbed	$4.3 \pm 0.9 \times 10^{-6}$ mol

[a]Light power at sample = lamp output x (sample illumination area ÷ output illumination area) = 34 mW x (0.5 cm^2 ÷ 9.5 cm^2) = 1.78 ± 0.40 mW.
[b]Calculated based on photon wavelength = 405 nm with an energy/photon = 4.9×10^{-19} J.
[c]Calculated for 120 min of illumination time.
[d]Photons absorbed was determined based on the CdS:MoFe protein reaction having a transmittance of 89% at 405 nm, to obtain the photons absorbed as 11%. ($4.3 \pm 1 \times 10^{-5}$ incident photons x 11%) = $4.3 \pm 0.9 \times 10^{-6}$ photons absorbed.

Table S5.11. Electron requirement for NH_3 and H_2 product formation at 2 h illumination and estimated quantum yield by CdS:MoFe protein biohybrids from N_2 reduction.

Product	[a]Amount (nmol)	[b]Electrons required for product formation (mol)	Photons absorbed (mol)	[c]Estimated quantum yield of product formation (%)
NH_3	45 ± 7	$0.14 \pm 0.02 \times 10^{-6}$	$4.3 \pm 0.9 \times 10^{-6}$	3.3 ± 0.8
H_2	437 ± 45	$0.87 \pm 0.09 \times 10^{-6}$	$4.3 \pm 0.9 \times 10^{-6}$	20.2 ± 5
$NH_3 + H_2$	482 ± 46	$1.01 \pm 0.09 \times 10^{-6}$	$4.3 \pm 0.9 \times 10^{-6}$	23.5 ± 5

[a]Mean of $N = 4$ independent reactions (± SD) after 2 h of illumination. The product values are corrected for background from CdS:apo–MoFe protein reactions.

[b]nmol electrons required per product:

$½N_2 + 3H^+ + 3e^- \rightarrow$

NH_3 $2H_2 + 2e^- \rightarrow H_2$.

Total nmol e^- based on total products after 120 min = (45 nmol NH_3 x $3e^-$) + (437 nmol H_2 x $2e^-$) = 1009 nmol e^-.

[c]Quantum Yield = (mol e^- used in product formation) ÷ (mol of absorbed photons) x 100%. The observed product ratio for CdS:MoFe protein catalyzed N_2 reduction is ~1 mol NH_3 to 10 mol H_2, which requires [(1 x $3e^-$) + (10 x $2e^-$)] = 23 e^-.

The number of absorbed photons (n) required to provide CdS:MoFe protein biohybrid with 23 e^- is equal to 23 e^- ÷ 1/QY, or 23 ÷ 0.235 = 98. Thus, $n = 98$ absorbed photons.

Table S5.12. Uncorrected NH_3 production time course data for CdS:apo–MoFe protein and CdS:MoFe protein biohybrids under illumination (Fig. 2, time course plot).

Illumination time (min)	**[a]Total nmol NH_3**	**Total nmol NH_3**	**mol NH_3 (mol MoFe protein)$^{-1}$**	**mol NH_3 (mol MoFe protein)$^{-1}$**
	CdS:MoFe protein	**CdS:apo–MoFe protein**	**CdS:MoFe protein**	**CdS:apo–MoFe protein**
20	5.4 ± 1.9	1.9 ± 0.5	1075 ± 388	383 ± 96
40	10.3 ± 1.6	3.5 ± 0.9	2061 ± 314	700 ± 175
60	20.8 ± 2.8	4.2 ± 1.0	4137 ± 562	827 ± 207
90	39.2 ± 4.7	7.4 ± 1.9	7814 ± 943	1479 ± 371
120	48.9 ± 6.7	3.6 ± 2.2	9740 ± 133	719 ± 438
210	58.1 ± 8.1	5.5 ± 1.4	11573 ± 1607	1098 ± 275
300	64.2 ± 8.3	8.8 ± 2.2	12795 ± 1645	1760 ± 438

[a]Mean of $N = 4$ independent measurements, ± SD.

Table S5.13. Background corrected N_2 reduction/NH_3 production time course data for CdS:MoFe protein biohybrids under illumination (Fig. 2, time course plot).

Illumination time (min)	**[a]mol NH_3 (mol MoFe protein)$^{-1}$**
20	692 ± 399
40	1361 ± 360
60	3310 ± 599
90	6335 ± 1013
120	9021 ± 1403
210	10475 ± 1631
300	11036 ± 1702

[a]Values are corrected for non-catalytic background levels of NH_3 measured in CdS:apo– MoFe protein samples listed in Table S5. Error calculated by standard error propagation methods using sample error and CdS:apo–MoFe reaction error

($\sigma_{TOF} = \sqrt{\sigma_{sample}}^2 + \sigma_{Apo-MoFe\ protein}^2$). Mean of $N = 4$ measurements, ± SD.

Table S5.14. Inhibition of Fe protein/ATP dependent H_2 production by MoFe protein in the presence of CdS.

Sample	**nmol H_2 (mg MoFe protein)$^{-1}$ min^{-1}**
[a]MoFe protein + Fe Protein/ATP	1961 ± 192
[b]CdS:MoFe protein biohybrids + Fe Protein/ATP	185 ± 50

[a]Reactions consisted of 0.1 mg MoFe protein, 0.5 mg Fe protein and ATP under 100% N_2 at 30 °C, in the dark, and in a buffer composed of 30 mM phosphocreatine, 5 mM ATP,
0.2 mg/mL creatine phosphokinase, and 1.2 mg/mL BSA) in 100 mM HEPES buffer at pH 7.0. The nmol of H_2 was measured by GC. Mean of $N = 4$ independent reactions, ± SD.
[b]CdS:MoFe protein biohybrids; 16.7 nM CdS, 16.7 nM MoFe protein.

Table S5.15. Data used to determine the effects of gaseous inhibitors on TOF of NH_3 production plotted in Fig. 2, uncorrected for non-catalytic background levels of NH_3 measured in CdS:apo–MoFe protein samples.

Sample	**Gas phase of reaction**	**[a]nmol NH_3 detected**	**[a]Total nmol NH_3 produced**	**[a]TOF (min^{-1})**
CdS:MoFe protein	100% N_2	8.2 ± 0.6	48.9 ± 3.4	81.2 ± 5.6
	10% C_2H_2, 90% N_2	0.9 ± 0.3	5.2 ± 1.6	8.7 ± 2.7
	10% CO, 90% N_2	0.8 ± 0.3	4.8 ± 1.6	8.0 ± 2.7
	10% H_2, 90% N_2	0.8 ± 0.3	4.7 ± 1.7	7.8 ± 2.8
	100% Ar	1.0 ± 0.3	6.0 ± 1.7	9.9 ± 2.8
CdS:apo–MoFe protein	100% N_2	0.6 ± 0.3	3.6 ± 1.6	6.0 ± 2.6

[a]Mean of $N = 4$ independent measurements, ± SD.

Table S5.16. TOF of NH_3 production by CdS:MoFe protein plotted in Fig. 2, and corrected for non- catalytic background levels of NH_3 measured in CdS:apo–MoFe protein samples.

Gas phase of reaction	[a]Absorbance 570 nm	[b]nmol NH_3 detected	[c]nmol NH_3 produced	[d]Corrected TOF (min^{-1})
100% N_2	0.136 ± 0.005	8.2 ± 0.6	48.9 ± 3.4	75.2 ± 6.2
10% C_2H_2, 90% N_2	0.069 ± 0.002	0.9 ± 0.3	5.2 ± 1.6	2.7 ± 3.7
10% CO, 90% N_2	0.069 ± 0.002	0.8 ± 0.3	4.8 ± 1.6	2.1 ± 3.8
10% H_2, 90% N_2	0.069 ± 0.002	0.8 ± 0.3	4.7 ± 1.7	1.9 ± 3.8
100% Ar	0.070 ± 0.002	1.0 ± 0.3	6.0 ± 1.7	3.9 ± 3.8

[a]Mean of *N*=4 independent reactions after 2 h of illumination.
[b]Calculated using A_{570} values for a 50 µl aliquot of a 300 µl reaction fit to the plot in Fig. S2A. The A_{570} value was fit to the linear equation, y = a*x + b, where a = 0.0091 ± 0.0002, and b = 0.061 ± 0.001 to obtain the value in nmol of NH_3 in 50 µl.
[c]Calculated by multiplying amount of the NH_3 detected in a 50 ul aliquot by 6 to obtain the total NH_3 produced in the 300 µl reaction.
[d]Calculated by subtracting CdS:apo–MoFe protein sample background (3.6 ± 1.6 nmol) from the total nmol produced; Mean of *N*=4 independent reactions (± SD). SD was calculated by standard error propagation method using sample error and CdS:apo–MoFe protein sample error ($\sigma_{TOF} = \sqrt{\sigma_{sample}{}^2 + \sigma_{Apo-MoFe\ \ protein}{}^2}$).